Scalar Vortex Coronagraphs for Imaging Habitable Exoplanets

Thesis by
Niyati Desai

In Partial Fulfillment of the Requirements for the
Degree of
Doctor of Philosophy in Space Engineering

CALIFORNIA INSTITUTE OF TECHNOLOGY
Pasadena, California

2024
Defended May 21, 2024

Niyati Desai
ORCID: 0000-0002-2843-8325

ACKNOWLEDGEMENTS

In this journey, there are many who've played pivotal roles, shaping my path and enriching my experience.

Foremost, I'd like to acknowledge my advisor Dimitri. Your unwavering confidence in my abilities from the first day has shaped who I am as a scientist. Thank you for all the exciting discussions and opportunities. You always gave me guidance when I needed it and encouraged me to explore my own ideas with independence.

To my thesis committee, Richard, Dan and Vanessa — each one of you provided support and encouragement for my academic dreams and throughout my PhD.

To my collaborators, especially Gary, AJ, Gene, Nem, Jorge, Arielle, Axel and Susan — thank you for your mentorship and wisdom, both in the lab and beyond. You always showed enthusiasm for my ideas, and without you, this thesis would not be the same.

To my dear labmates, especially Dan — I couldn't have asked for a better officemate to bounce the crazy ideas in my head and laugh about the ups and downs of grad school with. Also Katelyn, JB, Ashley, Yinzi, Jerry — your camaraderie and enthusiasm made every day in the office brighter and every conference an adventure.

To my cohort — Sahangi, Sorina, Tanner, John, Miles, Peter, Brayden — our shared moments of fun and friendship have been perfect breaks from the rigors of academia.

To all my friends along the way, thanks for sharing in my excitement for this work and coming to all my public talks even though it's not your field: Sandra, Ananya, Nancy, Dayna, Maddie, Nik, Andy & Victor, Emily, Harsha and many more.

To my family who has watched me grow throughout this process and continue to be proud of me and my aspirations. Thank you for always believing in me.

Finally to Lorenzo, whose presence has been a constant reminder of life's richness and the importance of balance — thank you for being by my side and inspiring me to strive for more. Of all the things I found in grad school, you are by far the best.

ABSTRACT

Of the over 5,600 exoplanets detected to date, less than 2% have ever been directly imaged. Direct imaging is crucial for the study of habitable exoplanets around Sun-like stars because it offers the potential to characterize their atmospheres and detect biosignatures. However, the extreme contrast between star and planet light poses immense challenges which coronagraphs aim to address. Future telescopes, like NASA's upcoming Habitable Worlds Observatory, necessitate coronagraphs capable of suppressing starlight to contrast levels of 10^{-10} and operating in broadband light to directly image and characterize habitable planets. To meet these ambitious goals, innovations in focal plane mask technologies and wavefront sensing and control strategies are imperative.

This thesis investigates the viability of scalar vortex coronagraphs for direct imaging of habitable exoplanets. The first part of this thesis focuses on simulation efforts for modeling various coronagraph mask topographies and laboratory testing. Analysis of current scalar vortex topographies found phase wrapping is favorable over classic vortex designs. The chromatic performance of one such design — the wrapped staircase scalar vortex coronagraph — is investigated and a laboratory demonstration is presented.

Next, this thesis explores the behavior of different wavefront sensing and control methods combined with the wrapped staircase scalar vortex coronagraph. Three techniques were implemented on a high contrast imaging testbed and competitive performance between model-free and model-based techniques was found, particularly with increasingly complex mask designs.

Lastly, new scalar vortex mask designs which combine radially and azimuthally varying features are investigated. Specifically, the benefits of adding central phase dimples to scalar masks to improve broadband performance are explored. Hybrid designs incorporating phase dimples are found to suppress chromatic leakage and show substantial improvement in broadband contrast over current scalar vortex designs.

Overall, this thesis advances the understanding and development of scalar vortex coronagraphs for exoplanet direct imaging, explores their potential for future space telescopes and highlights avenues for further research and experimentation.

PUBLISHED CONTENT AND CONTRIBUTIONS

Desai, N., A. Potier, S. Redmond, G. Ruane, A. E. Riggs, P. K. Poon, et al. (2024, Accepted). "A comparative laboratory study of electric field conjugation algorithms". In: *Journal of Astronomical Telescopes, Instruments, and Systems*.
N.D. conducted the laboratory experiments at JPL, collected and analyzed the data and prepared the manuscript.

Desai, N., D. Mawet, E. Serabyn, G. Ruane, A. Bertrou-Cantou, J. Llop-Sayson, and A. J. E. Riggs (2024). "Benefits of adding radial phase dimples on scalar coronagraph phase masks". In: *Journal of Astronomical Telescopes, Instruments, and Systems* 10.1, p. 015001. DOI: 10.1117/1.JATIS.10.1.015001.
N.D. developed the simulations of the new designs, performed the data analysis and prepared the manuscript.

Desai, N., A. Bertrou-Cantou, G. Ruane, J. Llop-Sayson, A. E. Riggs, E. Serabyn, and D. Mawet (2023a). "Achromatizing scalar vortex coronagraphs with radial phase mask dimples". In: *Techniques and Instrumentation for Detection of Exoplanets XI*. Vol. 12680. SPIE. DOI: 10.1117/12.2677224.
N.D. developed the simulations of the new designs, performed the data analysis and prepared the manuscript.

Desai, N., L. König, E. Por, R. Juanola-Parramond, R. Belikov, et al. (2023b). "Integrated photonic-based coronagraphic systems for future space telescopes". In: *Techniques and Instrumentation for Detection of Exoplanets XI*. Vol. 12680. SPIE. DOI: 10.1117/12.2677210.
This paper is a result of a workshop. N.D. conceptualized the idea with a large team and led the manuscript preparation.

Desai, N., A. Potier, G. Ruane, A. E. Riggs, P. K. Poon, M. Noyes, and C. Mejia Prada (2023c). "Experimental comparison of model-free and model-based dark hole algorithms for future space telescopes". In: *Techniques and Instrumentation for Detection of Exoplanets XI*. Vol. 12680. SPIE. DOI: 10.1117/12.2677040.
N.D. conducted the laboratory experiments at JPL, collected and analyzed the data and prepared the manuscript.

Desai, N., G. J. Ruane, J. D. Llop-Sayson, A. Bertrou-Cantou, A. Potier, A. E. Riggs, et al. (2023d). "Laboratory demonstration of the wrapped staircase scalar vortex coronagraph". In: *Journal of Astronomical Telescopes, Instruments, and Systems* 9.2, p. 025001. DOI: 10.1117/1.JATIS.9.2.025001.
N.D. performed the simulations, prototype characterization and laboratory experiments. N.D. collected and analyzed the data and prepared the manuscript.

Desai, N., J. Llop-Sayson, A. Bertrou-Cantou, G. Ruane, A. E. Riggs, E. Serabyn, and D. Mawet (2022). "Topological designs for scalar vortex coronagraphs". In: *Space Telescopes and Instrumentation 2022: Optical, Infrared, and Millimeter Wave*. Vol. 12180. SPIE, 121805H. DOI: 10.1117/12.2630950.
N.D. performed the simulations and analysis, and prepared the manuscript.

Desai, N., J. Llop-Sayson, N. Jovanovic, G. Ruane, E. Serabyn, S. Martin, and D. Mawet (2021). "High contrast demonstrations of novel scalar vortex coronagraph designs at the high contrast spectroscopy testbed". In: *Techniques and Instrumentation for Detection of Exoplanets X*. SPIE. DOI: 10.1117/12.2603953.
N.D. performed the simulations, prototype characterization and laboratory experiments. N.D. collected and analyzed the data and prepared the manuscript.

TABLE OF CONTENTS

LIST OF FIGURES

LIST OF TABLES

Chapter 1

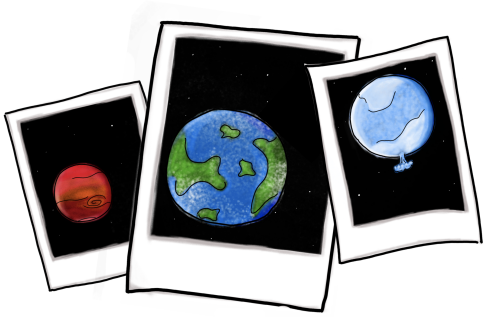

THE AGE OF EXOPLANETS

1.1 Are we alone?

The age old question of whether life exists out there in the universe is the driving curiosity behind much of today's astronomical ambitions. With all the science fiction shows and literature that have become popularized throughout the last century, it is hard to believe that the first concrete proof of planets outside our solar system was only found thirty years ago!

On January 9th, 1992, two radio astronomers at Arecibo Observatory announced their discovery of the first extra-Solar planet (exoplanet). They used precise timing measurements of the pulsar PSR 1257+12's radio emissions to confirm the detection of two orbiting planets (Wolszczan and Frail, 1992). Just three years later two future Nobel-prize winning astronomers from the University of Geneva announced the first definitive detection of an exoplanet orbiting a main-sequence star. By measuring the gravitational influence of a planet on its host star, they found a giant planet in a four-day orbit around the nearby star 51 Pegasi (Mayor and Queloz, 1995). This detection shattered existing theories about planetary formation and orbits, as it was previously thought that gas giants could not exist so close to their stars.

It was not long before technological advances led to the rapid discoveries of many new exoplanets. Soon after, astronomers realized variations in a star's apparent luminosity revealed orbiting planets transiting in front of them (Charbonneau et al., 2000; Henry et al., 1999). These discoveries ushered in the 'age of exoplanets.' The

turn of the twenty-first century was the start of an 'exoplanet gold rush.' The more exoplanets astronomers found, the more they realized the striking diversity of these worlds, which differed significantly from those within our own solar system.

Observations from ground telescopes played a critical role in starting this exoplanet hunt, but eventually space telescopes would become the key to building an exoplanet database. In 2009 the Kepler space telescope, the first mission dedicated to planet-finding, was launched. It would result in the confirmed detection of several thousand exoplanets. Kepler was followed in 2018 by the Transiting Exoplanet Survey Satellite (TESS) whose goal was to conduct an all-sky survey solely in search of new exoplanets. These successful missions paved the way for flagship space telescopes including the James Webb, Gaia and Nancy Grace Roman space telescopes all with science objectives dedicated to exoplanet discovery and characterization.

Today, only thirty years since their original discovery, over 5,600 exoplanets have been detected through various techniques (NASA Exoplanet Science Institute, 2020), and many more are expected to be found in the next decade. The quest to answer the question 'Are we alone?' has been a curiosity since the beginning of mankind. Now, with the scientific community eager to explore strange new worlds outside our Solar system and rapidly advancing scientific technologies, this generation might be the first to successfully find and characterize habitable exoplanets in search of new life.

1.2 Detection techniques

Although there has been speculation for many centuries of other worlds existing around some of the many stars we see in the night sky, their detection was not possible for a long time. This is because the faint signal from a planetary companion needs to be separated from the much brighter light of the host star. Several exoplanet detection techniques have been developed over the past three decades but most are 'indirect' methods. These methods rely on observing the star and inferring the existence of a planet nearby without directly measuring light from it. Different methods allow for measurements of different exoplanet characteristics such as planet size, mass, orbital parameters, and in some cases atmospheric or surface compositions. However, only direct detection of exoplanets enables their spectroscopy with the required resolution to constrain an individual planet's atmospheric properties — e.g., temperature, gravity, chemical composition, and clouds. The four main indirect detection methods shown in Figure 1.1 along with the direct imaging method are

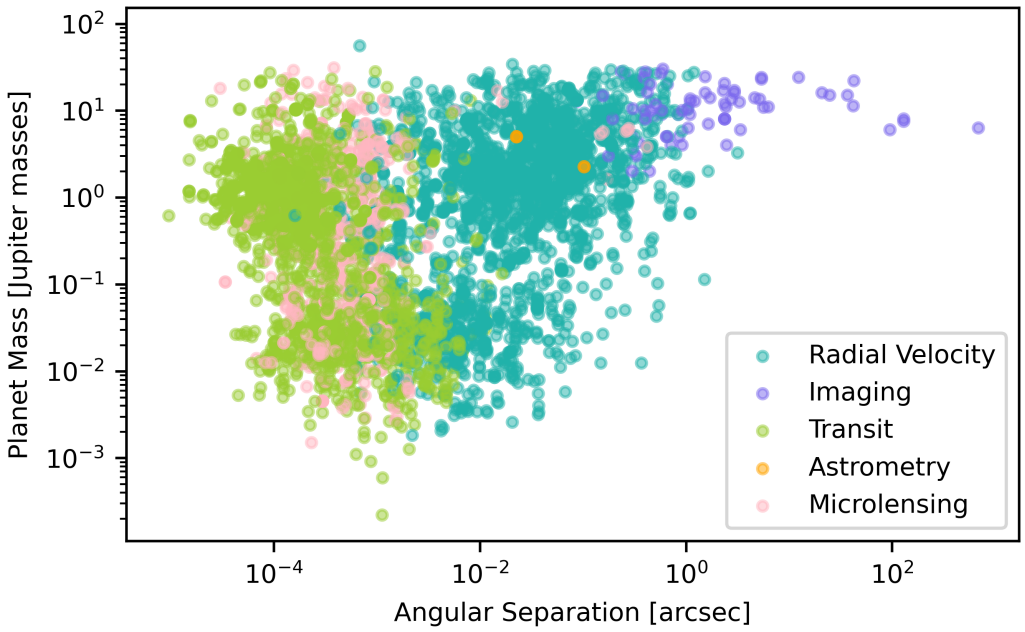

Figure 1.1: The mass and angular separation of all confirmed exoplanets detected through radial velocity, transit, microlensing, astrometry and direct imaging techniques as of April 20, 2024 (NASA Exoplanet Archive). [1]

discussed here. Other detection techniques account (eclipse, pulsar and transit timing variations, etc.) for less than 2% of the exoplanets discovered to date and are therefore not discussed in detail.

Radial velocity

When a star has one or more planets in orbit around it, the star and planets orbit around their combined center of mass. The planet's gravitational pull on its host star can be measured through the Doppler shift effect on the stellar spectrum. The influence of a planet as it pulls the star slightly towards or away from the observer results in a radial velocity component of the star. It is seen as small blueshifts or redshifts in its spectrum, provided the orbit is not perpendicular to the line of sight to the observer. The radial velocity variations will be larger for companions of higher mass and shorter orbital periods, making this method biased toward detecting exoplanets with these characteristics. Radial velocity measurement detections provide insight into a planet's orbital parameters, like the period and eccentricity and also provide a lower limit on the planet mass. Since being used for the famous first planet around a

[1] `https://exoplanetarchive.ipac.caltech.edu/index.html`

main-sequence star detection (Mayor and Queloz, 1995), the radial velocity method has successfully detected over one thousand (confirmed) exoplanets.

Transit photometry

When the orbit of a planet is aligned with the observer such that the system is seen edge-on, the planet passes in front of the star causing periodic dimming in the star's brightness which can be observed. During this transit, the measured light from the star decreases proportionally to the ratio of the area of the planet to the area of the star. A transit of a Jupiter-like planet around a Sun-like star would cause the flux to drop by only about 1%, and for an Earth-like planet this drop would be only 0.01%. The likelihood of observing a transit depends on the lucky alignment of the planet and star along our line of sight. Closer-in planets have a higher chance of transiting and larger planets produce larger transit depths, making those the easiest to detect with this method. Spectroscopy during a transit can sometimes be used to learn about the planet's partially transmitted atmosphere. However detecting a planet with a similar mass as the Earth in the habitable zone of Sun-like stars is challenging with transit photometry. If viewed as an exoplanet, the Earth would only appear to transit once a year because of its long orbital period (1 year) and small transit depth (0.01%). It would require observations over many years or even decades to acquire the necessary signal to noise ratio of transit spectra to reveal biosignatures. Despite this, transits account for the majority of exoplanet detections to date (as seen in Figure 1.1) thanks to successful surveys from missions like Kepler. Kepler surveyed more than 500,000 stars in a localized part of the sky resulting in more than 2,700 confirmed exoplanets detected with the transit method.

Astrometry

A planet's gravitational influence on its host star can also be detected by measuring the star's periodic change in apparent position in the sky. Astrometry makes precise measurements of a star's position in the sky and compares its proper motion relative to the more distant, relatively fixed background stars. Perturbations to the proper motion induced by the planet's pull can then then be used to determine the orbital parameters of the planet. This method is biased towards massive exoplanets on wide orbits in nearby systems since the astrometric precision required is extremely high. So far this method has only yielded a handful of confirmed detections. The Gaia space telescope aims to measure the position of over 1.8 billion stars over the course of 10 years with a precision down to a few microarcseconds or less (Lazorenko

and Sahlmann, 2017; Gaia Collaboration et al., 2016). Gaia is expected to detect thousands of new exoplanets in the coming years through the astrometry technique.

Microlensing

When a distant star aligns with a foreground star, the distant star's light is distorted due to the gravitational field of the foreground star. The foreground star then acts as a gravitational lens amplifying the light of the background star. This effect is called 'lensing' because there is an observable magnification which depends on the mass and trajectory of the foreground star. Monitoring the background star's brightness on the timescale of months enables the detection of such gravitational microlensing events. These events result in a characteristic lightcurve from which certain parameters of the lensing star can be inferred. If the lensing star happens to have a companion, the additional gravitational distortion results in a characteristic spike of the lightcurve. This method has been successful in making many new exoplanet detections as can be seen in Figure 1.1. However it requires detailed sampling of the lightcurve over a long time, since the planet signature in the lightcurve is typically much shorter than the overall duration of the microlensing event, which itself can take months or years. In addition, microlensing detections typically cannot be confirmed by other techniques since those systems are too far from the Earth. The Nancy Grace Roman Space Telescope is expected to use this technique throughout its wide-field survey of the sky to contribute thousands of new exoplanets detected through microlensing events.

Direct imaging

Directly imaging exoplanets requires isolating the signal of a faint planet from the light of the bright host star. Although the transit and radial velocity methods make up the majority of current exoplanet detections, these methods have limitations regarding the study of key molecules in exoplanet atmospheres or surface temperatures over a wide range of planet types and separations (Konopacky et al., 2013; National Academies of Sciences, Engineering and Medicine, 2021). Direct imaging involves capturing light directly from the planet, which enables direct spectroscopy and is therefore the most promising method for the characterization of Earth-like exoplanets and the detection of biosignatures. However only less than $\sim 2\%$ of the $\sim 5,600$ exoplanets discovered to date have been directly imaged.

The starlight suppression level required to detect a planet by direct imaging depends on whether the detection is in reflected light or thermal emission and varies with the

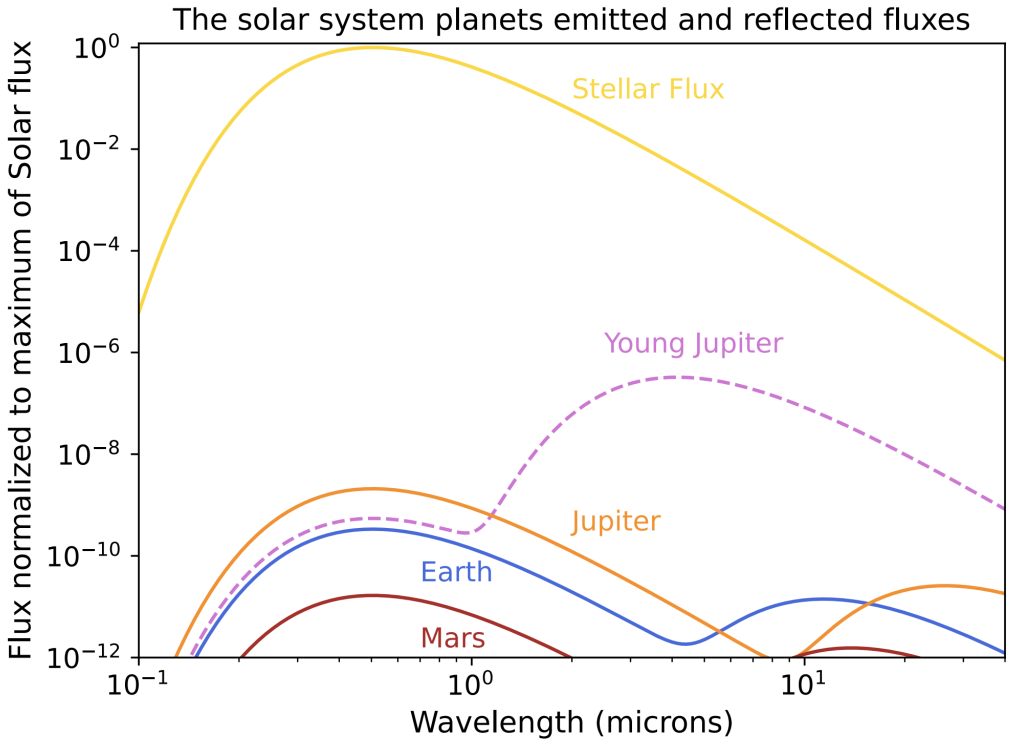

Figure 1.2: Reflected (in the visible) and emitted (in the near-IR) fluxes for Solar System planets, normalized to the maximum of the Sun flux (from Galicher and Mazoyer, 2023).

planet (e.g., size, temperature, albedo, etc.) and the projected angular separation to its host star. This can be seen in Figure 1.2 which shows the luminosity ratio between an exoplanet and its host star. The reflected flux (in the visible) and emitted flux (in the near-IR) for Solar System planets is shown normalized to the maximum of the Sun flux. This ratio corresponds to the required contrast to achieve with stellar suppression techniques in order to directly detect exoplanets of these characteristics. So far, all the exoplanets which have been directly imaged are young and still hot from formation. Their thermal emission results in contrasts around 10^{-6} with their host star, which is easier to directly detect. In reflected visible light, an Earth-like planet would be on the order of 10^{10} times fainter than its Sun-like host star.

Direct imaging is challenging not only because of the large brightness difference between the star and the planet, but also because of the small angular separation between them. An Earth twin orbiting a Sun-like star at a projected separation of 1 AU subtends an angle of 0.1" from a distance of 10 parsecs. As can be seen in the

distribution in Figure 1.1, no planets at this angular separation or closer have yet been directly imaged. Furthermore, for the purpose of atmospheric spectroscopy, imaging the planet over a large spectral bandwidth is necessary. The combination of high contrast and small angular separation makes it more challenging for direct imaging than for other indirect methods to detect planets at small angular separations from their host star (seen in the left half of Figure 1.1).

1.3 Achievements with direct imaging

Several stellar suppression techniques have been successfully developed over the past few decades, for the purpose of directly imaging exoplanets. These techniques can be divided in three main categories. Interferometric nullers destructively interfere the starlight collected by multiple telescopes or multiple telescope subapertures (Serabyn et al., 2022). External starshades propose to block the starlight before it reaches the telescope with two coordinated spacecrafts (Cash, 2006). Stellar coronagraphs remove the starlight after it enters a telescope through a series of focal and pupil plane masks and active wavefront correction (Galicher and Mazoyer, 2023). This thesis focuses only on direct imaging using coronagraphs, specifically on advancing coronagraph technology to meet exoplanet goals of the upcoming generation of space telescopes.

The first direct images and spectra of planet candidates relied on simple coronagraphs coupled with facility, general-use adaptive optics (AO) systems to deblur starlight. The past decade has seen the development and improvement of dedicated extreme AO systems coupled with advanced coronagraphs. These upgrades in combination with sophisticated post-processing methods have allowed for the detection of planets that are fainter and less massive or located at smaller angular separations. Spectroscopy instruments used in combination with extreme AO systems like the Spectro-Polarimetric High-contrast Exoplanet REsearch instrument (SPHERE) on the Very Large Telescope (VLT) and the Gemini Planet Imager (GPI) have provided critical low-resolution spectra of most directly-imaged exoplanets. These instruments have been critical in conducting direct imaging surveys in the last decade to provide constraints on the likely formation mechanism of directly imaged planets (Currie et al., 2023). Our original understanding of planet formation was based on our own solar system where planets are neatly arranged so that small planets are nearby to the Sun and larger planets are further out.

However early exoplanet detections determined a large population of giant planets at very small separations from their host star. The existence of these "hot Jupiters" was unexpected and therefore raised immediate questions about their formation and migration. The more planets that were detected, the more atypical our Solar system seemed. Years later, the first direct imaging detections found giant planets at unexpectedly wide separations — raising even more questions.

There are two main theories on how giant planets can form: core accretion and gravitational instability. In the core accretion model, a rocky core accretes first from planetesimals, followed by a gas envelope and pebble accretion leading to giant planets. Core accretion predicts more giant planets closer to the star and more lower-mass planets than higher-mass ones (Ida et al., 2013). In the gravitational instability model, if a disk is massive enough to experience self-gravity, parts of the disk can undergo fragmentation and quickly form giant planets. Gravitational instability predicts giant planets generally at wider separations, with more higher-mass planets than lower-mass ones, and no strong dependence on stellar mass (Forgan et al., 2014).

Exoplanet demographics from surveys have recently been used to determine which of these formation and migration mechanisms might be dominant, since each theory predicts planets will be found in very different parts of their stellar systems. Direct imaging surveys with the VLT/SPHERE found non-detections in the mass-separation parameter space where gravitational instability formation would be possible (Chauvin et al., 2015). Meanwhile the Gemini Planet Imager Exoplanet Survey (GPIES) (Nielsen et al., 2019) and SPHERE Infrared Survey for Exoplanets (SHINE) (Vigan et al., 2021) surveyed hundreds of stars and only found a few giant planets. The ones they did detect were still at relatively close separations with relatively lower-mass, and they were also more commonly found around higher mass stars – all factors pointing to core accretion.

When combined with results from radial velocity surveys at smaller separations (Fulton et al., 2021), a pronounced peak in the giant planet occurrence rate between 1 and 10 AU is confirmed. The increased occurrence from 1-10 AU corresponds to an angular separation of less than 0.1". This explains the relatively low numbers of directly detected planets with current imaging capabilities.

Overall, the abundance of indirectly detected planets at separations closer than is currently directly imageable, motivates improving coronagraph performance at small separations. Since transit photometry is limited to planets with very close

separations (typically <1AU), direct imaging will be critical to close the gap and retrieve spectral data for Earth-analogues. Coronagraphic capabilities at shorter wavelengths (<1 μm) will also need to be improved for this goal since direct imaging has so far only been able to detect brighter young planets. For example, the dashed young Jupiter flux in Figure 1.2 is based on physical values of the 51 Eridani system. This curve demonstrates how the current 10^{-6} contrast capability in near-infrared wavelengths is sufficient to directly detect thermally emitting planets like 51 Eridani b. The required contrast for imaging is more favorable in the infrared, where exoplanet emission peaks. However an Earth-like planet around a Sun-like star will require detection in the visible at the 10^{-10} contrast level.

1.4 The future of direct imaging

The recent Astro2020 Decadal Survey has identified the search for habitable exoplanets as a top priority science direction (National Academies of Sciences, Engineering and Medicine, 2021). The ability to image faint exoplanets near bright stars is key to creating a census of extrasolar planets and measuring their properties, and this calls for technological advancement of high-contrast coronagraphic techniques.

In the next few years, new technology applied to exoplanet imaging instruments from the ground will close the gap between the directly imageable planets and those that have only been detected indirectly. To reach planets at closer separations, larger apertures are needed. In the farther future, ground-based direct imaging will be revolutionized with the bigger-than-ever apertures of the Extremely Large Telescope (ELT) (Gilmozzi and Spyromilio, 2007), the Thirty Meter Telescope (TMT) (Packham et al., 2018), and the Giant Magellan Telescope (GMT) (Fanson et al., 2022).

At the same time new data from the James Webb Space Telescope (JWST) will provide detections of planets undetectable from the ground. Within the decade, the Coronagraphic Instrument (CGI) on the Roman Space Telescope will demonstrate focal-plane wavefront control with deformable mirrors in space (Spergel et al., 2013). Building off this technology and employing more advanced coronagraphs, NASA's next flagship telescope, the Habitable Worlds Observatory (HWO), will be dedicated to directly imaging exo-Earths. Although it will likely also detect thousands of new diverse planets, it promises to make the confirmed discovery and characterization of 25 Earth-like planets.

However this will require suppressing starlight at a level that is well beyond the capabilities of current ground and space-based high-contrast imaging instruments. As seen in Figure 1.2, directly imaging a Jupiter or Earth at 10 parsecs would require blocking starlight at angular separations of 0.5" or 0.1". In visible light this corresponds to achieving contrasts of 10^{-9} and 10^{-10}, respectively. Current coronagraph technologies need to be improved to reach this performance level. However the selection of a coronagraph does not only depend on its ability to suppress starlight, but also on factors such as high off-axis throughput (e.g., from a planet), a small inner working angle, and insensitivity to chromatic errors, tip/tilt and other low-order wavefront aberrations. This thesis aims to develop new coronagraph designs considering this context and demonstrate their potential for exo-Earth imaging with the future HWO space telescope.

Chapter 2

CORONAGRAPHY THEORY

2.1 Light propagation principles

To understand how the earliest coronagraphs were theorized and how new coronagraph designs are currently modelled, the foundational principles of light propagation need to be reviewed (Goodman, 2005). When a beam of light is partly blocked by an obstacle, some of the light is scattered around the object. This causes multiple interference patterns and light and dark bands are often seen at the edge of the shadow — this effect is known as diffraction.

In classical physics, the diffraction phenomenon is described by the Huygens–Fresnel principle which treats each point in a propagating wavefront as a collection of individual spherical wavelets. This 'Fresnel diffraction' only occurs when either the distance from the source to the obstruction or the distance from the obstruction to the screen is comparable to the size of the obstruction.

When the diffraction pattern is viewed at a sufficiently long distance from the object (in the far-field region), or when it is viewed at the focal plane of an imaging lens, approximations can be made so 'Fraunhofer diffraction' principles are valid to describe the light's behavior. In the case of observing a star through a telescope, the light source is so far away that its origin can be approximated to be at infinity. The light rays coming from the source would then be parallel and the wavefronts would be planar as opposed to spherical.

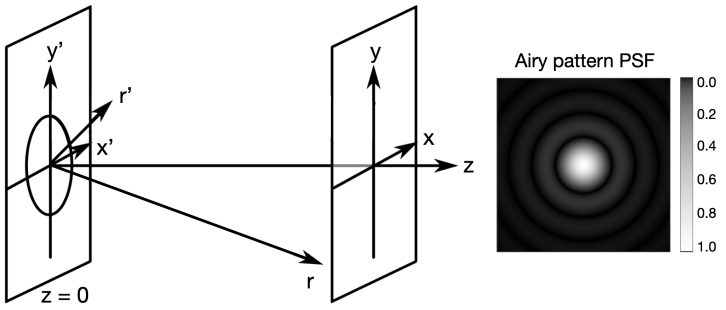

Figure 2.1: Example circular aperture and image plane demonstrating Fraunhofer diffraction. The resulting image plane on the right shows that the point spread function (PSF) is an Airy pattern.

Fraunhofer Diffraction

Figure 2.1 shows an example aperture in $x'y'$ plane, illuminated by a wave of wavelength λ, wavenumber k and complex amplitude $A(x', y')$. The diffracted wave is observed in the unprimed x, y-plane along the positive z axis.

The complex amplitude $U(x, y)$ of the diffracted wave is given by the Fraunhofer diffraction equation as:

$$U(x, y, z) \approx \frac{e^{ikz} e^{ik\left(x^2+y^2\right)/2z}}{i\lambda z} \iint_{\text{Aperture}} A\left(x', y'\right) e^{-i\frac{k}{z}(x'x+y'y)} dx'dy' \tag{2.1}$$

where $k = 2\pi/\lambda$ (Goodman, 2005). This integral can be recognized as simply the Fourier transform of the aperture function evaluated at frequencies $f_x = x/(\lambda z)$ and $f_y = y/(\lambda z)$.

Equation 2.1 written in terms of the Fourier transform:

$$U(x, y, z) \propto \mathcal{F}\left[A(x', y')\right]_{f_x f_y} .$$

This concept of using Fourier transforms to describe classical optics is briefly revisited throughout this thesis as it is used to describe Fraunhofer diffraction through an aperture as well as the Fourier transforming properties of lenses.

Circular Apertures

When the diffracting aperture has circular symmetry, it is convenient to use polar rather than Cartesian coordinates. The integral representation of the Bessel function can then be used to rewrite the Fourier transform in Equation 2.1 where r' is the radial coordinate in the aperture plane ($r' = \sqrt{x'^2 + y'^2}$) and r is the radial coordinate in the image plane:

$$U(r, z) \propto 2\pi \int_0^\infty A\,(r')\, J_0\left(\frac{2\pi r' r}{\lambda z}\right) r' dr'. \tag{2.2}$$

In this case, $U(r, z)$ is equal to the Fourier–Bessel or Hankel transform, $\mathcal{B}\{\cdot\}$, of the aperture function, $U(r')$.

For a circular aperture with radius l like the one shown in Figure 2.1, the aperture can be written as:

$$U(x', y') = \text{circ}\,(r'/l)$$

where

$$\text{circ}(r'/l) = \begin{cases} 1, & \text{for } r' < l \\ 1/2, & \text{for } r' = l \\ 0, & \text{for } r' > l \end{cases}.$$

Then the electric field can be written as

$$U(r) = \frac{e^{ikz}}{i\lambda z} \exp\left(i\frac{kr^2}{2z}\right) \mathcal{B}\left[U(r')\right]\Big|_{\rho = r/\lambda z} \tag{2.3}$$

where $\rho = \sqrt{f_X^2 + f_Y^2}$ represents the radius in the spatial frequency domain.

For a uniform normally incident plane wave with unit amplitude, the transmitted field would be equal to the amplitude transmittance. Since

$$\mathcal{B}\left\{\text{circ}\left(\frac{r'}{l}\right)\right\} = A\frac{J_1(2\pi l\rho)}{\pi l\rho} \tag{2.4}$$

where $A = \pi l^2$, or the area of the aperture, the resulting amplitude distribution in the Fraunhofer diffraction pattern takes the form:

$$U(r) = \exp\,(ikz) \exp\left(i\frac{kr^2}{2z}\right) \frac{A}{i\lambda z}\left[2\frac{J_1(kwr/z)}{kwr/z}\right]. \tag{2.5}$$

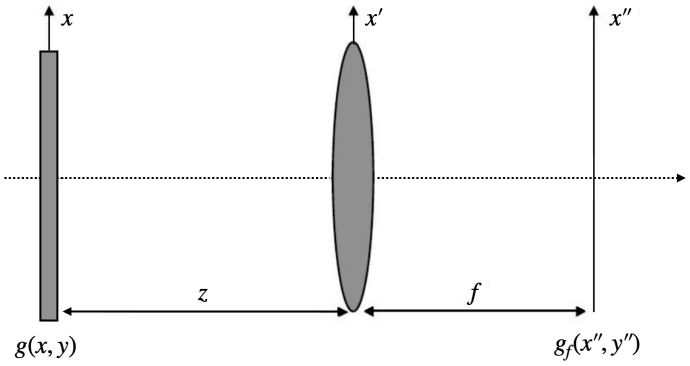

Figure 2.2: An optical system with an input plane, convex lens of focal length f, and image plane.

and the intensity distribution is written as

$$I(r) = \left(\frac{A}{\lambda z}\right)^2 \left[2\frac{J_1(kwr/z)}{kwr/z}\right]^2 . \tag{2.6}$$

This is referred to as the point spread function (PSF). This particular PSF for a perfectly circular aperture can be seen on the right in Figure 2.1. It is the well-known Airy pattern which will be found throughout this work in both experimental and simulated results since this thesis considers only circular telescope pupils.

Imaging lenses and mirrors

After the telescope's aperture, Fourier optics can also be utilized to describe the light propagation through lenses and mirrors in the telescope. According to the diffraction theory, a convex lens (or equivalently a concave mirror) of focal length f will produce the Fourier transform at a distance f after the lens of an object placed at a distance z before the lens.

Consider the optical setup in Figure 2.2. Here the input field is $g(x, y)$ and the back focal plane diffraction pattern is $g_f(x'', y'')$.

In one dimension,

$$g_{\mathrm{f}}(x'') = \exp\left\{i\pi\frac{x''^2}{\lambda f}\left(1 - \frac{z}{f}\right)\right\} \int g(x) \exp\left\{-i2\pi\frac{xx''}{\lambda f}\right\} \mathrm{d}x. \tag{2.7}$$

In two dimensions,

$$g_{\mathrm{f}}\left(x'', y''\right) = \exp\left\{i\pi \frac{x''^2 + y''^2}{\lambda f}\left(1 - \frac{z}{f}\right)\right\} \iint g(x, y) \exp\left\{-i2\pi \frac{xx'' + yy''}{\lambda f}\right\} \mathrm{d}x\, \mathrm{d}y \tag{2.8}$$

where it can be clearly seen again that the Fourier transform $G = \mathcal{F}[g(x, y)]$ emerges:

$$g_{\mathrm{f}}\left(x'', y''\right) = \exp\left\{i\pi \frac{x''^2 + y''^2}{\lambda f}\left(1 - \frac{z}{f}\right)\right\} G\left(\frac{x''}{\lambda f}, \frac{y''}{\lambda f}\right). \tag{2.9}$$

Fourier optics is the study of classical optics using Fourier transforms. One of the main strengths of using Fourier transforms is that it is well studied from signal processing and therefore developed methods like the Fast Fourier Transform (FFT) can be efficiently used to model light propagation through complex optical systems. These are useful tools to apply to telescope instruments in general because they can be used to describe arbitrary phase and amplitude patterns as they propagate through both focal and pupil planes. This property is particularly interesting for coronagraphic applications where a series of focal and pupil planes masks are combined in order to suppress starlight.

As the light passes through pupil and focal planes, its amplitude and phase is modified. The light can be traced and each propagation represented as an operator. For example, consider an optical system with one lens between two planes, A and B, where A is a pupil plane and B is the following focal plane. If Π denotes an unaberrated pupil-plane electric field, then the electric field just before an entrance pupil in a plane A would be described as $\Psi_{A,-} = \Pi$. If there is no mask in this pupil plane, the light just after plane A would be the same and represented as:

$$\begin{aligned} \Psi_{A,+} &= \Psi_{A,-} \\ &= \Pi. \end{aligned} \tag{2.10}$$

Propagating through the lens to plan B would be represented as:

$$\begin{aligned} \Psi_{B,-} &= C\{\Psi_{A,-}\} \\ &= C\{\Pi\} \end{aligned} \tag{2.11}$$

where $C\{\cdot\}$ is a linear operator that propagates a field from the pupil to the focal plane, typically approximated with a Fraunhofer propagator.

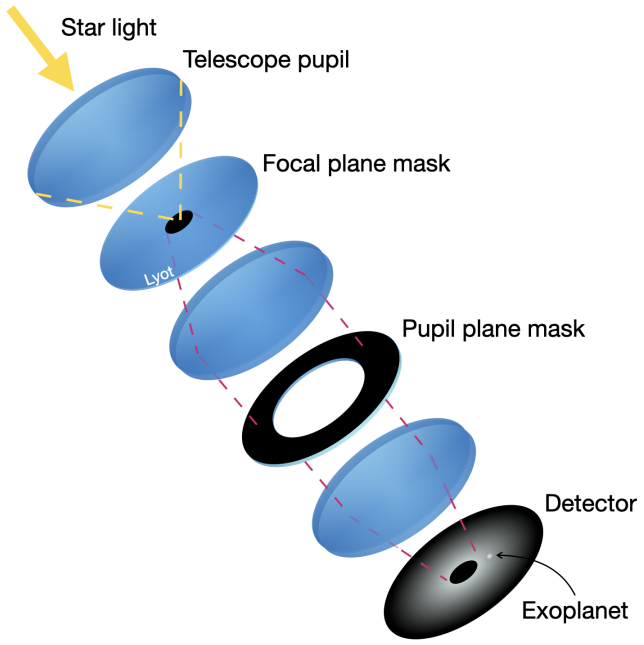

Figure 2.3: Components of a typical coronagraph instrument.

Any coronagraph can be ultimately represented by an operator that is linear since the light levels in a telescope are not strong enough to excite non-linear optical phenomena. This concept will be revisited in the next section.

2.2 The first coronagraph

The first coronagraph was invented in 1939 by French astronomer Bernard Lyot. Lyot's goal was to build a device which could image the Sun's outer edge, or the solar corona–hence the name 'coronagraph.' At the time, astronomers had to travel the world 'chasing' solar eclipses in order to image very close to the bright sun. Then Lyot developed the coronagraph as a series of masks and lenses inside the telescope to block the light of the solar disk. Figure 2.3 shows the general schematic for Lyot's coronagraph, employing both a focal-plane and pupil-plane mask. Using his coronagraph, Lyot became the first person to photograph the solar corona and prominences without an eclipse (Lyot, 1939). Since then, the general architecture of a coronagraph has remained essentially the same.

In the Lyot coronagraph, the light that enters the telescope aperture is focused onto a focal plane mask (FPM) which, when centered on a star, blocks most of the light.

At the first focal plane, the telescope's PSF forms an Airy pattern (as described in Equation 2.6 from Section 2.1). The Lyot FPM consists of an opaque spot designed to intercept most of the light concentrated in the PSF core. An undersized circular aperture (known as the Lyot stop) in the following pupil plane is used only to remove light that the hard edges of the Lyot spot FPM diffract mostly in a ring close to the pupil edge. The remaining light is focused to form the final coronagraphic image. Thus, the diffracted starlight is suppressed and faint objects neighboring a bright source can be observed. Lyot's original concept of the coronagraph still holds the record for the best contrast with an unobscured circular pupil in a laboratory setting presented by Seo et al. (2019) and is also in use on the James Webb space telescope (Boccaletti et al., 2022).

The coronagraph in its simplest form, as Lyot built it, uses an occulting mask in the focal plane of a telescope combined with an undersized pupil plane mask (Lyot, 1939). This architecture is the basis for many other coronagraphs which followed (discussed in Section 2.3). The light going through the Lyot coronagraph can be traced and also represented in the notation described at the end of Section 2.1. In this case, the focal plane B in Equation 2.11 contains a small opaque mask $M(\mathbf{k})$. Just after the FPM, the electric field will be:

$$\begin{aligned} \Psi_{B,+} &= M(\mathbf{k}) \cdot \Psi_{B,-} \\ &= M(\mathbf{k}) \cdot C\{\Pi\}. \end{aligned} \tag{2.12}$$

Just before the Lyot stop in the pupil plane C, the electric field is:

$$\begin{aligned} \Psi_{C,-} &= C^{-1}\{\Psi_{B,+}\} \\ &= C^{-1}\{M(\mathbf{k}) \cdot C\{\Pi\}\}. \end{aligned} \tag{2.13}$$

Babinet's principle can be applied here since it states that the diffraction pattern from an opaque body is identical to that from a hole of the same size and shape (Born and Wolf, 1980). Equation 2.13 can be rewritten as:

$$\Psi_{C,-} = \Pi - C^{-1}\{(1 - M(\mathbf{k})) \cdot C\{\Pi\}\}. \tag{2.14}$$

The next pupil plane contains the Lyot stop mask $L(\mathbf{x})$, which yields:

$$\begin{aligned} \Psi_{C,+} &= L \cdot \Psi_{C,-} \\ &= L \cdot [\Pi - C^{-1}\{(1 - M(\mathbf{k})) \cdot C\{\Pi\}\}], \end{aligned} \tag{2.15}$$

so the overall Lyot coronagraph operator $\mathcal{L}\{\cdot\}$ can be written as:

$$\mathcal{L}\{\Psi\} = L \cdot [\Psi - C^{-1}\{(1 - M(\mathbf{k})) \cdot C\{\Psi\}\}]. \tag{2.16}$$

Figure 2.4: Coronagraphic focal plane masks.

Since Lyot's initial coronagraph concept, considerable strides have been taken to improve coronagraph technology. New applications have demanded higher contrasts, and as telescopes have grown in size, the optical setup has become increasingly complex, necessitating more sophisticated coronagraphic systems. Modern telescopes typically incorporate a significant central obscuration supported by struts, leading to a noticeable leakage of stellar light through the coronagraph due to the more complex aperture. Moreover, the latest generation of telescopes feature segmented mirrors, further adding to the complexity.

2.3 Coronagraphic focal plane masks

However the Lyot coronagraph design suffers from two primary limitations. Firstly, the opaque mask only blocks the central portion of the Airy pattern. This allows the outer rings to propagate to the Lyot plane, resulting in residual starlight within the pupil, particularly intensifying towards the pupil edges. This issue can be partially mitigated by utilizing a substantially undersized Lyot stop, at the expense of reducing system throughput (desired signal from companions or other off-axis sources). Additionally, complex aperture shapes with central obstructions and struts produce a similar effect, which may be addressed by employing a Lyot stop tailored to the pupil shape, but which would also further reduce system throughput. Secondly, the occulting spot possesses finite dimensions, consequently obstructing faint sources in close proximity to the bright star. Reducing the size of the opaque mask expands the discovery potential, at the cost of diminishing achievable contrast. This measure of the closest angular separation from a star at which a coronagraph can effectively image objects is referred to as the inner working angle (IWA). It is defined as the distance at which 50% of the light of the companion is transmitted and is often reported in units of λ/D, where λ is the wavelength and D is the diameter of the primary mirror.

In pursuit of better starlight rejection at closer separations, transmissive FPMs employing phase shifts were developed. Figure 2.4 shows diagrams of the masks discussed throughout this section. The first design introduced by F. Roddier and C. Roddier (1997) involves using a phase mask instead of an occulting spot. This phase mask induces a π phase shift in the center, allowing for destructive interference of on-axis light and enhancing the detection range for planets near their host star. However, this mask's performance is limited by chromatic effects, particularly when used in broadband observations. The chromatic behavior stems from its design which incorporates a phase dimple that covers a specific area of the Airy disk. Although the physical size of the dimple remains constant, the size of the PSF changes with different wavelengths, causing the phase mask to function optimally only at its designated wavelength. Additionally, the phase dimple is typically constructed as a physical step in a dielectric substrate, resulting in chromaticity in the phase shift itself.

Soummer et al. (2003) attempted to address this issue by proposing a solution which introduces a second phase-shifted zone. This dual-zone phase mask incorporates an additional phase step in the central dimple, providing an opposite phase shift to mitigate chromatic effects. Instead of exhibiting excellent performance solely at the design wavelength and quickly degrading with wavelength deviation, the dual-zone phase mask rejects starlight well consistently across a 40% bandwidth.

Further phase-only FPM concepts were developed avoiding the use of a phase dimple. Rather than dividing the focal plane image into inner and outer rings with a phase shift of π, Rouan et al. (2000) partitioned it into four quadrants with the Four Quadrant Phase Mask (4QPM). Two adjacent segments within these quadrants have a relative phase difference of π. Light at the center in two diagonal quadrants destructively interferes with the light in the other two quadrants, each with a phase difference of π, thus producing the coronagraphic effect. Furthermore, the 4QPM's effectiveness is not influenced by the size of the PSF, making its design achromatic. This idea was further extended to the eight-octant phase mask (EOPM) by Murakami et al. (2008) with eight alternating sectors of π and 0 phase shifts instead of four.

However, the primary problem encountered with the 4QPM and the EOPM is that any planet lying on the transition between two sectors, would be cancelled due to destructive interference. To address this, the transition between sectors can be smoothed by adding additional steps at intermediate phases. This would reduce the phase shift between neighboring sectors and prevent potential companions from

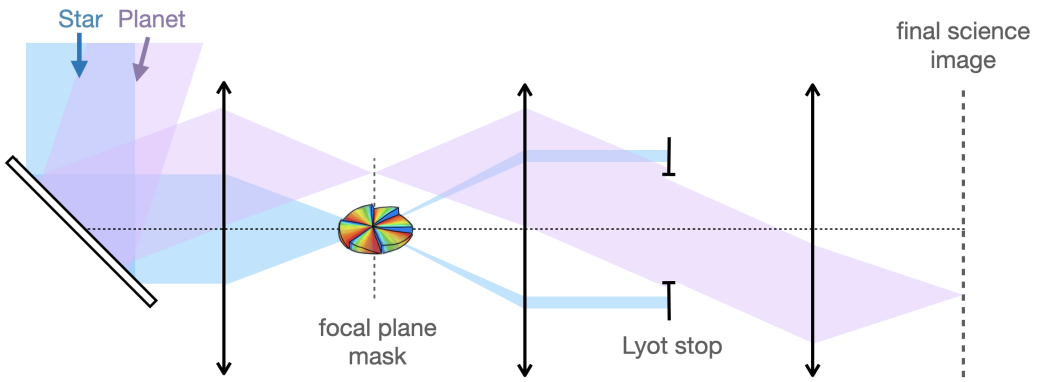

Figure 2.5: Optical schematic of a vortex coronagraph. The focal plane mask shown here is a charge 6 scalar vortex phase mask. Starlight is blocked by the vortex coronagraph and planet light is allowed through to the final science camera.

being canceled. Extending this concept further eventually leads to a smooth phase ramp first introduced formally in 2005 as the vortex phase mask (Mawet et al., 2005a; Foo et al., 2005). On-axis starlight is in theory perfectly rejected by the vortex coronagraph and any off-axis planet light is allowed through to the final science camera since it is not focused onto the center of the vortex phase pattern. A schematic of the vortex coronagraph is shown in Figure 2.5. Further explanation of the mechanism behind a vortex coronagraph is provided in the following section.

Alternative coronagraphic masks have been since proposed, such as the cosine or combinations of cosine and vortex topographies (Hénault, 2015). However the most promising FPM today for future exoplanet direct imaging missions is the vortex coronagraph. Over the last fifteen years, the vortex phase mask has been explored as a viable alternative to the classical Lyot coronagraph for high contrast imaging because it allows for higher throughput of planet light along with a smaller IWA and lower sensitivity to low-order aberrations (Swartzlander, 2005; Mawet et al., 2005a; Foo et al., 2005; Lee et al., 2006).

2.4 The vortex coronagraph

The core principle behind a vortex coronagraph involves the rejection of on-axis starlight through the introduction of a spiral phase pattern onto the incoming wavefront. Placing a vortex mask at the focal plane introduces an optical vortex phase ramp, $e^{il\theta}$, where θ represents the azimuthal angle, and l denotes the topological

charge, which is defined as the number of phase wraps. According to the principles of Fourier optics discussed in Section 2.1 a vortex with an even integer topological charge theoretically achieves perfect rejection of starlight (Swartzlander, 2005; Mawet et al., 2005a; Foo et al., 2005; Lee et al., 2006). More information about the derivation of the vortex rejection proof can be found in Mawet et al. (2005a).

The vortex phase ramp as a coronagraphic focal plane phase mask can be written in the operator notation described earlier with $V(\omega) = e^{il\omega}$ where ω is the azimuthal coordinate in the FPM and l is the topological charge. Start with the electric field of the incoming starlight Π as in Equation 2.10. In the focal plane, it is an Airy disk function assuming a circular entrance pupil of radius R_{tel} and it can be written:

$$C\{\Pi\} = \frac{2J_1\left(2\pi R_{\text{tel}} r\right)}{2\pi R_{\text{tel}} r}. \tag{2.17}$$

Propagating through the vortex mask, just after the FPM, the electric field will be:

$$\begin{aligned} \Psi_{B,+} &= V(\omega) \cdot \Psi_{B,-} \\ &= V(\omega) \cdot C\{\Pi\}. \end{aligned} \tag{2.18}$$

In the next pupil plane , just before the Lyot stop, the electric field is:

$$\begin{aligned} \Psi_{C,-} &= C^{-1}\{\Psi_{B,+}\} \\ &= C^{-1}\{V(\omega) \cdot C\{\Pi\}\}. \end{aligned} \tag{2.19}$$

The operator functions can be explicitly plugged in to express how the Lyot plane electric field is distributed:

$$\Psi_{C,-} = C^{-1}\{e^{il\omega} \cdot \frac{2J_1\left(2\pi R_{\text{tel}} r\right)}{2\pi R_{\text{tel}} r}\}. \tag{2.20}$$

Mawet et al., 2005a recognized the J_1 Bessel function here is actually subject to a lth order Hankel transform and yields an analytical solution for when the electric field is zero inside the pupil area.

$$\Psi_{C,-} = 0, \quad r < R_{\text{tel}} \text{ and } l = 2, 4, 6, \ldots \tag{2.21}$$

The vortex phase mask rejects the light entirely outside of the pupil area but perfect attenuation is only achieved if the topological charge l is an en even integer value.

Next the Lyot stop mask $L(\mathbf{x})$ can be used in that pupil plane to block all the light. Applying the Lyot stop operator the same way as Equation 2.15 gives:

$$\Psi_{C,+} = L \cdot \Psi_{C,-}. \tag{2.22}$$

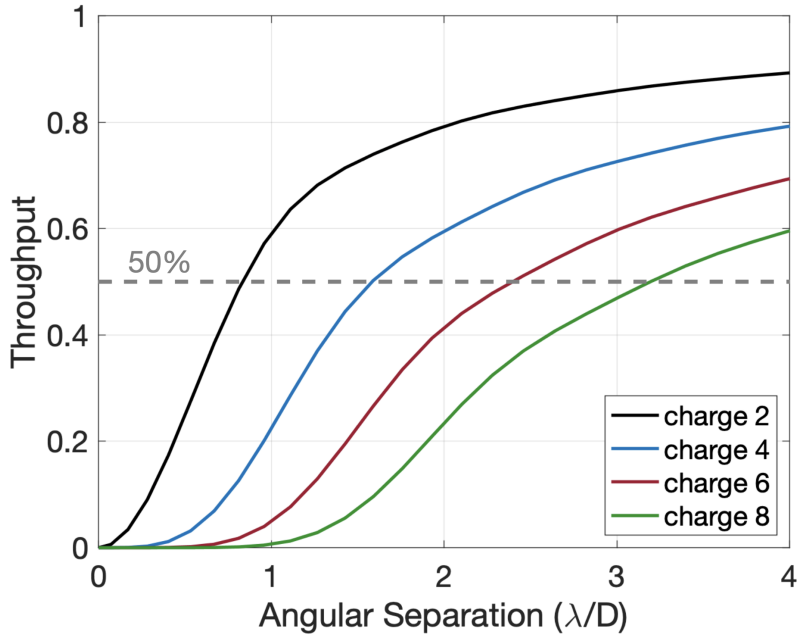

Figure 2.6: Simulated off-axis planet throughput for vortex coronagraphs of charge 2, 4, 6, 8. The dashed 50% transmission line intersects the various curves at the inner working angle for each vortex coronagraph.

The vortex coronagraph operator $\mathcal{V}\{\cdot\}$ can be written as:

$$\mathcal{V}\{\Psi\} = L \cdot [C^{-1}\{V(\omega) \cdot C\{\Pi\}\}]. \tag{2.23}$$

Figure 2.6 shows how vortex coronagraphs with charge $l = 2, 4, 6, 8$ provide different throughput. The lower topological charge vortex coronagraphs exhibit better IWAs but are also seen to demonstrate worse sensitivities to low-order aberrations (Ruane et al., 2018). This trade-off between IWA and aberration sensitivity drives the choice of topological charge for future space telescope missions, which is determined by the science goals. For the Habitable Worlds Observatory's (HWO) goal of directly detecting Earth-twins, a vortex charge $l = 6$ has the most suitable balance of inner working angle and insensitivity to low-order aberrations. This thesis will mostly focus on charge 6 vortex coronagraphs.

There are two main flavors of vortex coronagraphs: scalar (SVC) and vector (VVC) vortex coronagraphs. Both flavors of vortex coronagraphs apply a $e^{il\theta}$ phase ramp to the wavefront. The VVC utilizes a polarization-dependent geometrical phase shift, while the SVC relies on a wavelength-dependent longitudinal phase delay.

There has been significant progress made in the design, fabrication and testing of vector vortex masks in the last two decades. However, scalar vortex masks have not been studied in the same amount of detail. Here the current state of both vector and scalar vortex masks is reviewed.

Vector Vortex Achievements and Limitations

A vector vortex coronagraph is essentially a half-wave plate whose fast axis varies azimuthally. The characteristic of a half wave plate is that it induces a π phase shift between orthogonal polarizations, and an additional phase depending on its orientation. When arranged conveniently, this effect can be used to create the phase ramp of a vortex phase mask. The left diagram in Figure 2.7 shows an implementation of the polarization-dependent VVC where an incoming linear polarization is rotated by an angle of twice the azimuthal coordinate. A VVC with charge l effectively imprints a spiral phase ramp onto the incoming light, but creates two conjugated phase ramps $\exp(\pm il\theta)$ on the orthogonal opposite polarization states of the light. Equation 2.24 shows the Jones matrix in the circular polarization basis which demonstrates how the wavefront is modified by the vector vortex FPM, where c_V and c_L are constants.

$$\mathbf{M}_{\circlearrowleft} = c_V \begin{bmatrix} 0 & e^{il\theta} \\ e^{-il\theta} & 0 \end{bmatrix} + c_L \begin{bmatrix} 1 & 0 \\ 0 & 1 \end{bmatrix} \tag{2.24}$$

Here the first term indicates that a vortex phase ramp, $e^{\pm il\theta}$, is applied to each polarization component, where the sign of the vortex ramp depends on whether the incident circular polarization is right or left handed. Unpolarized light would result in the VVC imprinting two phase ramps of opposite helicity: $e^{+il\theta}$ and $e^{-il\theta}$. However, within a telescope instrument, the two polarization states accumulate distinct aberrations which complicate wavefront control.

This requires wavefront control in both polarizations independently, resulting in either splitting the two polarizations at the cost of increased complexity, or filtering one polarization at the cost of reducing the throughput. This dependence on polarization is the primary disadvantage of VVCs. One solution requires introducing a polarizer and an analyzer, ensuring that only one circular polarization reaches the focal plane (Mawet et al., 2011; Quesnel et al., 2022). Another solution is to basically duplicate the instrument for both polarizations by way of a polarizing beamsplitter. Although polarization filtering helps reduce the leakage term and isolate only one of the spiral phase ramps, it also effectively cuts the total throughput in half.

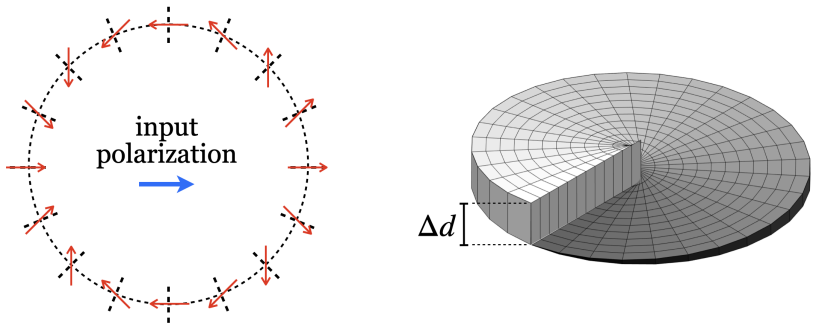

Figure 2.7: Two flavors of vortex coronagraphs: (left) Vector vortex coronagraphs implement a spiral phase ramp geometrically via rotation of the polarization (adapted from Mawet et al., 2011). (right) Scalar vortex coronagraphs vary the thickness or index of refraction to implement a phase ramp longitudinally.

Another limitation of the VVC is stellar leakage due to imperfect retardance of the half wave plate. The second term in Equation 2.24 is the stellar leakage component due to imperfect retardance. This leakage leads to a portion of the beam passing through the mask without acquiring the phase ramp which adds a scaled down, on-axis Airy pattern in the final image plane.

To address these limitations, VVC development in various implementations has received much attention throughout the last decade and VVCs have recently been installed in several ground based observatories. Successful implementations of vector vortex masks are often manufactured from liquid crystal polymers (Mawet et al., 2009a; Ganic et al., 2002), subwavelength gratings (Mawet et al., 2005b; König et al., 2023), photonic crystals (Murakami et al., 2013), or metamaterials (Devlin et al., 2017). On-sky demonstration and operation of VVCs at Palomar Observatory (Mawet et al., 2009b), Keck Observatory (Serabyn et al., 2017; Wang et al., 2020), Subaru Observatory (Kühn et al., 2018), and the VLT (Mawet et al., 2013) have proven the capabilities of vortex coronagraphs. Additionally, VVCs have already reached raw contrast levels of 1.6×10^{-9} at 10% bandwidth in testbed environment (Serabyn et al., 2019). Moreover, experimental testing and further development of vector vortex masks continues to push their potential for high contrast imaging of exoplanets (Serabyn et al., 2019; Ruane et al., 2020; Ruane et al., 2022; König et al., 2022).

The Potential of Scalar Vortex Coronagraphs

The primary motivation behind exploring scalar vortex coronagraphs is to circumvent the polarization-dependent limitation imposed by vector vortex masks. Contrary to VVCs which exploit the geometric phase shift, SVCs use longitudinal phase delays to imprint an optical vortex onto the incoming wavefront.

As seen in the right diagram in Figure 2.7, SVCs vary in either surface height or in index of refraction with respect to the azimuth to imprint the desired phase ramp on the wavefront. This is a significant advantage because it removes the need for polarization filtering, therefore retaining the total throughput.

To understand the wavelength dependence, we start with the general equations for the optical path difference (OPD) induced by any dielectric material in air with thickness Δd and index of refraction n.

$$\begin{aligned} \text{OPD} &= \Delta d\,(n - n_{air}) \\ &= \Delta d\,(n - 1) \end{aligned}$$

Now convert the OPD to phase delay ϕ and consider the wavelength dependence of the index of refraction $n(\lambda)$:

$$\phi = \frac{2\pi}{\lambda}\text{OPD}$$

$$\phi(\lambda) = \frac{2\pi}{\lambda}\Delta d\,(n(\lambda) - 1)\,. \tag{2.25}$$

To achieve the desired coronagraphic effect of the vortex at the design wavelength λ_0, the phase must be:

$$\phi(\lambda_0) = l_0\theta$$

where l_0 is the desired topological charge. Substituting this into Equation 2.25 and solving for $\Delta d(\theta)$ yields the scalar implementation of a vortex coronagraph, where n_0 is the refractive index at the design wavelength.

$$\Delta d(\theta) = \frac{l_0\lambda_0\theta}{2\pi(n_0 - 1)}$$

The effective phase of this SVC at any λ can be found by plugging this back into Equation 2.25:

$$\phi = \frac{\lambda_0}{\lambda} l_0 \theta \left(\frac{n(\lambda) - 1}{n_0 - 1} \right).$$

The chromaticity factor of the SVC can be seen here by the wavelength dependence of the phase. The index of refraction of the transmissive dielectrics commonly used in these applications does not vary significantly across the visible range ($n(\lambda) \approx n_0$). This leaves the SVC wavelength-dependent phase and transmission as:

$$\phi(\lambda) = l_0 \frac{\lambda_0}{\lambda} \theta \tag{2.26}$$

$$t = \exp\left(i l_0 \frac{\lambda_0}{\lambda} \theta \right). \tag{2.27}$$

As mentioned earlier in Section 2.4, an ideal vortex coronagraph requires the charge l to be a nonzero, even integer value for the starlight to be completely diffracted outside of the Lyot stop. At the design wavelength λ_0, an SVC creates a perfect optical vortex with a spiral phase ramp described by $e^{i l_0 \theta}$.

However, for light at any wavelength other than the design central wavelength λ_0, the effective charge of the vortex will vary. Essentially as the wavelength is offset from the central design wavelength, $\lambda \neq \lambda_0$, the effective charge becomes non-integer $l_{\text{eff}} = l_0 \frac{\lambda_0}{\lambda}$ and the SVC's ability to perform light suppression decreases–hence it is chromatic. This property is the primary limitation of SVCs and the reason why VVCs are generally preferred in current mission studies requiring effective starlight rejection across a broad band.

The earliest literature on SVCs dates back to Foo et al. (2005) and Swartzlander (2006) who explored the potential of scalar vortex coronagraphs and suggested possible limitations. Later, Swartzlander et al. (2008) reported the first demonstration of an SVC. More recently, Ruane et al. (2019) discussed the theoretical potential that SVCs offer, and Galicher et al. (2020) showed how phase wrapping of SVC topographies impacts the achromatic limitations discussed in Section 4.7.

One of the primary focuses of this thesis work is to assess the chromatic challenge of current SVC designs and investigate methods of achromatizing scalar vortex coronagraph masks. This led to several papers presenting the chromatic characterization of the wrapped staircase SVC (see Chapter 4, Desai et al., 2021 and Desai et al., 2023b), as well as new SVC topographies with promising broadband performance

(see Chapter 6, Desai et al., 2022, Desai et al., 2023a, and Desai et al., 2024). Further strategies to achromatize SVCs utilizing metasurface implementations are also currently being investigated in parallel by König et al. (2023) and Palatnick et al. (2023) and are discussed in Chapter 7.

Apodization with the vortex coronagraph

As explained in 2.4, the vortex coronagraph achieves theoretically perfect stellar rejection for circular pupils with no obstructions. However most large telescopes incorporate central obstructions and support structures due to their secondary mirrors. Furthermore, in the context of HWO, a segmented primary mirror has already been identified as the most likely configuration for a future space telescope mission focused on the direct imaging and characterization of exoplanets (National Academies of Sciences, Engineering and Medicine, 2021). The vortex coronagraph is a promising FPM to achieve the 10^{-10} target contrast ratio but it is well known that its performance suffers from large central obstructions and segment gaps since they cause unwanted diffracted starlight to leak through the coronagraph (Riggs et al., 2022).

To deal with these complex pupil shapes, amplitude and phase apodizers can be used together with the coronagraphic mask. Apodizers are pupil plane masks that modulate the incoming wavefront to redirect the light to specific regions in the focal plane. To correct for the effect of complex aperture shapes, apodizers will be crucial in order to bring the vortex coronagraph to the performance levels needed for future space telescope missions.

Apodizers have been used in the past to correct for the complex shape of typical telescope apertures. For example, a ring apodizer can restore the perfect starlight rejection capability of a vortex coronagraph in presence of a circular central obstruction (Mawet et al., 2013). Similarly, more complex pupil shapes including struts and segmented mirrors can be addressed by iteratively optimizing a pupil plane apodizer (Carlotti, 2013). Recently, both phase and amplitude apodizers have been tested in lab (Kenworthy et al., 2007; Pueyo et al., 2011; Riggs et al., 2022; Bertrou-Cantou et al., 2023). Other work considers combining apodizers with Lyot coronagraphs (N'Diaye et al., 2018) or with Roddier and Dual Zone phase mask coronagraph (Soummer et al., 2003).

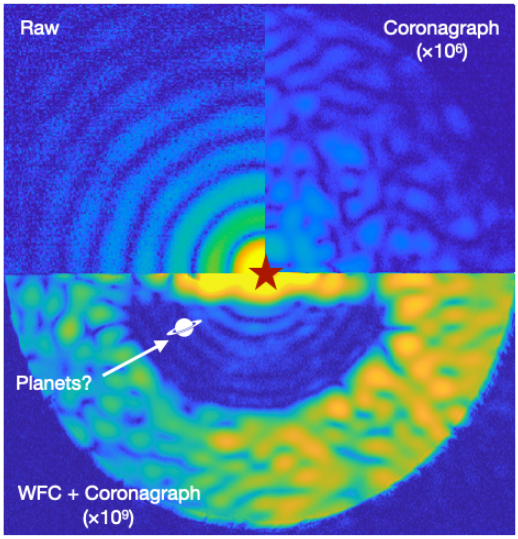

Figure 2.8: Experimental point spread function (PSF) representing raw stellar light (top left) and with a vortex coronagraph at 10^6 times brightness (top right), as well as after dark hole digging with wavefront sensing and control using a deformable mirror (bottom) from the In-Air Coronagraph Testbed at JPL.

2.5 The need for wavefront sensing and control

Although much progress has been made in the development of coronagraph masks, the direct imaging of exoplanets will require starlight suppression at 10^{10} levels and no coronagraph design has yet demonstrated this. Coronagraphy at these levels is extremely challenging and requires more than a precisely engineered and high performing coronagraphic mask. Small perturbations in the wavefront strongly affect the coronagraphic performance, and therefore need to be controlled to very high accuracy. From the ground, the main effect disturbing the incoming light is the atmospheric turbulence. But even from space, high-contrast imaging must overcome two major noise sources to successfully detect Earth-like planets around Sun-like stars: residual starlight from diffraction due to the telescope apertures, and speckle noise from starlight scattered by instrumentally-generated wavefront perturbations. Coronagraphs tackle only the residual starlight contribution by attenuating the starlight at the location of a planet. Speckle noise is addressed with wavefront sensing and control (WFSC) systems.

Speckle noise comes from optical imperfections or warping in the optics due to temperature changes over time, distorting the wavefront as it propagates through the optical system. The resulting (small) aberrations in the optics lead to starlight leaking

into the coronagraphic plane and create quasi-static speckles (slow-moving speckles compared to the fast-moving atmospheric speckles experienced from ground) which are challenging to distinguish from planets. The first quadrant of Figure 2.8 shows the raw laboratory PSF without any coronagraph/vortex. The second quadrant shows the residual light after introducing the vortex at a scale of 10^6 brightness. The image is clearly dominated by speckles, limiting the achievable raw contrast of the coronagraph.

The goal raw contrast requirement (10^{-10}) can be translated to engineering requirements on the spacecraft, e.g., tip/tilt sensitivities translate to pointing accuracy and vibration modes, low-order aberrations translate to mechanical stability of the primary mirror. For example, consider a phase perturbation $\delta\phi$ in the form of a sinusoid with amplitude h, where u is the spatial coordinate:

$$\delta\phi = \frac{2\pi}{\lambda} h \cos u.$$

The intensity of this phase aberration would be proportional to

$$I_{\text{speckle}} = |\mathcal{F}[\delta\phi]|^2 \propto \left(\frac{\pi h}{\lambda}\right)^2.$$

For HWO, this speckle intensity must be maintained at less than 1×10^{-10}. This translates to a stability requirement of:

$$\left(\frac{\pi h}{\lambda}\right)^2 < 10^{-10}$$

at $\lambda = 500$ nm,

$$\frac{\pi h}{5 \times 10^{-7}\text{m}} < 10^{-5}$$

$$h < \sim 1.5 \text{ pm}.$$

In order to directly detect planets at 10^{-10} contrasts, picometer level stability will be required for HWO. This extreme precision necessitates highly effective and efficient control of wavefront phase and amplitude.

Coronagraph instruments now incorporate deformable mirrors (DMs) in closed loop to correct for instrumental aberrations and create a 'dark hole,' i.e., a speckle-free dark region in which to search for stellar companions. The most commonly used DMs in high contrast imaging are micro-electro-mechanical systems (MEMS) DMs.

They consist of a reflective continuous membrane supported by actuators arranged in a pattern of constant spacing which can be pushed or pulled to a precision of 1 nanometer or less (BMC, 2024). The bottom half of Figure 2.8 shows the impact of focal plane WFSC with a DM to remove the speckles and achieve contrast at the level of 10^{-9}.

Establishing a dark hole region at 10^{-10} contrast levels requires precise sensing and control of the electric field (E-field). For adaptive optics systems on ground-based telescopes, wavefront sensing is performed by splitting the light and using an external wavefront sensor. This ensures enough photons are captured to perform real time correction ($\sim$ 1kHz) of the atmospheric turbulence. However, this creates non-common path aberrations, which are critical issues in wavefront sensing, and would prevent the system from achieving the required contrast levels. Instead, the principle of focal plane wavefront sensing is that high contrast is best achieved by avoiding all possible non-common errors that arise from path or wavelength differences. The controller is provided with an estimate of the electric field at the final image plane, rather than from a measurement taken by a separate wavefront sensor. Figure 2.9 shows WFSC in a closed loop with an external wavefront sensor and the resulting non-common path aberrations on the left, and with a focal plane wavefront sensor on the right. The three principal methods used to sense the image plane electric field in high-contrast imaging are Gerchberg-Saxton solutions (Gerchberg, 1972; Fienup, 1982), differential fringe imaging, such as the self-coherent camera or pinhole masks (Baudoz et al., 2006; Mazoyer et al., 2013), and DM probing (Bordé and Traub, 2006; Give'on et al., 2007). The scope of this thesis focuses only on the self-coherent camera and DM probing methods.

Overall, the control loop around the DMs and the final science image enables the estimation and control of the wavefront to create a dark hole through a process referred to as 'dark hole digging' (Malbet et al., 1995).

Dark hole digging algorithms

Malbet et al. (1995) first introduced how principles from adaptive optics can be applied to cancel the scattered light in the focal plane using a dark hole algorithm. The control algorithm drives the actuators of the DM to suppress the light at low spatial frequencies and reduce the scattering level near the optical axis by estimating the wavefront and applying the opposite shape to a DM in a preceding pupil plane. This phase conjugation method minimizes the difference between the shape of the

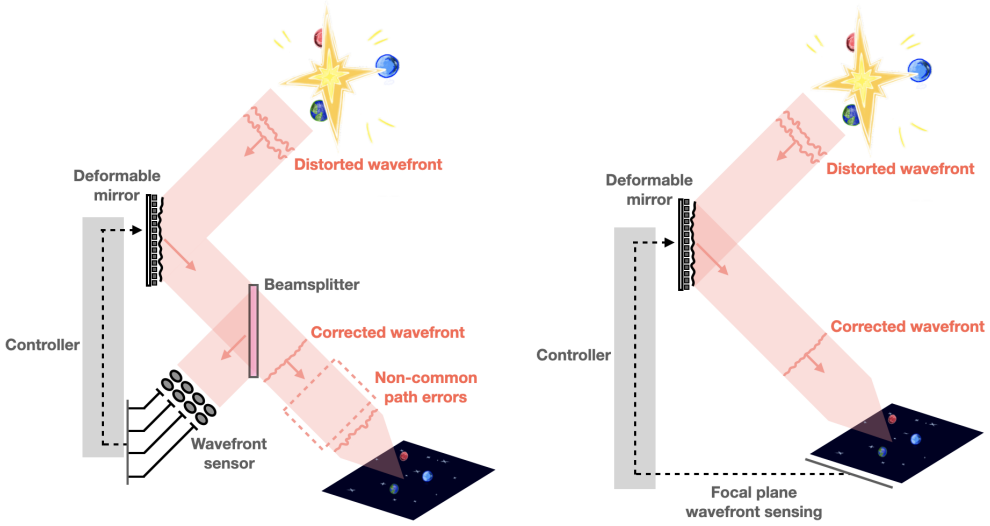

Figure 2.9: Wavefront sensing and control with an external wavefront sensor leading to non-common path aberrations (left) or with focal plane wavefront sensor without non-common aberrations (right).

DM and the shape of the low-pass filtered phase aberration at the plane of the DM. However, at very deep contrasts, wavefront errors can arise from both phase and amplitude errors, while a single pupil plane DM can only correct for phase aberrations. A second out-of-pupil DM is therefore needed for very high contrasts.

Bordé and Traub (2006) followed up on this work with the development of two alternative approaches: speckle nulling and energy minimization. Speckle nulling minimizes the intensity in the image plane one speckle at a time. It does not require an estimate of the electric field and, therefore, only closes the loop on intensity images. Speckles are then singled out in the image and suppressed by adding the sinusoidal component to the DM shape corresponding to the location of the speckle. Energy minimization in the form presented by Bordé and Traub (2006) on the other hand, finds the actuators' heights that minimize the total energy in the image plane.

Give'On (2009) formalized all these most commonly used high contrast correction methods, grouping phase conjugation, speckle nulling and energy minimization as all special cases of electric field conjugation (EFC). Give'on et al. (2007) also extended the EFC methodology to correct over a wider wavelength range using several estimates of the electric field at different wavelengths in the band.

Give'on et al. (2007) furthermore considered uncertainties in the model of the system and estimation errors, and introduced a solution for the actuator heights that

minimizes the total energy in the system. Lastly, extensions to EFC with multiple DMs (where some are not in the pupil plane) were proposed in order to correct for both amplitude and phase aberrations. A second DM also allows full correction in a 360 degree field of view around the star (Bordé and Traub, 2006).

2.6 Electric field conjugation theory

The EFC algorithm is divided into two parts: estimation of the wavefront and its correction. The complex electric field amplitude in the image plane is estimated, then the estimate is used to determine a correction to be applied to the DM actuators.

If P_1 and P_2 are defined as two planes along the optical path of the system, their corresponding complex-valued electric fields are E_1 and E_2. For high contrast imaging systems, P_1 is typically at a re-imaged pupil plane in the system and P2 is at the final image plane where the detector is placed.

Let C be the complex-valued transformation of electric fields between P_1 and P_2 so

$$E_2 = C\{E_1\}.$$

For a general given imaging system, the corrected electric field (including the effect of the aberrations and the effect of the DM) at P_2 is modeled as

$$\begin{aligned} E_2 &= C\{Ae^{\alpha+i\beta}e^{i\phi}\} \\ &\approx C\{Ae^{\alpha+i\beta}\} + iC\{A\phi\} \\ &= E_{ab} + iC\{A\phi\} \\ &= E_{ab} + G\overline{a} \end{aligned}$$

where A is the ideal, uncorrected electric field, α and β are the real-valued amplitude and phase aberrations, respectively, and ϕ is the real-valued shape of the DM.

Here G is a linear operator describing the effect of the DM and $\overline{a}$ are the coefficients when G is decomposed into a set of basis functions. When the influence function of the DM is used as the basis set, $\overline{a}$ are the actuator heights.

The goal of EFC is to find a solution for the DM actuator heights that sets the total electric field in the image plane to zero, or $E_2 = 0$.

This means $\overline{a}$ must be set so that

$$G\overline{a} = -E_{ab}.$$

Since a real-valued solution is needed for $\overline{a}$, this complex-valued equation can be separated into real and imaginary parts:

$$\bar{a} = -\begin{bmatrix} \Re\{G\} \\ \cdots \\ \Im\{G\} \end{bmatrix}^{-1} \begin{bmatrix} \Re\{E_{ab}\} \\ \cdots \\ \Im\{E_{ab}\} \end{bmatrix}.$$

The left matrix is over-determined so least squares-based methods (such as the Singular Value Decomposition) can be used to find a solution.

The solution minimizes the total energy for the linearized model and is within the space of solutions, X (defined by the propagation function):

$$\bar{a}^* = \arg\min_{\bar{a}\in X} \|E_{ab} + iC\{\phi\}\|^2 .$$

In order to find a multi-wavelength solution for the actuators, an estimate of E_{ab} at different wavelengths is necessary:

$$\bar{a} = -\begin{bmatrix} \Re\{G(\lambda_1)\} \\ \cdots \\ \Im\{G(\lambda_1)\} \\ \cdots \\ \Re\{G(\lambda_2)\} \\ \cdots \\ \Im\{G(\lambda_2)\} \\ \vdots \\ \Re\{G(\lambda_k)\} \\ \cdots \\ \Im\{G(\lambda_k)\} \end{bmatrix}^{-1} \begin{bmatrix} \Re\{E_{ab}(\lambda_1)\} \\ \cdots \\ \Im\{E_{ab}(\lambda_1)\} \\ \cdots \\ \Re\{E_{ab}(\lambda_2)\} \\ \cdots \\ \Im\{E_{ab}(\lambda_2)\} \\ \vdots \\ \Re\{E_{ab}(\lambda_k)\} \\ \cdots \\ \Im\{E_{ab}(\lambda_k)\} \end{bmatrix}.$$

Now, the least-squares solution finds the actuator heights that minimize the intensity of light in the image plane over all the wavelengths:

$$\bar{a}^* = \arg\min_{\bar{a}\in X} \sum_k \|E_{ab}(\lambda_k) + iC\{\phi\}\|^2 .$$

Model-based and model-free methods

There are many ways to apply EFC in practice for wavefront control with coronagraph systems. Recently, various new EFC methods have emerged, holding potential

applications for the HWO mission concept. This thesis work focuses on three such methods and the experimental results from implementing these techniques are presented in Chapter 5.

The first method discussed in this thesis is the strictly model-based dark hole digging technique known as pairwise probing with electric field conjugation (PWP + EFC) (Give'on et al., 2007). The effectiveness of PWP + EFC relies on an accurate model of the coronagraph. It uses a model to estimate and directly minimize the E-field inside the dark hole (E_S). The other two methods are model-free dark hole digging approaches using different wavefront sensing approaches. The second method is the self-coherent camera (Baudoz et al., 2006) with EFC (SCC + EFC). It introduces a pinhole in the pupil plane, then measures the intensity of the resulting interference fringes within the dark hole (I_-) and aims to minimize it. The third method is implicit electric field conjugation (iEFC) (Ruffio and Kasper, 2022; Haffert et al., 2023). It uses pairwise probes on the DM to measure changes in intensity (dI) in the final science image dark hole region and aims to minimize that change. Both SCC + EFC and iEFC operate without an optical model of the system.

These dark hole digging algorithms can be categorized as either model-free or model-based, yet their common goal is to efficiently reduce the starlight within a specified region in the final focal plane. Here the terms 'model-based' and 'model-free' refer to whether a numerical simulated model of the optical system is necessary or not.

The matrix in Figure 2.1 shows that, despite the different naming conventions among these three dark hole digging algorithms, all three are methods of conjugating the electric field. They differ in implementation and wavefront sensing techniques. More fundamentally, these methods differ in which quantity they are measuring and minimizing within the dark hole region.

The general cost function is presented in Equation 2.28, illustrating how EFC aims to effectively minimize the sum of a quantity proportional to the estimated E-field in the final science focal plane, χ, the product of the DM commands, u, and the Jacobian, G.

$$J = min\left[|Gu + \chi|^2\right] \tag{2.28}$$

Dark Hole Digging Algorithms

	Wavefront Sensing Methods	
	Pairwise Probing	Self-coherent Camera
Model-based	PWP + EFC	/
Model-free	iEFC	SCC + EFC

Table 2.1: Matrix of various techniques of electric field conjugation split by their wavefront sensing methods and whether they require a system model. Pairwise probing (PWP) + electric field conjugation (EFC), self coherent camera (SCC) + electric field conjugation, and implicit electric field conjugation (iEFC) shown in the matrix are all dark hole digging methods implemented in this study. Note a model-based hybrid SCC has been partly investigated in (Mazoyer et al., 2013).

The variable $\mathcal{X}$ is intentionally retained as a placeholder, as this quantity varies among the three WFSC methods discussed here. The objective of the algorithm is to determine the DM commands, u, that null the total E-field in the image plane.

Pairwise Probing + Electric Field Conjugation

The conventional PWP + EFC algorithm has achieved the best contrast demonstrated to date on the Decadal Survey Testbed at JPL (Seo et al., 2019). Introduced as simply 'EFC' by Give'on et al. (2007), EFC minimizes the sum of the estimated E-field in the final science plane and the E-field due to the corrective elements throughout the system.

This model-based technique can be separated into a wavefront sensing technique (PWP) and a control algorithm (EFC). The wavefront sensing is done by applying pairwise sinc function probes (+/-) to the DM and measuring the final focal plane image. This can then be used with the model of the entire optical system to determine the best estimate of the speckle electric field, E_S.

The control step involves first forming the Jacobian G_{EFC} by moving each actuator of the DM in simulation to record the induced focal plane E-field. The Jacobian is inverted and combined with the E-field estimate to iteratively compute the DM commands that minimize E_S inside the correction region.

Effectively Equation 2.28 becomes:

$$J = min \left[|G_{\mathrm{EFC}} u + E_S|^2 \right] \tag{2.29}$$

where $G_{\mathrm{EFC}} = \partial E_S / \partial u$ and can be created entirely from the model of the system. PWP + EFC would not require any images per mode to build the Jacobian but a minimum of two probes hence four images per iteration for each subband.

Self-Coherent Camera + Electric Field Conjugation

The concept of the classical SCC was conceived by Baudoz et al. (2006). Since then it has been mainly implemented on the Très Haut Dynamique bench (THD) at the Paris Observatory (Baudoz et al., 2018; Potier et al., 2020) which demonstrated contrast performance around 10^{-9} in-air with a Four Quadrant Phase Mask coronagraph (Rouan et al., 2000).

Figure 2.10 shows the optical system required for closed loop WFSC with the SCC. Like the conventional PWP + EFC, this model-free dark hole digging technique can also be broken into a wavefront sensing method (SCC) and a control algorithm (EFC). Wavefront sensing with the SCC works by introducing a pinhole in the Lyot plane at a location where coherent starlight rejected by the coronagraphic mask lands.

The pinhole creates a reference channel which interferes with any residual starlight leaking through the image channel, thereby creating fringes at the final focal plane. The right panel of Figure 2.10 shows an example final science image with and without fringes where the speckle pattern of starlight through the coronagraph and the dark hole region where the speckles have been partially suppressed are visible.

In principle, this fringed image contains all the information needed to estimate the unwanted E-field in the coronagraphic image. Figure 2.11 shows the SCC Lyot stop with the pinhole and reference channel, the resulting fringes in the final image plane due to the additional pinhole, and the Fourier transform of the fringed imaged.

The light in the fringed SCC image can be described by the E-fields that each pass through the reference or Lyot channel. Let A_S be the complex electric field of the speckles in the Lyot channel which we want to estimate and minimize. A_C is the complex electric field of a potential companion (also in the Lyot channel). A_R is the complex electric field associated with the SCC reference hole.

Since the stellar light through the pinhole is coherent with the stellar speckles through the Lyot channel, A_S and A_R interfere, resulting in fringes. However any light from

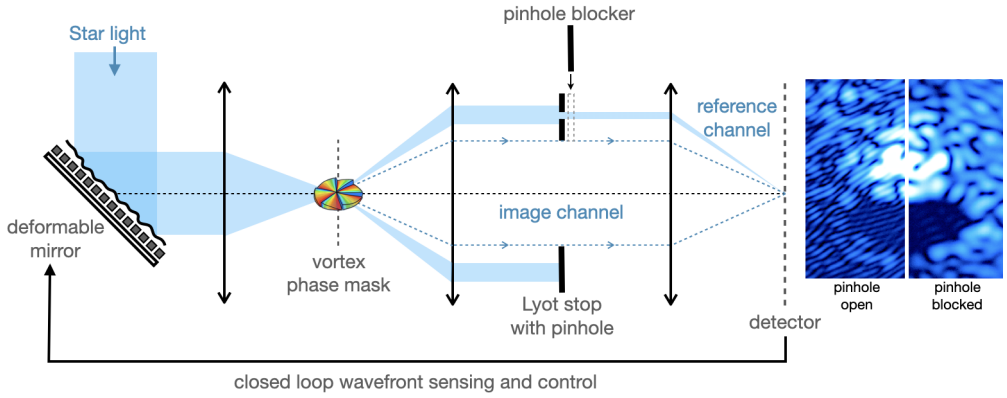

Figure 2.10: Diagram of optical layout for the self-coherent camera and electric field conjugation. The self-coherent camera technique uses the pinhole blocker to open and close the reference channel to obtain the fringed (left) and unfringed (right) final focal plane images.

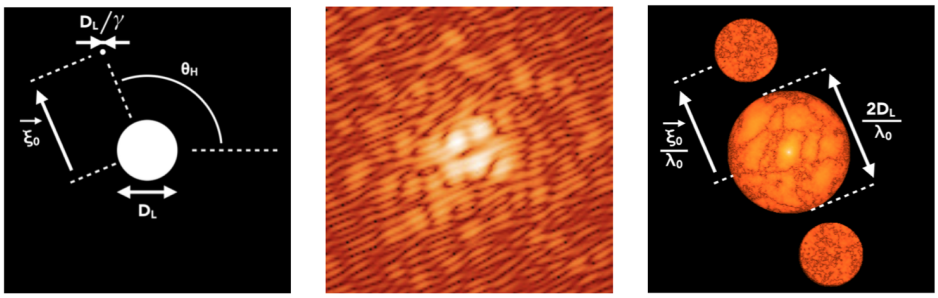

Figure 2.11: Diagram of SCC Lyot stop with pinhole, fringed final focal plane image, and Fourier transform of the fringed image with central lobe and two side lobe (from Delorme et al., 2016).

a companion A_C would not be coherent with the reference beam or stellar speckles, so it would not be fringed.

The intensity I in the fringed image can be written as follows (Baudoz et al., 2006):

$$I(\vec{\alpha}) = |A_S(\vec{\alpha})|^2 + |A_C(\vec{\alpha})|^2 + |A_R(\vec{\alpha})|^2 + 2\,\mathrm{Re}\left[A_S(\vec{\alpha})A_R^*(\vec{\alpha})\exp\left(\frac{2i\pi\vec{\alpha}\cdot\overrightarrow{\xi_0}}{\lambda_0}\right)\right]$$

where $\vec{\alpha}$ is the focal plane coordinate and $\overrightarrow{\xi_0}$ is the separation between the classical Lyot stop and the SCC reference pinhole, and A_R^* is the conjugate of A_R.

To differentiate the fringed speckles from the companion a numerical Fourier transform is applied:

$$\begin{aligned}\mathcal{F}^{-1}[I](\vec{u}) = \mathcal{F}^{-1}\left[|A_S|^2 + |A_C|^2 + |A_R|^2\right] * \delta(\vec{u}) \\ + \mathcal{F}^{-1}\left[A_S^* A_R\right] * \delta\left(\vec{u} + \frac{\overrightarrow{\xi_0}}{\lambda_0}\right) \\ + \mathcal{F}^{-1}\left[A_S A_R^*\right] * \delta\left(\vec{u} - \frac{\overrightarrow{\xi_0}}{\lambda_0}\right)\end{aligned}$$

where $\vec{u}$ is the spatial frequency plane coordinate.

The first term corresponds to the sum of the autocorrelations of the electric field in the classical Lyot stop and in the reference hole. The other two terms are conjugates and correspond to the correlation between the stellar electric fields in the classical Lyot stop and in the reference hole. Each represents one of the three lobes shown in the Fourier transform image in the right panel of Figure 2.11.

The radius of the central lobe is D_L/λ_0 and the radius of the two side lobes is $D_L(1 + 1/\gamma)/(2\lambda_0)$ based on the configuration of the pinhole in the Lyot stop (in the left panel of Figure 2.11).

These lobes will not overlap if the separation $||\vec{\xi}_0||$ between the classical Lyot stop and the SCC reference hole is large enough (Galicher et al., 2009):

$$\left\|\vec{\xi}_0\right\| > \frac{D_L}{2}\left(3 + \frac{1}{\gamma}\right).$$

To estimate the complex electric field A_S, one of the side lobes is cropped and Fourier transformed to give the fringe intensity (I_-):

$$I_- = A_S A_R^*.$$

Finally, I_-, which is proportional to the speckle E-field, is then minimized in the control step. The control step follows almost the same EFC procedure when paired with SCC as with PWP, except the Jacobian (G_{SCC}) is data-driven.

Effectively Equation 2.28 becomes:

$$J = min\left[|G_{\mathrm{SCC}}u + I_-|^2\right] \tag{2.30}$$

where $G_{\mathrm{SCC}} = \partial I_-/\partial u$ and is created by actuating the DM and measuring the SCC response as explained above. After systematically building this matrix, the estimate

from the wavefront sensing and the Jacobian are combined to iteratively control the DM to minimize I_- inside the dark hole. SCC + EFC would require a minimum of two images (+/-) per mode to build the Jacobian and one image per iteration for each subband.

There are several variations of SCC wavefront sensing which can be applied to obtain the I_- mentioned above. The classical SCC relies on the Fourier transform of the fringed image to get an estimate for the final E-field (Galicher et al., 2009; Mazoyer et al., 2013; Delorme et al., 2016). Building off the classical SCC, two simple modifications further improve its wavefront sensing capabilities and were implemented in this study for broadband experiments.

The first variation is based on Thompson et al. (2022). Instead of using the Fourier transform to extract the fringe intensity, the closed pinhole image (unfringed) is subtracted from the opened pinhole image (fringed) to retain the fringe intensity I_-. Although the wavefront sensing is improved, this variant takes longer to build the Jacobian since two images are required to estimate the E-field where classical SCC needs only one. This variant allows for the use of a field stop, which poses a significant challenge in classical SCC. This is because classical SCC relies on the Fourier transform which would be distorted by introducing a field stop. This variant also offers the ability to use pinholes closer to the science channel which potentially extracts more light for wavefront sensing (Martinez, 2019).

The second variation opens multiple pinholes instead of just one. This multi-reference SCC method is based on Delorme et al. (2016). With a single pinhole, the fringe contrast is reduced due to chromatic blurring away from the central fringe. With three pinholes in the Lyot stop, all at the same radius away from the center, overlapping fringes are created in different directions in the coronagraphic image, increasing the area of high contrast fringes. Delorme et al. (2016) demonstrated that such a design can be used to enhance SCC broadband capabilities. Hence, for this study it was implemented to effectively increase the amount of light in the reference channel and allow for improved wavefront sensing across the 10% bandwidth. Section 5.6 provides an experimental comparison between these SCC variants and shows that the three pinhole technique without the Fourier transform demonstrates the most efficient WFSC of the broadband SCC methods.

Implicit Electric Field Conjugation

Implicit electric field conjugation (iEFC) was presented formally by Haffert et al. (2023) and has recently become more commonly implemented on high contrast imaging benches for its appeal as a model-free version of conventional PWP + EFC. Unlike the other two dark hole digging methods presented in this paper, iEFC cannot be split into wavefront sensing and control, as the two occur concurrently.

The first step of iEFC involves applying a set of (+/-) Fourier modes to the DM with superimposed (+/-) pairwise probes. The difference in intensity, (dI), from the probe measurements is used to build the Jacobian, G_{iEFC}. Then, identical pairwise probes are applied to the DM at each iteration to measure the difference in intensity (dI) in the correction region. This quantity, proportional to the speckle E-field, is therefore minimized when multiplied with the inverse of the initially calibrated Jacobian.

Effectively Equation 2.28 becomes

$$J = min\left[|G_{\mathrm{iEFC}}u + dI|^2\right] \tag{2.31}$$

where $G_{\mathrm{iEFC}} = \partial(dI)/\partial\alpha$. One of the unique advantages of iEFC is that it requires no additional optics or hardware since the primary wavefront sensing technique is PWP involving the DMs. iEFC would require a minimum of two probes, so eight images per mode to build the Jacobian and four images per iteration for each subband. These repeated exposures can be a lengthy process in practice and is perhaps the biggest drawback of existing iEFC implementations.

2.7 Post-processing techniques

Even with WFSC correction, exoplanet direct imaging often requires sophisticated post-processing techniques to enhance the detection of the signal from the planet and distinguish it from speckles. Although not explored in this thesis, it is important to understand how current post-processing techniques build on coronagraph starlight suppression ability. There are three predominant methods which work hand-in-hand with the coronagraph system and the WFSC correction:

Angular Differential Imaging (ADI): Angular differential imaging works by acquiring multiple images of the target area at different telescope roll orientations or 'angular diversity' relative to the star. By taking these images and carefully aligning and subtracting them, the speckle noise can be subtracted while preserving the exoplanet signal, which remains fixed relative to the star. ADI is particularly effective

for detecting faint exoplanets at wide separations from their host stars (Marois et al., 2006; Lafreniere et al., 2007).

Reference Differential Imaging (RDI): In reference differential imaging, the speckle noise is addressed by obtaining an additional PSF from a similar nearby star. These reference images help characterize and subtract the speckle noise more accurately, improving the sensitivity to faint exoplanets. RDI is especially useful for detecting exoplanets located close to their host stars where the angular separation is small (Lafrenière et al., 2009).

Spectral Differential Imaging (SDI): Spectral Differential Imaging is a technique that exploits differences in the wavelength-dependent behavior of starlight and planet light. It involves obtaining images of the planet at multiple wavelengths, typically using narrow-band filters or integral field units. Since the planet's spectrum can differ from that of the star, SDI allows the two to be distinguished and suppresses the starlight while preserving the planet's signal (Sparks and Ford, 2002; Smith, 1987; Racine et al., 1999). SDI can be combined with other techniques like ADI or RDI for even better results, especially for detecting faint exoplanets with distinct spectral features.

These techniques, often used in combination, play a crucial role in extracting exoplanet signals from direct imaging observations. Their performance needs to be considered in conjunction with focal plane WFSC capabilities for future coronagraph design and technology development for direct exoplanet imaging.

2.8 System level coronagraph architecture

Future development of coronagraphs demands a holistic approach that considers not only individual components but also their integration into the broader telescope system. To achieve contrast levels of 10^{-10}, progress in coronagraphy specifically necessitates advancements in two key areas: the design of well-engineered FPMs and the development of effective WFSC methods.

These two directions must progress in tandem, with each informing the other to maximize the potential for achieving high-contrast imaging capable of detecting even fainter or rocky planets. By recognizing the interplay between WFSC algorithms and the FPM or coronagraph system, the effectiveness of coronagraph mask design

can be enhanced and in addition, techniques for maintaining dark hole stability during extended observations and even post-processing can be improved.

Consideration of system-level requirements, such as sensitivity to low-order wavefront aberrations, is crucial. For instance, while a lower vortex charge FPM may offer superior inner working angle, it is not suitable for current space telescopes due to its sensitivity to low-order aberrations conflicting with stability requirements. Another example of a system-driven requirement is that most coronagraph's practical implementations will necessitate the use of an apodizer when combined with a segmented mirror system. Moreover, certain wavefront sensing techniques, like the self-coherent camera, necessitate early integration into coronagraph design due to their hardware requirements, such as a custom Lyot stop with pinholes. Integrating advancements in FPMs and WFSC methods in a coordinated manner enables the development of coronagraphs capable of achieving groundbreaking contrast levels and revolutionizing exoplanet imaging.

Chapter 3

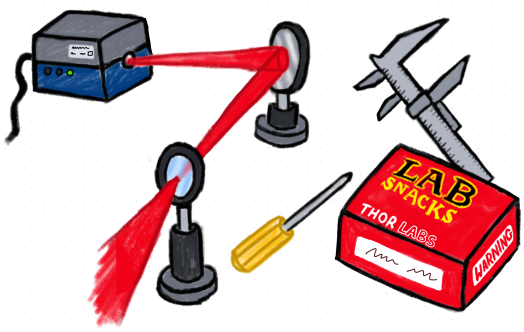

METHODS FOR DEVELOPING SCALAR VORTEX MASKS

3.1 Motivation

This chapter presents the problem statement and research approach of this thesis, as well as the simulation and experimental tools used in this work. The engineering requirements in this problem statement are derived from the exoplanet science goals discussed in Chapter 1. The simulation and experimental tools used for mask development and testing employ the coronagraphy theory discussed in Chapter 2 and are referenced throughout the remaining chapters of this thesis. These tchniques and analysis tools were developed to further our understanding of scalar phase mask capabilities and limitations as well as yield novel designs suitable for exoplanet direct imaging.

3.2 Thesis problem statement

In the context of the Habitable Worlds Observatory (HWO), a coronagraph capable of achieving 10^{-10} contrasts will require not only extremely precise and well developed wavefront sensing and control methods, but also high performance focal plane masks. The goal of this work is to develop scalar vortex coronagraph (SVC) designs capable of pushing the contrast toward 10^{-10} across a 20% bandwidth and demonstrating low sensitivity to low-order aberrations, all without compromising throughput at a small inner working angle (IWA). This thesis investigates new scalar

vortex concepts first in theory, then simulation, and finally implemented in the lab to be compared against existing technologies.

3.3 Research approach

Towards the pursuit of developing a scalar vortex coronagraph suitable for exoplanet direct imaging on a space telescope, this thesis work involved using the theory of coronagraphy and of wavefront sensing and control (discussed in Chapter 2) to develop new SVCs.

To address this objective, several intermediary questions were identified, each with corresponding methods of investigation. Firstly, the chromatic behavior of simple SVC devices needs to be assessed. This is done through metrology and experimental measurement of wavelength dependence. Secondly, the potential to enhance broadband performance of an SVC by altering its topography is explored via simulations of various focal plane mask (FPM) designs. Lastly, alternative approaches to designing an achromatic scalar vortex phase mask are considered, aiming to broaden the understanding and capabilities of SVC technology.

The techniques developed for this thesis work involve a combination of optical modeling and experimental testing on high contrast imaging testbeds. Simulation tools and the custom pipeline were developed for performance prediction of novel coronagraph mask designs. Additionally, the High Contrast Spectroscopy Testbed (HCST) and In-Air Coronagraph Testbed (IACT) are utilized for performance evaluation to characterize novel fabricated FPMs and assess their starlight suppression performance. Evaluation metrics such as contrast profiles and chromaticity V-curves are determined for standardized comparisons. This research and development process for investigating novel scalar vortex coronagraphs is iterated in this thesis towards the goal of finding a viable achromatic scalar vortex coronagraph solution to reach the contrast, aberration sensitivity, and bandwidth requirements of future exoplanet direct imaging space telescope missions.

3.4 Simulation methods

The goal of the simulation work in this thesis was to model existing coronagraph designs and investigate the potential of novel designs. By creating a simulation platform that describes the physical behavior of light passing through each optical element in the system, various coronagraph topographies could be tested for their chromatic behavior, robustness to low-order wavefront aberrations, and overall light suppression performance.

Building off of existing codebases designed for coronagraph development, I developed a wavefront propagation pipeline customized for designing, testing, and assessing novel SVC topographies. I also developed a modal decomposition analysis tool to predict the performance of some SVC topographies without the need for full 2D wavefront propagation modeling. These tools were critical to the scalar vortex coronagraph development carried out in this thesis and as a result they are now also being used by collaborators investigating alternate implementations of scalar vortex coronagraphs.

FALCO simulation tools

The Fast Linearized Coronagraphic Optimizer (FALCO)[1] is a software package for high contrast coronagraphy development. Specifically, it is designed to precisely simulate wavefront control as would be performed by a high contrast imaging testbed in a laboratory, and is furthermore used in the laboratory to perform the various wavefront control algorithms. To do this, the FALCO codebase contains many functions for describing standard optical elements of a coronagraph (point sources, pupils, apodizers, deformable mirrors, lenses, etc). For the purpose of modeling high contrast testbeds useful for laboratory experiments, it has three types of optical models for every element of the coronagraph: full, compact, and Jacobian. The full model represents the true physics of a testbed, whereas the compact model represents the best knowledge of the setup that is available to the estimator and controller. The compact model includes aberration maps from the lab setup which can be measured and accounted for. For this reason, the full model is used only in simulations rather than actual testbed operations. Lastly, the Jacobian model is used only in the wavefront control experiments for computing the control Jacobian matrices. It provides the linearized response of each deformable mirror (DM) actuator in the final focal plane's E-field and is critical for quickly computing the best DM shape in the model-based electric field conjugation (EFC) method.

Developing a wavefront propagation pipeline

The first analysis tool developed in this thesis was a 2D wavefront propagation pipeline in FALCO, customized for scalar vortex coronagraph development. FALCO contains many built-in functionalities designed for high contrast imaging instrumentation development. These were used in this pipeline to generate some standard optical elements including the stellar point spread function (PSF), the simple circular

[1] `https://github.com/ajeldorado/falco-matlab`

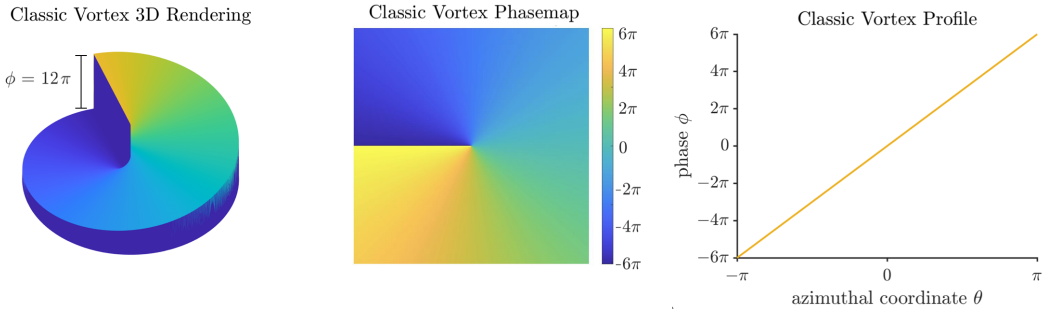

Figure 3.1: 3D rendering, phase map and azimuthal profile for the classic scalar vortex coronagraph focal plane mask. The classic vortex shown here is for charge $l = 6$.

telescope pupil and the Lyot stop pupil. The other critical optical component of a coronagraphic system is the FPM. A large part of the simulation work carried out in this thesis was dedicated to designing and modeling high resolution maps of custom scalar FPMs, and adapting FALCO's existing wavefront propagators to accurately simulate their performance.

The simplest case is the classic vortex SVC, as shown in Figure 3.1. This topography is a simple phase ramp wrapping around the optical axis, and its slope is proportional to the charge of the vortex l. The classic vortex shown here in Figure 3.1 has a topological charge of $l = 6$, so its phase is a linear ramp from -6π to $+6\pi$.

High resolution maps of this mask design and all others presented in this thesis (like the middle image of Figure 3.1) were generated as part of the pipeline developed in this work. These maps, along with the propagation methods created for testing them, have since been added to the FALCO repository and are available to the public for further research.

For the scalar vortex coronagraph pipeline built in this thesis work, two wavefront propagators were used to model the light as it passes through the coronagraph elements. FALCO already contains several methods for performing optical propagations in 2-D Cartesian coordinates which utilize discrete Fourier transforms as matrix Fourier transforms (MFTs). The first propagator in the pipeline was adapted from FALCO's high-fidelity propagator for the vortex coronagraph, which goes from the pupil plane before the vortex to the pupil plane after it. The second was one of FALCO's MFT functions which goes from the Lyot pupil plane to the final focal plane.

The traditional FALCO vortex propagator uses two MFTs to describe the FPM at high-resolution in the inner region and at low resolution for the full focal plane. The high-resolution map is used to sample the vortex's singularity well enough to reduce the numerical noise floor arising from the fast Fourier transform (FFT). The high and low resolution maps of the mask are then combined using a smoothing Tukey window to avoid artifacts from the different resolution domains. However this implementation has limitations when considering FPMs with radial features since it was designed for only azimuthally-varying FPMs of a (pseudo) infinite-extent, like the vortex. This propagation also does not consider any chromatic dependence since the theoretical vector vortex coronagraph (VVC) behaves identically across subbands in any given bandwidth.

For the pipeline developed in this thesis, this propagator was modified to instead consider two distinct scalar vortex mask maps at different resolutions. The high resolution map considers only the central region and contains radial features while the low resolution map considers an azimuthal-only pattern across the full focal plane. In addition, to consider the chromatic nature of the scalar vortex coronagraph, this propagator applies a wavelength-dependent factor which scales the phase of the FPM. The chromaticity is accounted for by recomputing both the high and low resolution FPMs for each wavelength with respect to the designed wavelength for the mask.

Modal decomposition tool

Originally for the pursuit of understanding the comparative performance of different topologies better, Ruane et al. (2019) presented an analysis approach depending only on the phase profile of a topography. In this thesis, I further developed this into a tool and used it to provide a more extensive understanding of the behavior of different SVC topographies. In Desai et al. (2022) this tool is presented for predicting the performance of any azimuthally varying SVC topography. This tool is crucial in understanding the different leakage contributions to the overall performance of different SVC topographies, and contributes to the development of new SVC designs.

Modal decomposition is a way to break down and visualize the power spectrum of an SVC. These quantities are important in order to predict the amount of stellar leakage (zeroth order mode) and the sensitivity to aberrations, as well as the dominant topological charge for any potentially complex phase profile. Since an optical

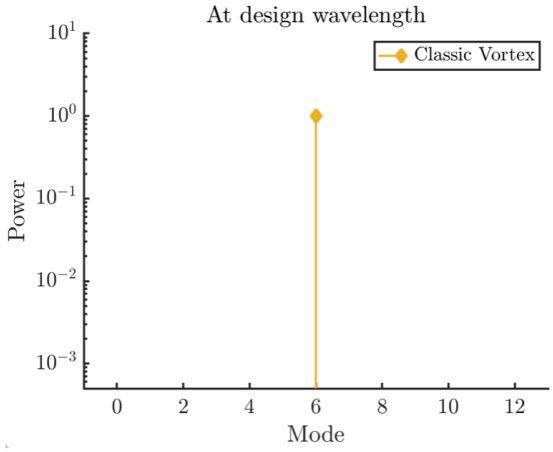

Figure 3.2: A modal decomposition for a charge 6 classic vortex coronagraph at the design wavelength. A single peak at mode 6 indicates ideal charge $l = 6$ vortex behavior.

vortex can be expressed as a Fourier series, in the exponential form each coefficient can be linearly decomposed as shown below.

Any azimuthal phase profile, including an optical vortex, can be decomposed and written as:

$$t(\theta, \lambda) = \Sigma_m C_m(\lambda) e^{im\theta} \tag{3.1}$$

with

$$C_m(\lambda) = \frac{1}{2\pi} \int_{\pi}^{-\pi} t(\theta, \lambda) e^{-im\theta} d\theta. \tag{3.2}$$

Each mode m corresponds to a charge m vortex. Every azimuthal phase profile can therefore be interpreted as a linear combination of vortexes of different topological charge.

As an example, this technique is applied to the classic vortex shown in Figure 3.1. At the design central wavelength, only the expected mode 6, is found (as shown in Figure 3.2). However, when a modal decomposition is performed at a wavelength offset from the central wavelength, the chromatic behavior of the SVC is revealed. Figure 3.3 shows the power spectrum of a SVC at a 5% wavelength offset and 10% offset. Mode six is still the primary peak, however, other peaks emerge.

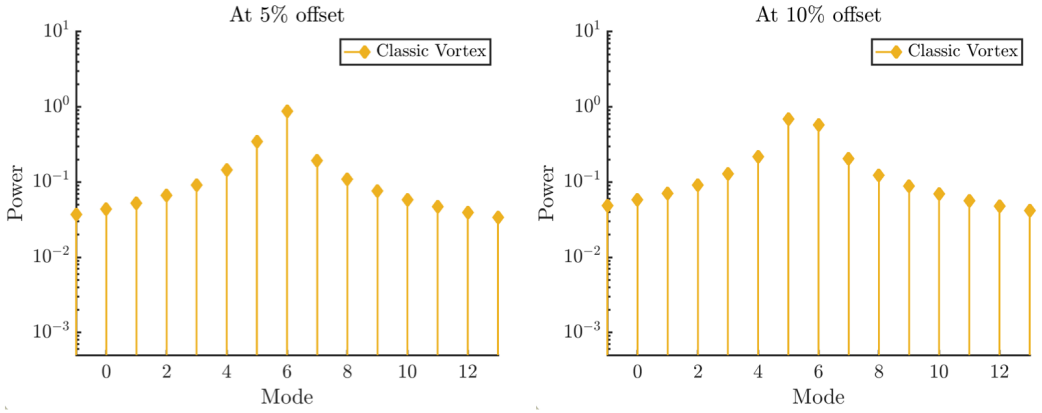

Figure 3.3: A modal decomposition for a charge 6 classic vortex coronagraph at wavelengths 5% and 10% offset from the designed wavelength. Several new peaks emerge at undesirable odd and low even modes.

Specifically, a peak emerges at mode zero which corresponds to zeroth order leakage. Zeroth order leakage corresponds to starlight passing straight through the coronagraph without being affected by the vortex at all and therefore not being suppressed and resulting in a scaled down version of the PSF.

Furthermore, the peaks at even modes correspond to energy distributed to evenly charged vortex behaviors, whose behaviors are well studied. Therefore, for these modes, starlight is effectively nulled. Odd modes, on the other hand, correspond to odd charged vortexes, where starlight suppression is deficient since only an even charge produces a null for a vortex coronagraph (Swartzlander, 2005; Mawet et al., 2005a; Foo et al., 2005; Lee et al., 2006).

The peaks corresponding to low even charge vortexes are important because these vortexes are known to be affected more negatively in the presence of low order aberrations (as explained in Section 2.4) (Ruane et al., 2018). Peaks at even modes larger than the desired charge are not expected to be as problematic since higher charge vortexes are not highly sensitivite to aberrations, although they do affect the throughput and inner working angle.

3.5 Experimental methods

Mask metrology

After simulating scalar phase mask designs, the next step is to fabricate them and experimentally test them. Before measuring the high contrast performance

of a coronagraph mask prototype, first it needs to be characterized. The primary assessments of fabrication quality relevant to coronagraph phase masks are 1) the size of the central defect and 2) the phase response of the mask.

Since a vortex phase mask has a singularity at the center, fabrication is the most delicate at the very center. Microscope images of the mask prototypes provided measurements of the central defect. The microscope setup was also used to assess the fabrication quality of some other optical elements including several Lyot stop pupils and field stop masks.

A Zygo interferometer setup was built and used to characterize the phase response of several prototype scalar vortex masks. This metrology technique for characterizing surface shape and transmission quality of test optics is based on the principles of the Fizeau interferometer. The Fizeau interferometer is the most commonly used interferometer for testing optical components and systems for space-related instrumentation (Liu et al., 2005). In a Fizeau laser interferometer, a beamsplitter divides the beam from a laser source. The "reference beam" is directed to a high-quality flat mirror. The "test beam" is directed through the optic to be tested and then to a high-quality flat mirror.

When the two reflected beams pass back through the beamsplitter, they recombine at the detector and form an interference pattern. This pattern is due to changes in phase caused by the optic being tested which the reference beam did not experience. The detector records this interference pattern as a single measurement frame. Then by combining several frames, the change in wavefront caused by the beam passing through the optic can be quantified. In this case, the heights of all the points on the scalar phase mask can be measured. To acquire multiple frames, the Zygo interferometer in this setup uses dynamic acquisition. That means the Zygo measures several extremely short exposure data frames and then averages the best ones to produce measurements despite vibration or turbulence.

Figure 3.4 shows the experimental setup for the Zygo imaging. A Zygo Verifire class IIIa laser with a 6 inch beam was used to measure the phase ramps of the masks. The built-in camera resolution was 1200×1200 pixels and the maximum optical zoom factor achieved was 5×. In order to achieve a sufficient number of pixels to image the smallest SVC (2 mm in diameter), a telescope was implemented to shrink the Zygo beam diameter and recollimate the light.

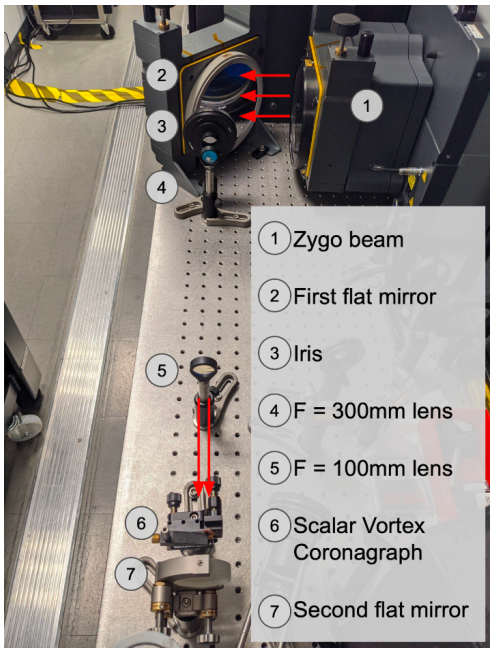

Figure 3.4: Layout of the Zygo interferometer setup built for phase metrology of scalar vortex phase mask prototypes.

The Zygo beam was passed through two 1" lenses: a $F = 300$ mm lens, and then a $F = 100$ mm lens to achieve a new beam width of 1/3" which then passed through the coronagraph mask before it was reflected off a perfectly normal mirror. Two additional elements were used to achieve imaging with this smaller beam: an iris for blocking stray light not passing through the SVC, and a primary large flat mirror for deflecting the beam so the setup could fit the geometric constraints of the optical bench. Note that each of the coronagraph masks were easily switched out from the mount before the final mirror and the mount was placed as close as possible to the mirror to minimize phase loss in the Zygo imaging.

Three varieties of SVCs were manufactured and with the purpose of directly comparing their starlight suppression performance, their phases were characterized using the Zygo interferometer setup described above. The prototypes included three ultrafast laser inscripted (ULI) masks shipped from Australia, seventeen direct laser beam written Zeiss masks, and three nano-posts SVCs provided by the Caltech Kavli Institute. Figure 3.5 shows photographs from the lab of one of each of these sets of prototypes.

The three ULI masks were delivered as square regions on circular substrates and came in two different sizes: one 2 mm$\times$2 mm sample and two 4 mmx4 mm samples.

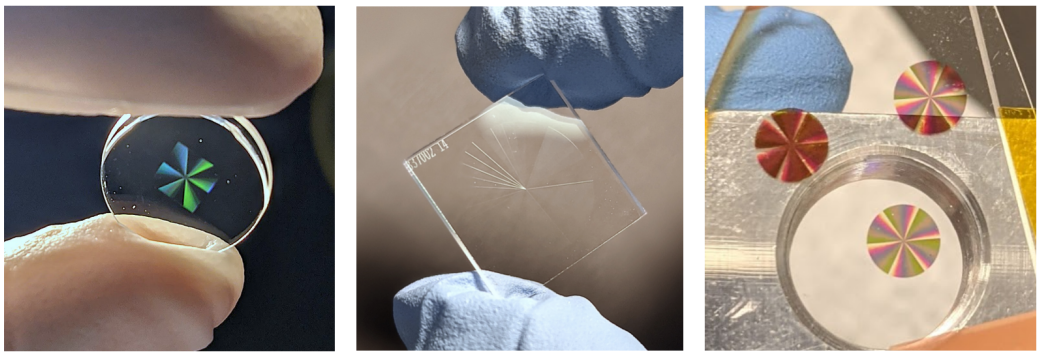

Figure 3.5: Three prototype SVC masks fabricated with different techniques (left) ultra-fast laser inscription, (middle) direct laser beam writing, (right) nano-posts.

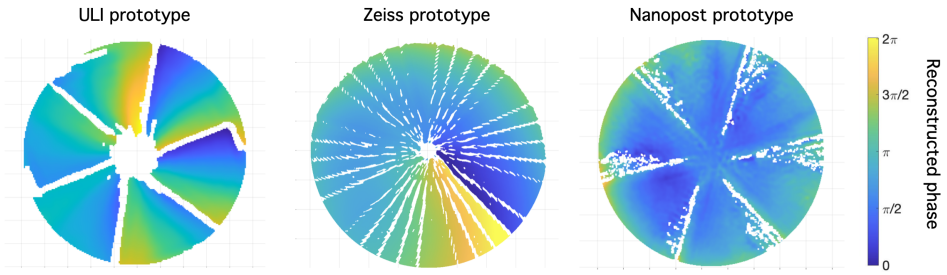

Figure 3.6: Zygo phase reconstructions for three prototype SVC masks fabricated with different techniques (left) ultra-fast laser inscription, (middle) direct laser beam writing, (right) nano-posts.

They were designed for a central wavelength of 635 nm. The Zeiss masks are stepped scalar vortex masks. They were created on fused silica and optimized for a central wavelength of 775 nm. The three nanopost masks were fabricated with electron-beam lithography on an irregularly shaped piece of glass. All the ULI, Zeiss, and nanopost masks were designed to have a charge of 6 as is clearly visible by the 6-fold symmetry in the pattern in the photograph of the samples.

The phase maps in Figure 3.6 display the results from the Zygo characterization. Analysis of these Zygo images included removing the first three Zernike modes: piston, tip and tilt. The plots here show the extrapolated phase by the Zygo for one example of each of the three SVC mask types. The ULI masks demonstrated a smooth phase reconstruction, but too large of a central defect to perform well as a coronagraphic FPM. The Zeiss prototypes were the most consistent in their Zygo

phase characterizations and showed the closest profile to the desired phase ramp. The nano-post prototypes were delaminated during the experimental procedures and therefore resulted in a poor phase ramp reconstruction. Since the Zeiss prototypes showed the best phase characterization and smallest central defects, they were further tested in high contrast testbeds for their starlight suppression ability (see Chapter 4).

High Contrast Spectroscopy Testbed

To better understand the chromatic behavior of scalar vortex mask prototypes the High Contrast Spectroscopy Testbed (HCST) in the Exoplanet Technology Laboratory (ET lab) at Caltech was used. The layout for the HCST is shown in Figure 3.7. The star was simulated using a supercontinuum white-light laser source (NKT Photonics SuperK EXTREME) followed by a tunable single-line filter (NKT Photonics SuperK VARIA) to isolate the specific wavelengths desired for testing. Wavelengths were sampled by moving the tunable filter to select narrowbands (6 nm bandwidth) between 685 nm and 820 nm at increments of 15 nm.

After the entrance pupil, the light is collimated by off-axis parabolic mirrors (OAPs) onto the DM. The adaptive optics system consists of a Boston Micromachines Corporation kilo-DM that flattens the wavefront. The DM has a continuous surface membrane with 34×34 actuators with an inter-actuator separation of 300 μm (BMC, 2024). Several more OAPs are used to create a focal plane, where the light is focused on the scalar vortex mask. Next OAPs collimate the light again to a downstream pupil plane where a circular Lyot stop with 93% of the radius of the 16.4 mm beam blocks the light diffracted by the FPM. This size of Lyot stop was chosen because it preserves the throughput. After this, a field stop is introduced at the next focal plane to help block any unwanted light outside the region of interest from reaching the camera. The remaining light is finally imaged with a f/50 beam onto the camera (Oxford Instruments Andor Neo 5.5) at focus. A filter wheel is placed before the camera, either set to a neutral density (ND) filter (Thorlabs NE20B, OD = 2.0) or an empty slot for photometric calibration.

A custom mount was designed to hold both a scalar vortex mask and a vector vortex mask to allow for switching between and comparing the two flavors. Figure 3.8 shows the installation of the custom mount and scalar vortex mask prototype into HCST. A more detailed description of the HCST testbed and the optical components designed and incorporated can be found in Bertrou-Cantou et al. (2023), Llop-Sayson et al. (2020a), and Llop-Sayson et al. (2020b).

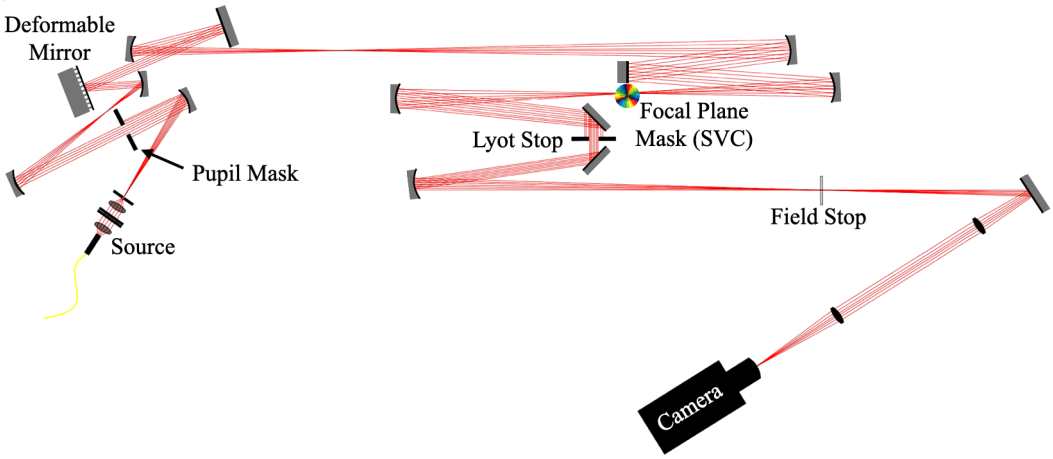

Figure 3.7: Layout of the High Contrast Spectroscopy Testbed (HCST) at Caltech used for demonstrating the scalar vortex coronagraph.

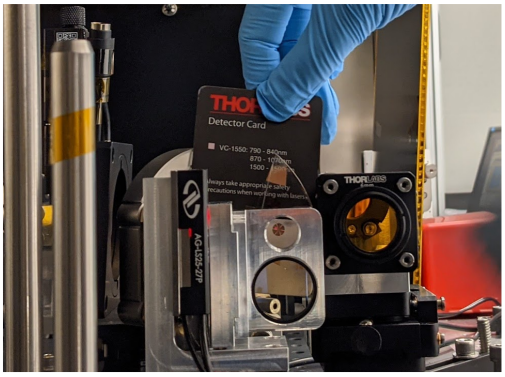

Figure 3.8: Custom focal plane mask mount designed to hold both a scalar (SVC) and vector (VVC) vortex coronagraph mask on the High Contrast Spectroscopy Testbed at Caltech. The SVC is mounted in the top slot and the VVC is in the bottom slot and the same mount design was eventually used for the In-Air Coronagraph Testbed at JPL.

In-Air Coronagraph Testbed

In addition to doing initial chromatic characterization on HCST at Caltech, a second testbed, the In-Air Coronagraph Testbed (IACT) at JPL was used for extensive wavefront sensing and control experiments with the scalar vortex masks. IACT was used to demonstrate the first laboratory comparison of vector versus scalar vortex coronagraphs with traditional dark hole digging techniques (see Chapter 4)

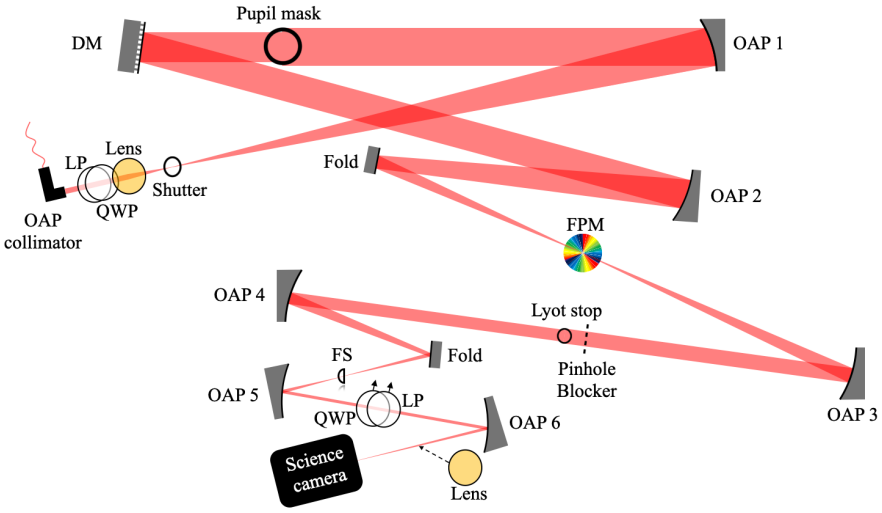

Figure 3.9: Layout of the In-Air Coronagraph Testbed (IACT) at JPL used for performing wavefront sensing and control experiments.

and further to compare model-based and model-free wavefront sensing and control techniques (see Chapter 5).

The layout for IACT is shown in Figure 3.9. For the work performed in this thesis, the laser source on IACT was replaced with an NKT supercontinuum laser enabling broadband testing. Similarly to HCST, several OAPs are employed here for collimating and focusing the beam which encounters an entrance pupil mask, DM, focal plane vortex phase mask, Lyot stop, field stop, and camera. The primary differences between the two in-air testbeds, IACT and HCST, is that IACT has a bigger DM and a larger F number (F/# $\approx$ 82.5 compared to F/# $\approx$ 30) at the FPM plane. The DM on IACT is a 2040 actuator (2k) micro-electro-mechanical systems (MEMS) DM manufactured by Boston Micromachines Corporation (BMC, 2024). Additionally, to test both the SVC and VVC masks, the quarter wave-plate and linear polarizer downstream of the coronagraph in Figure 3.9 are used with the VVC and moved out of the beam for the SVC experiments. Further details about the IACT design and optical setup can be found in Baxter et al. (2021).

3.6 Evaluating performance

Both the 2D coronagraph wavefront pipeline developed in this thesis and the experimental measurements conducted in the laboratory aim to provide a platform for

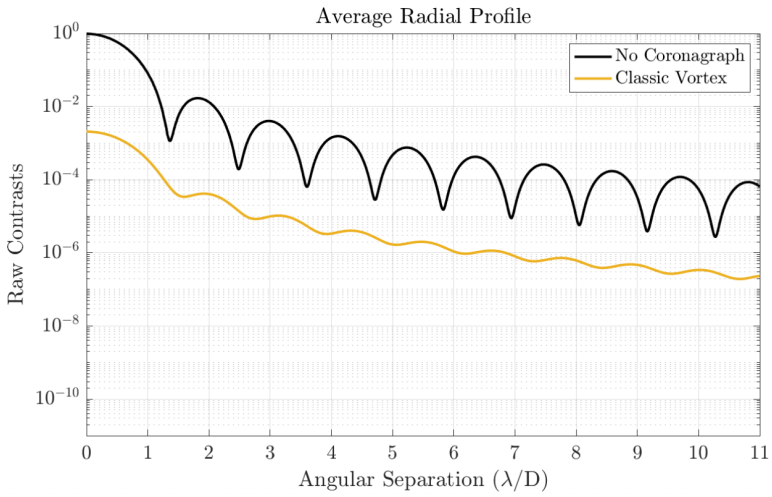

Figure 3.10: Contrast profile for the classic vortex coronagraph demonstrating the simulated starlight suppression performance in broadband light. The un-occulted point spread function (black) displays characteristic diffraction rings while the coronagraphic image (yellow) shows how the classic vortex suppresses this pattern.

comparing the performance of several scalar phase mask topographies in broadband light. In either simulation or lab experiments, the final coronagraphic images at several wavelengths are needed to produce two primary performance metrics: 1) a measure of the starlight suppression as a function of angular separation, referred to as a 'contrast profile' and 2) a measure of the average contrast in the final image as a function of wavelength, referred to as a 'chromaticity V-curve' due to its shape.

The first measurement of a coronagraph's starlight suppression ability is called the raw contrast. Raw contrast is defined as the averaged intensity of the simulated coronagraphic image at the final focal plane divided by the peak intensity of the unocculted PSF image (or the final focal plane image without any coronagraph). Using the wavefront propagation pipeline described in Section 3.4, the coronagraphic ability of the charge 6 classic vortex shown in Figure 3.1 could be simulated. Figure 3.10 shows the average radial profiles of the final focal plane image with and without a classic vortex coronagraph.

The second measurement of a coronagraph's performance evaluates its ability to suppress starlight across a large bandwidth. For a charge 6 vortex coronagraph, the inner working angle is at 2.4 λ/D so the typical measurement relevant for planet detection is the average contrast across the region from 3 - 10 λ/D. Plots like the one in Figure 3.11 show the average contrast in that region as a function of the phase

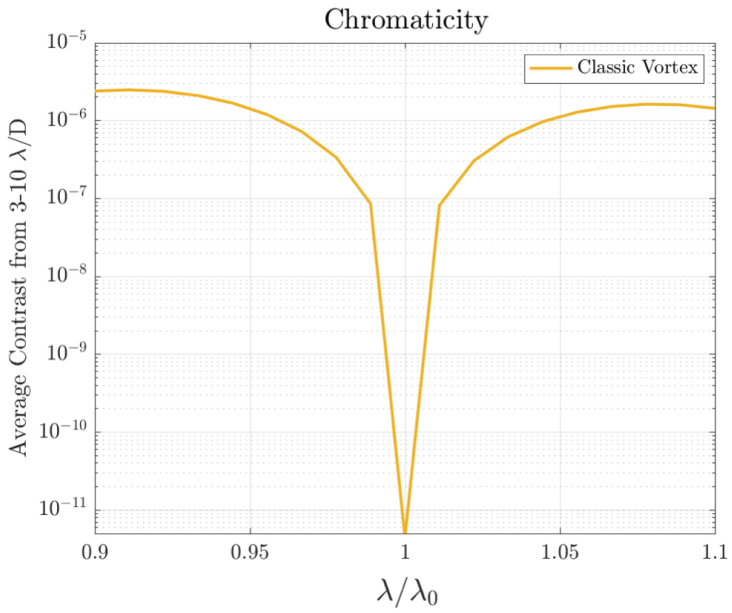

Figure 3.11: Chromaticity V-curve for the classic vortex coronagraph shows average contrast from 3 - 10 λ/D as a function of the phase scale factor, or wavelength offset, and demonstrates the simulated starlight suppression performance in broadband light. The V-shape shows how the scalar vortex performance degrades drastically away from the central wavelength λ_0.

scale factor. The phase scale factor is λ/λ_0, or the ratio of a given wavelength λ in the bandwidth, to the design wavelength, λ_0. Since the classic vortex is very chromatic, the V-curve shows the best contrast at the design wavelength ($\lambda/\lambda_0 = 1$) and significantly reduced contrasts at offset wavelengths.

In simulation further analyses were carried out with other FALCO functionalities. This included simulating the coronagraph's throughput and sensitivities to low order wavefront aberrations. The planet throughput was computed by simulating a point source across different off-axis angular separations (between 0-5 λ/D) and measuring the total flux allowed through the coronagraph to the final image plane. This was primarily used to verify that the inner working angle of new SVC topographies was not affected.

The aberration sensitivities were simulated with FALCO by inputting between 1-10^{-6} waves RMS wavefront error at the entrance pupil in the forms of tip-tilt, defocus, astigmatistm, coma, trefoil, and spherical aberrations. The stellar leakage is then averaged and normalized to the peak leakage without a coronagraphic mask for both

narrowband and broadband light. Further details and example of this analysis can be found in Section 6.5.

After assessing the relative chromatic performance for a promising mask design, the next step is to add wavefront control and perform dark hole digging with EFC. Dark hole digging experiments with the algorithms described in Section 2.5 were performed both in simulation (with PWP + EFC in FALCO) and in experiment (on IACT with 3 different EFC methods).

Chapter 4

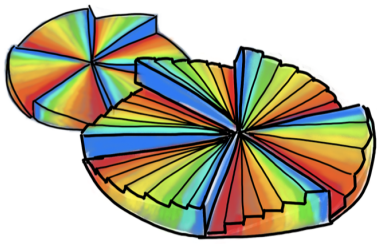

FIRST GENERATION SCALAR VORTEX CORONAGRAPHS

Article: Laboratory demonstration of the wrapped staircase scalar vortex coronagraph

Desai, N., G. Ruane, J. D. Llop-Sayson, A. Bertrou-Cantou, A. Potier, A. E. Riggs, et al. (Apr. 2023). "Laboratory demonstration of the wrapped staircase scalar vortex coronagraph". In: *Journal of Astronomical Telescopes, Instruments, and Systems* 9.2, p. 025001. DOI: 10.1117/1.JATIS.9.2.025001.

This chapter is also based on work published in the following proceedings:

Desai, N., J. Llop-Sayson, N. Jovanovic, G. Ruane, E. Serabyn, S. Martin, and D. Mawet (Sept. 2021). "High contrast demonstrations of novel scalar vortex coronagraph designs at the high contrast spectroscopy testbed". In: *Techniques and Instrumentation for Detection of Exoplanets X*. Ed. by S. B. Shaklan and G. J. Ruane. SPIE. DOI: 10.1117/12.2603953.

Desai, N., J. Llop-Sayson, A. Bertrou-Cantou, G. Ruane, A. E. Riggs, E. Serabyn, and D. Mawet (Aug. 2022). "Topological designs for scalar vortex coronagraphs". In: *Space Telescopes and Instrumentation 2022: Optical, Infrared, and Millimeter Wave*. Ed. by L. E. Coyle, S. Matsuura, and M. D. Perrin. Vol. 12180. International Society for Optics and Photonics. SPIE, 121805H. DOI: 10.1117/12.2630950.

4.1 Motivation

The main goal of this chapter is to explore broadband scalar vortex phase masks in simulation and early prototype performance experimentally. Scalar vortex coronagraph (SVC) masks have received much less attention than vector vortex coronagraph (VVC) masks, even though scalar vortex masks are polarization-insensitive and can theoretically provide significantly higher throughput with simpler optics. However they are limited by their chromatic behavior.

This work builds directly upon early literature by Swartzlander (2006) and more recent literature by Ruane et al. (2019) which both propose the theoretical and simulated potential that scalar vortex coronagraphs offer for advancing high contrast imaging of exoplanets. A few strategies have been proposed to achromatize SVCs including combining two optics of different refractive indices into a dual-layer focal plane mask (FPM) (Swartzlander, 2006), or cleverly wrapping the profile of the phase ramp (Galicher et al., 2020). Wrapping the phase of a vortex, as introduced by Galicher et al. (2020), essentially means introducing phase jumps of 2π to allow for a continuous vortex phase ramp with the same charge but spanning a smaller overall phase range. Any other non-2π phase jumps might lead to off-axis point spread function (PSF) distortions or attenuations. Here I focused on comparing methods of varying the FPM surface topography to improve broadband performance and the focus of this chapter is the proof-of-concept testing of a prototype monochromatic SVC.

In order to fully understand the effect that the topography of an SVC has on its coronagraphic performance and to effectively choose one design to fabricate for lab testing, a trade study of several designs in simulation as well as Fourier decomposition analyses was performed. In this chapter, I present a comparison of simulated designs and the first laboratory demonstration of the the wrapped staircase scalar vortex mask. The experimental results include characterization of the mask's light suppression capability and chromatic behavior with and without wavefront sensing and control. The wrapped staircase mask presented here incorporates discrete steps along the vortex phase ramp similar to the charge 2 staircase mask in Lee et al. (2006). However, that staircase design did not implement phase wrapping. Here the charge 6 staircase phase ramp is wrapped six times in the design proposed by Ruane et al. (2019). One of the primary motivations here is to study how this impacts the broadband performance.

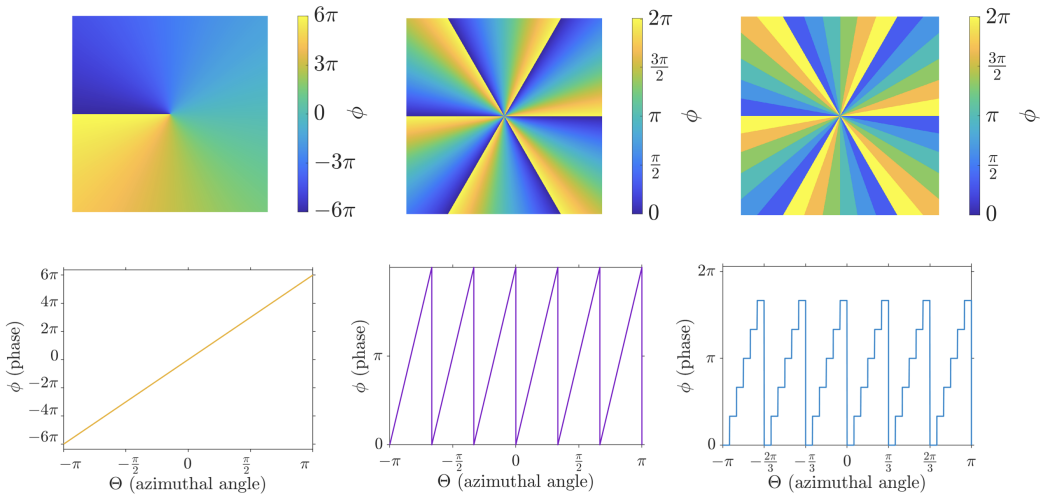

Figure 4.1: Phase mappings (top row) and corresponding phase profiles (bottom row) for three charge 6 scalar vortex FPM topographies (from left to right): classical vortex, sawtooth vortex, wrapped staircase vortex. The wrapped staircase vortex (right) was originally proposed in Ruane et al. (2019).

4.2 Simulations of mask topographies

Several different SVC topographies of charge 6 were simulated to perform a direct comparison of their performance. Figure 4.1 shows the phase mappings and the corresponding azimuthal profiles for a charge 6 classical vortex, sawtooth vortex, wrapped staircase vortex. The focus of this paper is to provide an analysis of the chromatic behavior for the wrapped staircase scalar vortex phase mask and a comparison of its performance against a vector vortex phase mask. However, additional work in Desai et al. (2022) considers the simulated performance of an additional charge 6 variation of the phase wrapping design derived from Galicher et al. (2020) (see the supplemental work in Section 4.7).

Here three vortex topographies are considered:

Classical Vortex: A classical vortex FPM is a simple phase ramp wrapping around the optical axis, and its slope is proportional to the charge of the vortex. In Figure 4.1, the left image is a charge 6 classical vortex, so its phase is a linear ramp from 0 to 12π, or shown here as -6π to $+6\pi$.

Sawtooth Vortex: In the sawtooth vortex design, the charge of the vortex dictates the number of phase ramps, and therefore the slope. It is referred to as the 'sawtooth'

vortex SVC because the azimuthal profile of this mask looks like a sawtooth pattern. In the middle image of Figure 4.1, the charge 6 sawtooth vortex has 6 ramps, each of which starts at a phase of 0 and goes to 2π.

Wrapped Staircase Vortex: The wrapped staircase vortex design from Ruane et al. (2019), whose name is apparent from its phase profile shown in the right image of Figure 4.1, is a discretizated version of the sawtooth vortex. Instead of several continuous linear phase ramps, this design allows for several sectors with flat steps at heights ranging from 0 to 2π within each sector. Starting the first step at $\phi = 0$, the staircase does not actually reach 2π, because of the digitization of the ramp. For example, Figure 4.1 shows a charge 6 wrapped staircase vortex with 6 sectors and 6 steps in each sector.

Wavefront propagation simulations

The Fast Linearized Coronagraphic Optimizer (FALCO)[1] simulation without wavefront control found that on average the wrapped staircase mask attenuates starlight by a factor of approximately a few times 10^{-7} across a 10% bandwidth and approximately a few times 10^{-6} across a 20% bandwidth. The simulated performance of the classical vortex across a 20% bandwidth without wavefront control is a few times 10^{-6}.

To simulate wavefront control, electric field conjugation (EFC) (explained in Chapter 2) is performed in FALCO to iteratively find an optimal deformable mirror shape that suppresses residual starlight from 3-10 λ/D. After 50 iterations of EFC across a 10% bandwidth, the classical vortex yielded an average contrast of 1.16×10^{-6} whereas the wrapped staircase vortex yielded an average contrast of 3.92×10^{-7}.

Modal decompositions of phase profiles

The technique of modal decomposition introduced in Section 3.4 was applied to the SVC topographies to compare their predicted performances. As shown in Figure 4.2 (left), at the design central wavelength, only the expected mode, six, is found and there is consistent behavior across all three FPM topographies. However, when a modal decomposition is performed at a wavelength offset from the design central wavelength, the chromatic behavior of each SVC is revealed. In Figure 4.2 at a 1% offset (middle), and a 10% offset (right), mode six is still the primary peak, however, a peak emerges at mode zero which corresponds to the zeroth order leakage, which

[1] `https://github.com/ajeldorado/falco-matlab`

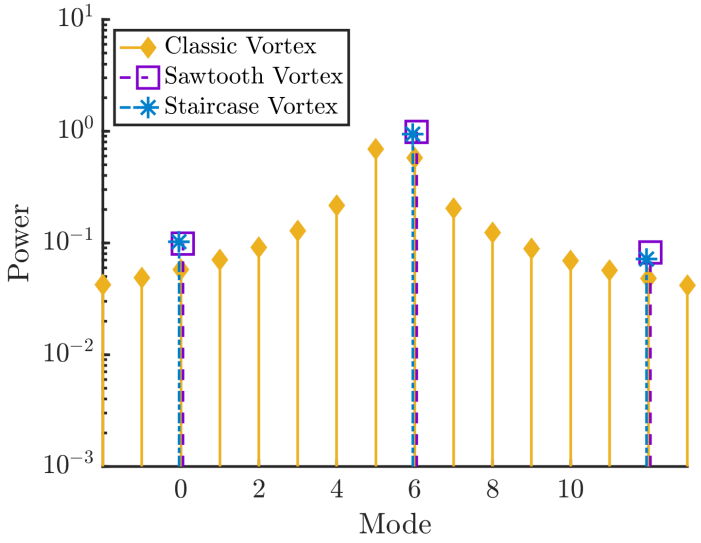

Figure 4.2: A modal decomposition at a 10% wavelength offset (right) shows how each of the classical vortex (yellow), sawtooth vortex (purple), and wrapped staircase vortex (blue) topographies differ in behavior for broadband light.

corresponds to starlight passing through the coronagraph unaffected, as explained in Chapter 3.

An intuitive explanation of the sawtooth design's modal decomposition can be derived from the known modes of a sawtooth wave in signal Fourier analysis. Typically, the first mode is at some f_0 and all the other modes are at higher frequencies which are multiples of f_0 harmonics. For a classical SVC (single phase ramp), the first frequency is at the topological charge of 1, then the second one is at 2, and so on, explaining the low-order modes in the decomposition for the classical vortex. For a sawtooth design, the first non-zero frequency is $f_0 = 6$, then the next is $f_0 = 12$, and so on, matching the results for the sawtooth vortex modal decomposition.

The peaks at even modes correspond to energy distributed to other vortexes with even charge. Therefore, for these modes, starlight is effectively nulled and their behavior in the presence of low order wavefront aberrations is well studied (Ruane et al., 2018). Odd modes, on the other hand, correspond to odd charged vortexes, where starlight suppression is deficient since only an even charge produces a null for a vortex coronagraph. This explains why the classical vortex, which displays odd modes in the modal decomposition (orange), exhibits the worst contrast performance in FALCO simulations (see Section 4.7 for further details).

Figure 4.2 suggests that the wrapped staircase and sawtooth topographies outperform the classical vortex, particularly because no other odd or small even modes besides the zeroth order leakage appear in the broadband modal decomposition analysis. Since the modal decompositions for the wrapped staircase and sawtooth vortex topographies are comparable, and based on their simulated starlight suppression shown by their V-curves (see Section 4.7) the wrapped staircase design was chosen to be made for its manufacturability.

4.3 Wrapped staircase mask design and fabrication

The scalar vortex mask fabricated was a wrapped staircase scalar vortex mask manufactured by Zeiss and designed to have a charge of 6. It had six sectors made up of six steps each. The mask was fabricated on fused silica and created for a central wavelength of 775 nm. The square silica sample is 15 mm by 15 mm in size and the actual spiral phase plate region is circular with a diameter of 13 mm and centered in the square (see Figure 4.3).

As discussed in Section 3.5, an important measure of the quality of an FPM, particularly vortex masks, is the size of the central defect because light passing through it does not pick up the desired phase ramp. Microscope measurements revealed the central defect on the mask to be no larger than approximately 8.2 microns in diameter. It is imperative that the central defect be small relative to the beam/spot size. Since the focal ratios of the optical setup here are large (F/# $\approx$ 30 for High Contrast Spectroscopy Testbed (HCST) and F/# $\approx$ 80 for In-Air Coronagraph Testbed (IACT)), this measured central defect is sufficiently small at the working wavelength of 775 nm. The device has a broadband anti-reflective coating with a reflectance of less than 0.2% over 725 nm to 825 nm. Transmittance is taken into account through the normalization since the off-axis PSF image is also taken through the mask.

4.4 Chromaticity characterization

To better understand the chromatic behavior of the wrapped staircase SVC mask, the mask was installed in the focal plane of the High Contrast Spectroscopy Testbed (HCST) (introduced in Chapter 3) and its light suppression capabilities were measured at a range of wavelengths.

To quantitatively characterize the focal plane starlight suppression, the contrast curves in Figure 4.4 show the raw contrast at four wavelengths: 685 nm, 730 nm, 775 nm, and 830 nm with angular separations ranging from 3 λ/D out to 12 λ/D.

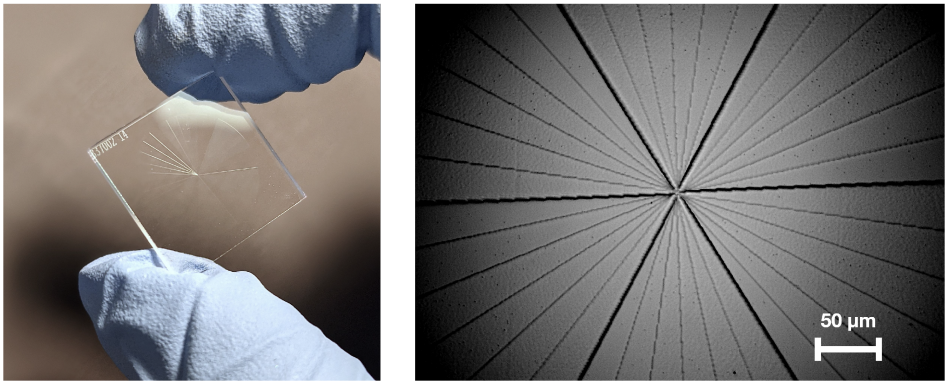

Figure 4.3: A charge 6 wrapped staircase SVC mask fabricated in fused silica (left) and a microscopic image of its central defect (right).

The raw contrast is defined as the averaged intensity of the coronagraphic image divided by the peak intensity of the unocculted PSF image. The peak intensity is defined as the highest pixel value of the non-coronagraphic image. The sampling error is negligible since the pixel sampling on HCST is approximately 6 pixels per λ/D (3×Nyquist). In each plot of Figure 4.4, the pink curve is the contrast profile without the scalar vortex mask; the distinctive bumps correspond to the Airy rings of the diffraction pattern in the PSF. The blue dashed curves are the raw contrasts with the scalar vortex mask. The overall lower contrast and the lack of bumps in the blue dashed curve shows the SVC's ability to suppress the on-axis source. Of these four profiles, it is also clear that the largest contrast improvement is with the 775 nm light, which was the design central wavelength for these scalar vortex masks.

By sampling over a large range of wavelengths and taking narrowband measurements at each, the light suppression capability of the SVC was found to degrade as the incoming starlight's wavelength deviates from the design wavelength (775 nm), as seen in Figure 4.5. Furthermore, from this graph, it can be seen that observing light across approximately a 10% bandwidth (the curve at 760 nm and the curve at 790 nm) degrades the contrast by a factor of 2 or 3.

The image plane contrast curve as a function of wavelength in Figure 4.6 shows the general chromatic behavior of the SVC, with peak performance close to 775 nm, the design central wavelength for this mask. The region of 6 - 8 λ/D is considered instead of 3 - 10 λ/D for a comparison with the theoretical chromaticity fit in the focal

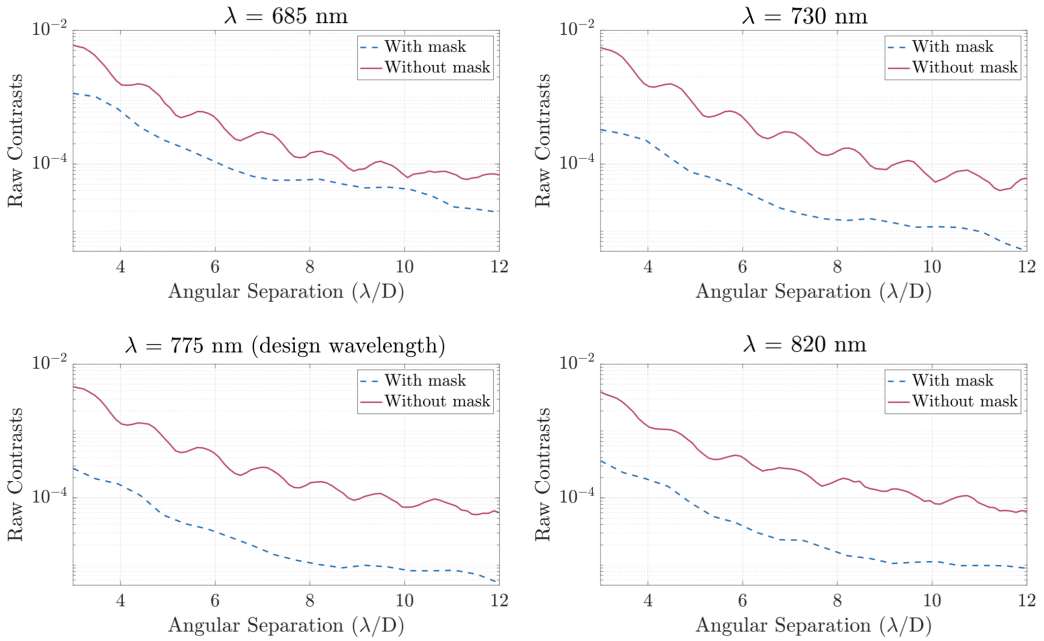

Figure 4.4: Experimentally measured unocculted point spread function (PSF) (solid pink) and coronagraphic (dashed blue) contrast curves from focal plane images for 685 nm, 720 nm, 775 nm, and 820 nm, and angular separations from 3 to 12 λ/D on HCST. Overall, the wrapped staircase scalar vortex coronagraph improved the raw contrasts and suppressed the Airy ring diffraction pattern shown by the bumps in the pink PSF curves.

plane because this region farther from the center is not as dominated by low-order wavefront aberrations and would be a reasonable metric for how much the starlight suppression performance changes as a function of wavelength. The pupil plane contrast plot in Figure 4.6 demonstrates in blue the ratio of the total flux inside the pupil versus outside the pupil. In dashed pink the parabolic fit of this curve describes a second order dependence on wavelength, as expected from theory (Ruane et al., 2019). The pupil plane data is expected to be more trustworthy because it integrates across all spatial frequencies and is less limited by the speckle patterns in the focal plane. These experimental results also compare to the simulated FALCO results without wavefront control for monochromatic light at the design wavelength, and at a 10% offset.

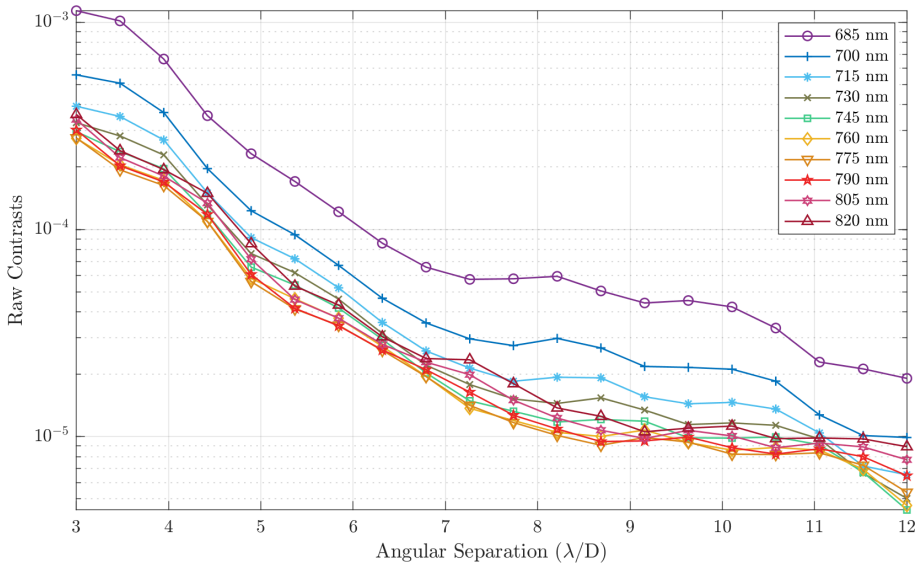

Figure 4.5: Experimentally measured classical contrast curves for wrapped staircase SVC plotting raw contrast versus angular separation for wavelengths from 685 nm to 820 nm. These were measured on HCST and calculated by taking the ratio of the azimuthal averages at each angular separation to the peak intensity of the unocculted point spread function. The best performance is observed at 775 nm, which was the central design wavelength for this scalar vortex mask.

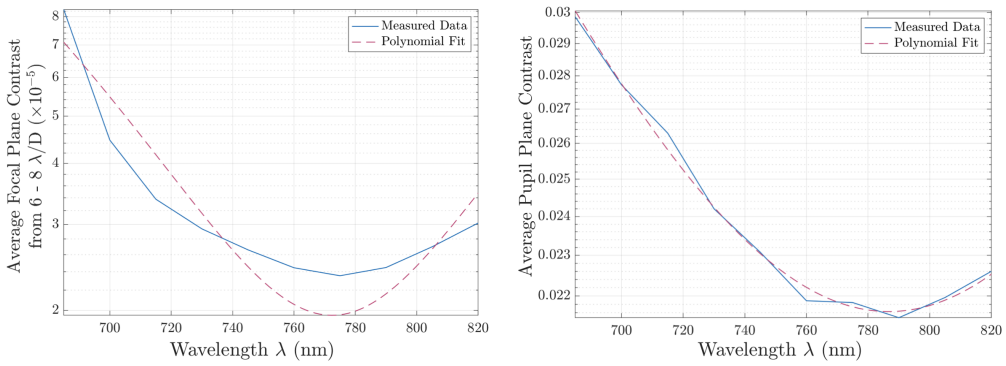

Figure 4.6: Chromaticity fits of the wrapped staircase SVC. (left) A focal plane raw contrast versus wavelength plot (solid blue) averaged across the region from 6 to 8 λ/D and a quadratic fit (dashed pink) to that data. (right) A pupil plane raw contrast versus wavelength plot (solid blue), which takes the ratio of the flux inside the pupil to the flux outside the pupil, and quadratic fit (dashed pink).

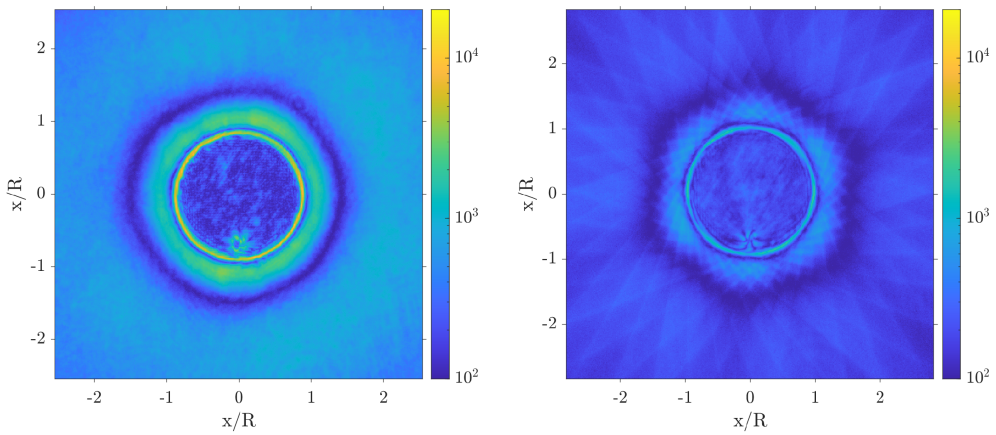

Figure 4.7: Pupil plane images without the Lyot stop on IACT taken after 0.001 seconds of integration time across a 10% bandwidth. The ring of fire can be seen for both (left) the vector vortex coronagraph (VVC) and (right) the scalar vortex coronagraph (SVC). Both pupils show a defect in the bottom due to a dead actuator in the deformable mirror. The right pupil image shows the SVC is letting a lot more light through the Lyot stop opening than the VVC.

4.5 Wavefront sensing and control results

After characterizing the broadband performance of the wrapped staircase scalar vortex mask on HCST, wavefront sensing and control was performed on IACT (introduced in Chapter 3) to further assess the contrast performance of the coronagraph.

Figure 4.7 shows the pupil plane images taken on IACT with the Lyot stop removed for both a charge 6 VVC manufactured by Beam Co. and the SVC previously characterized on HCST. From the images, the distinct "ring of fire" visible along the edges of the pupil plane can be seen, which helps to clearly demonstrate how well the FPM is suppressing starlight inside the Lyot stop aperture. The defect visible in both the VVC and SVC pupil plane in the bottom of the pupil comes from a dead actuator in the deformable mirror. The light at the edge of the pupil is a direct indication that the scalar vortex mask is successfully rejecting light.

Measurements on IACT were done for both monochromatic light and broadband light with EFC. Figure 4.8 shows the resulting focal plane dark holes after 50 iterations of EFC for the SVC and VVC in 10% broadband light side by side for a direct comparison. For the SVC, the dark hole is a semicircle digging region from 3 to 15 λ/D. For the VVC, the digging region is a semicircle from 3 to 20 λ/D since

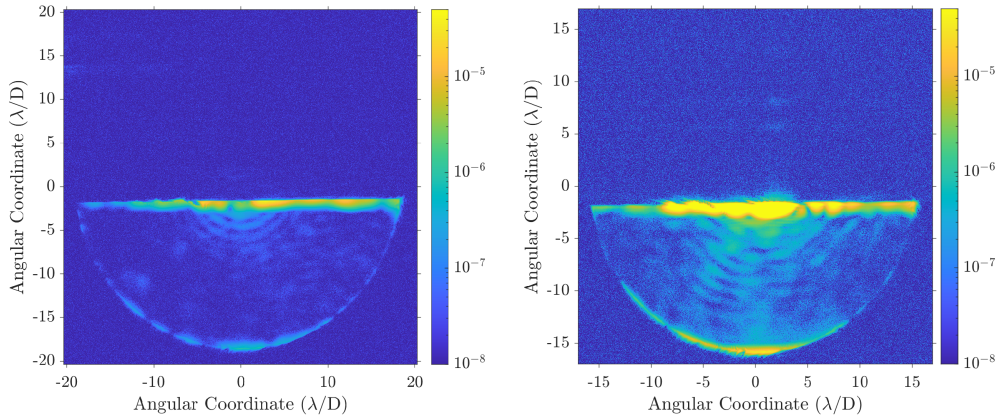

Figure 4.8: The resulting dark holes for the (left) vector vortex coronagraph (VVC) and (right) scalar vortex coronagraph (SVC) after performing electric field conjugation on IACT. Both are semicircle dark holes across a 10% bandwidth. The digging region for the SVC is up to 15 λ/D and for the VVC it is up to 20 λ/D. Across the same scoring region of 3-10 λ/D, the average contrast is 3.2×10^{-8} for the VVC's dark hole and 2.2×10^{-7} for the SVC's dark hole.

it was measured at a lower central wavelength of 635 nm, compared to 775 nm for the SVC. In monochromatic and broadband, for both the SVC and VVC the scoring region, or the area over which the average contrast is measured, is from 3-10 λ/D.

In monochromatic light for the SVC, the average contrast across the scoring region was 3.2×10^{-8}. For the VVC in monochromatic light the average contrast in the same scoring region was 1.2×10^{-8}. In broadband, the average contrast across the scoring region for the SVC was 2.2×10^{-7} taken over a 10% bandwidth. Across the same 10% bandwidth, the average contrast in the scoring region for the VVC was 3.2×10^{-8}.

The wrapped staircase vortex experimental results agree with the expected simulated values from FALCO with wavefront control in Section 4.2 within an order of magnitude. These results can be compared to those reported by Galicher et al. (2020) for a wrapped charge 8 vortex phase mask, which is discussed in further detail in the supplemental Section 4.7. Numerical simulations of the wrapped vortex phase mask predict similar performance with a 3σ detection limit at 3.1×10^{-8} for a dark hole from 6 - 13 λ/D for narrowband light at a 10% wavelength offset. The differences are related not just to the focal plane mask design, but also the different

scoring regions, which correspond to the different inner working angle of each of these masks.

These preliminary EFC tests have shown that wrapped staircase SVCs have promise for broadband starlight suppression. The two primary reasons the SVC performs worse than the VVC are chromatic leakage and model mismatch with EFC. Even though a model of the wrapped staircase SVC can be generated, EFC is sensitive to any mismatch, including clocking angle, transmission uniformity, and phase steps manufacturing accuracy.

Instead of using a perfect vortex phase mask model for EFC, a more accurate model describing the steps and sectors of the wrapped staircase mask in the EFC algorithm might result in improved contrast levels and perhaps a faster convergence rate. Alternatively, a model-free wavefront control algorithm, like iEFC (Haffert, 2022), might prove to be a more optimal approach for the wrapped staircase mask and other SVC topographies with sharp features. This is explicitly explored in Chapter 5.

4.6 Conclusion and future directions

This work demonstrated the starlight suppression capabilities of a charge 6 wrapped staircase scalar vortex coronagraph in lab. Average contrasts of 3.2×10^{-8} were achieved from 3 to 10 λ/D in monochromatic light with room for improvement by better matching the EFC model to the physical FPM. Preliminary wavefront control with EFC yielded average contrasts of 2.2×10^{-7} from 3 to 10 λ/D for light across a 10% bandwidth. One of the drawbacks to the wrapped staircase mask design which was encountered was the non-uniform transmission in the event that the star or planet lands on a non-2π transition region between steps for an off-axis measurement.

Although the contrasts achieved by the wrapped staircase SVC experimentally are not yet at the required level for space missions seeking exo-Earths around Sun-like stars, they are suitable for ground-based Earth-like planets around M type stars such as with the Extremely Large Telescope (ELT) (Fitzgerald et al., 2022; Males et al., 2022; Kasper et al., 2021). This study presents experimental evidence that wrapped staircase scalar vortex coronagraphs have further potential for narrowband starlight suppression, show promise in broadband light from lab results on HCST and IACT, and are a worthy avenue of further research for high contrast exoplanet imaging. These results motivate testing a wrapped staircase scalar vortex phase mask with alternative wavefront sensing and control algorithms – particularly model-free methods (see Chapter 5). This research also yielded an improved understanding

of the modal decomposition representation of a phase mask which can be used to reverse-engineer a new mask design. This can be done by selecting certain peaks to suppress: for instance the zeroth mode, odd modes, or small even modes, and then mitigating their modal intensity. Then an inverse Fourier transform is applied on this distribution to result in a new phase profile. Further discussion of this technique is included in the supplemental work in Section 4.7.

A wide range of designs will be considered in the future including superpositions of vortices of different orders, sinusoidal azimuthal profiles, metasurface designs with nanoposts, as well as masks that include both radial and azimuthal variations. New designs will first be simulated in FALCO and then experimentally tested in lab on IACT or HCST. Further development of coronagraph design and analyses tools is required to produce phase profiles that are unequivocally more optimal than the phase ramps presented here. Furthermore, manufacturing constraints and alignment tolerances, have yet to be accounted for in the design optimization process. Moving forward for new designs, masks with smooth ramps instead of staircase patterns will be considered for fabrication and various fabrication methods other than electron-beam lithography will be investigated to achieve these scalar vortex topographies, including ultrafast laser inscription. Through further iterative design, simulation, fabrication and testing, a better understanding of the capabilities and limitations of SVCs can be developed and ultimately their potential for direct exoplanet imaging can be investigated.

Supplemental Work

4.7 Variations of phase wrapped scalar vortex coronagraphs

Wrapped vortex designs

Galicher et al. (2020) demonstrated that one cleverly wrapped phase function resulted in good broadband performance. To investigate how phase wrapping a scalar vortex mask's topography affects its performance, and specifically its chromaticity, a direct comparison of several different topographies was performed and the findings are presented here.

The phase mapping and phase profile of the charge 8 'Galicher Vortex' in Figure 4.9 show the unique phase wrapping from Galicher et al. (2020). Requirements were

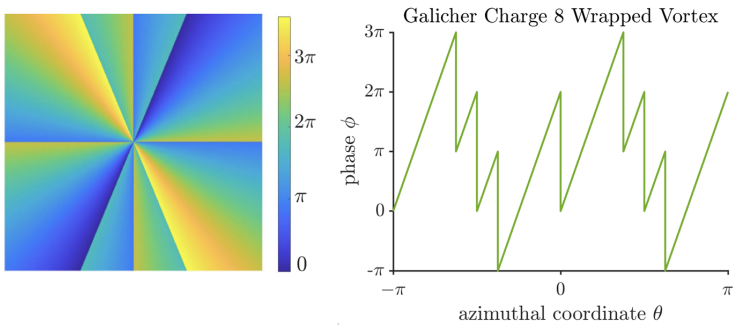

Figure 4.9: Phase mapping (left) and azimuthal phase profile (right) for the charge 8 wrapped vortex FPM proposed by Galicher et al. (2020). The same wrapping technique was applied to create the charge 6 wrapped vortex in Figure 4.10.

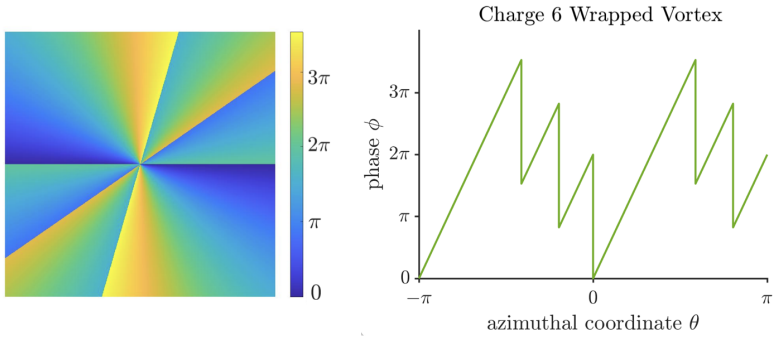

Figure 4.10: Phase mapping (left) and azimuthal phase profile (right) for the charge 6 wrapped vortex focal plane mask inspired by Galicher et al. (2020) shown in Figure 4.9.

placed on phase discontinuities to be jumps in multiples of 2π and overall the resulting phase ramp had to be that of a charge 8 vortex. Because this design was reported to improve broadband performance, one of the motivations for this study was to more generally understand phase wrapping comparatively.

Several different SVC topographies of charge 6 and charge 8 were simulated to perform a direct comparison. Figure 4.9 and Figure 4.10 show the SVC topographies that employ the 'clever phase wrapping' for charge 8 and charge 6, respectively. The simulated performance of these two topographies was compared to the topographies shown earlier in Figure 4.1: a classic vortex, sawtooth vortex, and a staircase vortex, which were also simulated in charge 8 versions.

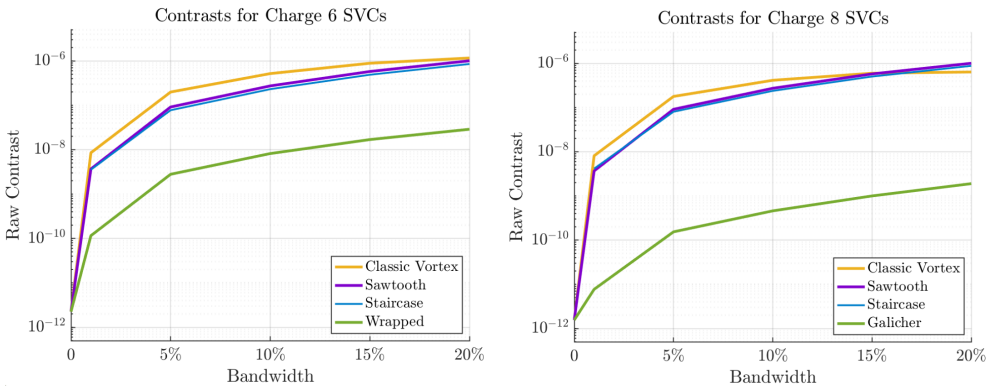

Figure 4.11: Raw contrasts for charge 6 scalar vortex coronagraphs (SVC) (left) and charge 8 SVCs (right) simulated using FALCO packages.

Wrapped Vortex: The topography considered here is inspired by the phase wrapping method proposed by Galicher et al. (2020). As mentioned in Section 4.1, that study demonstrated that cleverly wrapping the phase function resulted in improved broadband performance for a charge 8 SVC. I applied a similar wrapping principle to create a charge 6 vortex and Figure 4.10 shows the resulting design. This profile was obtained with a Markov chain Monte Carlo (MCMC) optimization of the starlight suppression, using the azimuthal position of the 2π jumps as parameters.

Wrapped vortex simulation results

The contrast curves in Figure 4.11 show the starlight suppression performance as a function of bandwidth of the four topographies of SVCs. The left figure shows a comparison between four SVC topographies for a charge 6 mask and the right shows a comparison between the same four SVC topographies for a charge 8 mask.

These contrast curves display how chromatic each topography is. For monochromatic light, all four topographies achieve raw contrasts of around 10^{-12}, likely limited by numerical noise. However as the bandwidth increases, the contrasts for the sawtooth, staircase, and classic vortex quickly deteriorate to 10^{-8} for 1% bandwidth and to around 10^{-7} for 5% bandwidth. The contrast curves of the new wrapped designs in both plots of Figure 4.11 show significantly better broadband performance than the three other topographies and the contrasts for the charge 8 wrapped mask agree with those reported in the original study (Galicher et al., 2020). These results were able to confirm that wrapping the phase ramp improves broadband performance specifically in the charge 6 wrapped mask case, shown in

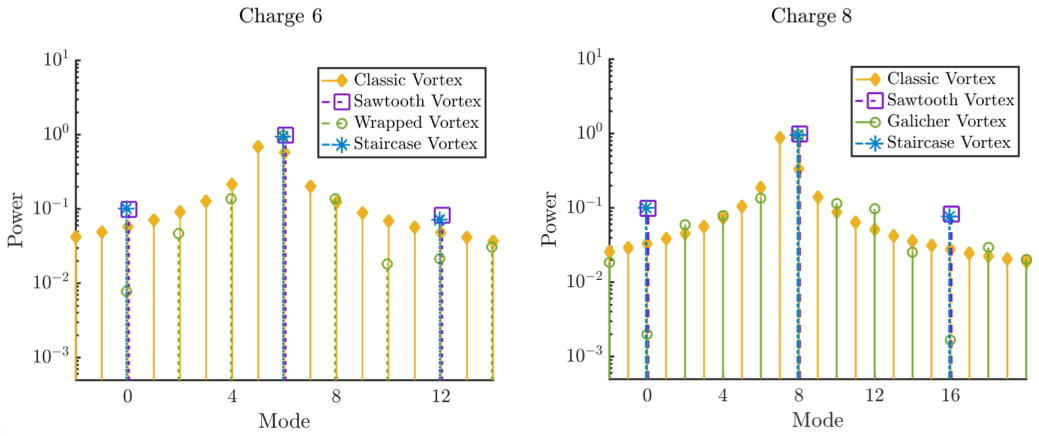

Figure 4.12: Modal decomposition at a 10% wavelength for charge 6 topographies on the left and charge 8 topographies on the right show how each of the classical vortex (yellow), sawtooth vortex (purple), wrapped vortex (green), and wrapped staircase vortex (blue) topographies differ in behavior for broadband light.

the left plot in Figure 4.11. As expected because of the different topological charge vortexes, the charge 6 wrapped mask contrasts did not outperform the charge 8 wrapped mask, however the new charge 6 wrapped design still offers a two order of magnitude improvement at broadband over the other charge 6 topographies.

The newly developed modal decomposition tool was utilized to gain insight into the performance improvement seen with phase wrapping. Figure 4.12 shows that at a 10% offset, the mode corresponding to the vortex charge (six or eight) is still the primary peak for most of the topographies, however other peaks have emerged. The wrapped vortexes shows peaks at mode zero which corresponds to zeroth order leakage, and other even modes, which correspond to smaller vortex charges. These vortexes are known to have worse sensitivities to low-order aberrations and zeroth order leakage. The low zeroth order mode explains the two orders of magnitude improvement in contrast at larger bandwidths seen in Figure 4.11. As seen in this figure, the wrapped vortex (green) has a significantly lower zeroth mode, but also several more peaks at other undesirable modes.

4.8 Modal decomposition potential for optimizing new designs

The modal decomposition representation of a phase mask presented originally in Section 3.4 can also be used to reverse-engineer a new mask design. This is done by selecting certain peaks to suppress: for instance the zeroth mode, odd modes,

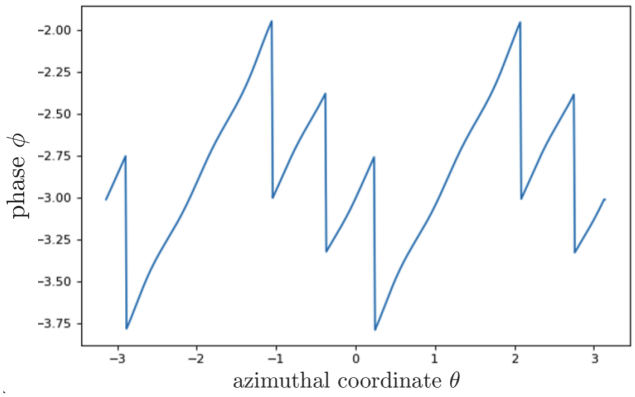

Figure 4.13: A resulting scalar vortex topography phase profile from a preliminary attempt at optimization using modal decomposition to suppress the peak at the zeroth mode.

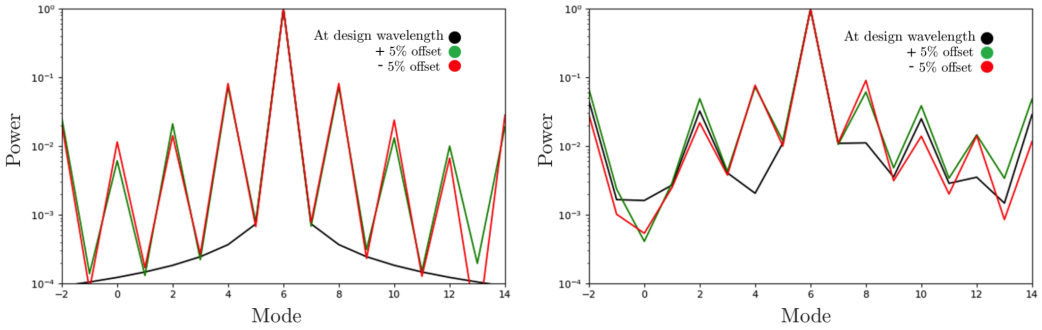

Figure 4.14: Example of using modal decomposition to optimize a phase profile. (left) The original modal decomposition for a charge 6 wrapped vortex at the design wavelength (black), at +5% wavelength offset (green), and at a −5% wavelength offset (red). (right) The modal decomposition after nulling the zeroth order. Although the zeroth mode is partially suppressed, other unwanted modes have an increased intensity, particularly odd modes.

or small even modes, and then mitigating their modal intensity. Then an inverse Fourier transform is applied on this distribution to result in a new phase profile.

This optimization was found to be challenging given our modest understanding of the interplay between modes combined with the difficulties associated with optimizing for a large bandwidth. When trying to suppress one mode, others change in intensity in a way that is not yet understood. Furthermore, covering a large spectral band and nulling the zeroth order at a given wavelength increases the intensity of other

modes in other wavelengths, thus deteriorating low-order aberrations sensitivity and starlight suppression of the mask.

Figure 4.13 shows an optimized phase profile that resulted when carrying out this procedure and Figure 4.14 shows the corresponding modal decompositions before and after suppressing the peak at mode zero. This optimization process is in early stages of development and for this preliminary attempt the L-BFGS-B (limited memory Broyden–Fletcher–Goldfarb–Shanno) based algorithm in scipy was used to optimize the shape of the phase profile for a given number of resolution elements that describe the profile.

This optimized profile is presented as a demonstration of how modal decomposition could be a useful tool for new topography designs with SVCs. The phase profile in Figure 4.13 offers an improvement in terms of contrast for a 25% bandwidth, with only a slight degradation of tip and tilt sensitivity, and no effect on planet throughput and inner working angle. Manufacturing constraints, alignment tolerances, and Lyot stop considerations all have yet to be accounted for.

There remains much exploration space for development of new optimized mask designs with the modal decomposition tool. One advantage is that modal decomposition is able to clearly discern the effective charge for any complex mask design whose charge might not be obvious, like a sinusoidal or otherwise asymmetric topography. The optimized topography will likely be a balance between the desired contrast performance and an acceptable modal sensitivity.

Chapter 5

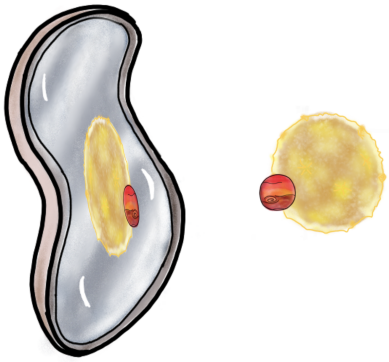

WAVEFRONT SENSING AND CONTROL EXPERIMENTS

Article: A comparative laboratory study of electric field conjugation algorithms

Desai, N., A. Potier, S. Redmond, G. Ruane, A. E. Riggs, P. K. Poon, et al. (2024, Accepted). "A comparative laboratory study of electric field conjugation algorithms". In: *Journal of Astronomical Telescopes, Instruments, and Systems*.

This chapter is also based on work published in the following proceedings:

Desai, N., A. Potier, G. Ruane, A. E. Riggs, P. K. Poon, M. Noyes, and C. Mejia Prada (Oct. 2023). "Experimental comparison of model-free and model-based dark hole algorithms for future space telescopes". In: *Techniques and Instrumentation for Detection of Exoplanets XI*. Vol. 12680. SPIE. DOI: 10.1117/12.2677040.

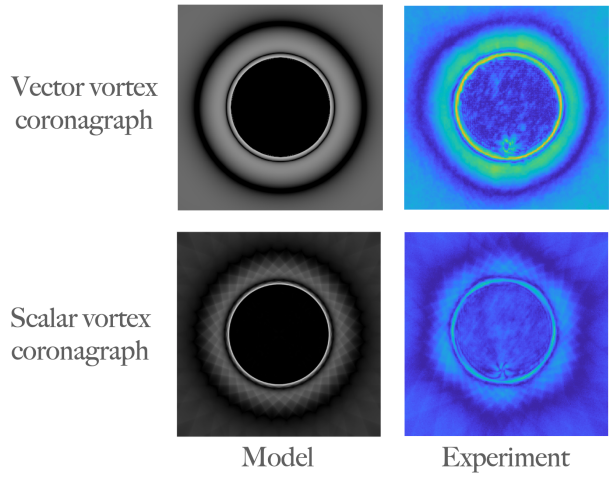

Figure 5.1: Vector and scalar vortex pupil plane images from their theoretical model (left) and from experiment (right) on the In-Air Coronagraph Testbed at JPL.

5.1 Motivation

The predominant method for testing the performance of vector (VVC) and scalar (SVC) vortex coronagraphs in high-contrast imaging testbeds has been the strictly model-based dark hole digging algorithm known as Pairwise Probing with Electric Field Conjugation (PWP + EFC). As shown in Chapter 4, PWP + EFC was found to improve the dark hole average contrast consistently by up to two orders of magnitude. Since this method relies heavily on the model of the focal plane mask (FPM), it is worth comparing the model predictions to the experimental results.

Figure 5.1 shows the same pupil plane images from Figure 4.7 but now adds the simulated theoretical images using the underlying model for a side-by-side comparison. The triangular pattern in the scalar vortex image is due to the staircase nature of the FPM (there are six sectors with six steps each defining the phase ramp). However there is an additional hexagonal shape in the 'ring of fire' in the right experimental scalar vortex image which is not present in the left model image. This potential model-mismatch could be limiting the resulting dark hole contrast. Therefore model-free methods might be interesting to explore with increasingly complex scalar vortex masks.

Recently, two model-free dark hole digging approaches have been proposed: the self-coherent camera (SCC) (Baudoz et al., 2006), compatible with EFC, and implicit electric field conjugation (iEFC) (Ruffio and Kasper, 2022; Haffert et al.,

2023). Notably, these model-free approaches have not been applied to compare the performance of SVCs and VVCs yet. These three techniques were introduced in Chapter 2 and further details on their theory can be found in Section 2.5.

This study aims to understand the differences in applying model-free versus model-based dark hole digging methods through two main goals: 1) compare SVC and VVC performance under identical laboratory conditions and 2) identify the realistic pros and cons of these three wavefront sensing and control algorithms when implemented in the same testbed. The In-Air Coronagraph Testbed (IACT) at the Jet Propulsion Laboratory was employed for conventional model-based PWP + EFC and model-free iEFC, with modifications enabling the implementation of model-free SCC + EFC. This work not only focused on average contrast in broadband light as a performance metric for these three methods but also considered convergence rates and how testbed stability influenced the results for both scalar and vector vortex coronagraphs. This systematic comparison of wavefront sensing and control technologies is imperative to guide the design of future space telescopes.

5.2 Experimental setup

In this study, dark holes were dug on IACT at JPL (see Section 3.5 for a description of IACT) for both the VVC and SVC in uniform conditions in broadband light using all three wavefront sensing and control (WFSC) algorithms. To maintain as many of the experimental conditions constant as possible, the same bandwidths and sub-bands were used. For broadband measurements, the 10% bandwidth was split into three sub-bands. However the coronagraphic FPMs available on IACT have different design central wavelengths. The VVC is a liquid crystal charge 6 vector vortex mask designed with λ_0 = 635 nm and and the SVC is a charge 6 wrapped staircase scalar vortex chromatic mask designed with λ_0 = 775 nm. Note that the intensity of the source, an NKT SuperK supercontinium laser with Varia tunable filter, decreases significantly for wavelengths greater than 650 nm, and has an upper limit of 800 nm. The 10% broadband VVC measurements were centered at λ_0 = 635 nm and the SVC measurements were centered at λ_0 = 760 nm. Consequently the overall flux for the SVC experiments is fainter than for the VVC experiments, making wavefront sensing with SCC more challenging. It is important to note that is not related to the FPM or the WFSC algorithm, but instead due to the continuum light source used on IACT. To account for the different fluxes, the broadband contrast is measured as the averaged intensity of the coronagraphic subband images divided by the peak

intensity of the unocculted broadband point spread function (PSF) image to account for this.

As demonstrated in Chapter 4, IACT has already been used to conduct PWP + EFC for both the VVC and SVC. The VVC and SVC are both mounted on a stage with a Newport LTA actuator, so consecutive experiments can quickly switch between masks while maintaining similar laboratory conditions. In order to implement the SCC, only two modifications in the pupil plane were required: a new Lyot stop with multiple pinholes to create the reference channels, and a pinhole blocker in front of the Lyot mask to open and close the pinholes while keeping the Lyot stop open.

Note that the SCC Lyot stop was designed to have 3 outer pinholes (used for this study) and 3 inner pinholes (for a possible future SCC experiment). The pinhole size was optimized for the VVC central wavelength and their positions were chosen to be within in the VVC 'ring of fire' (a ring of rejected starlight created by the FPM in the Lyot plane) so that the maximum amount of coherent starlight is transmitted through this reference channel. The Lyot stop design used in this study is therefore slightly sub-optimal for the SVC coronagraph (since it operates at a different wavelength). In addition to the custom Lyot stop, the custom pinhole blocker was designed to keep the Lyot stop central channel open while blocking or unblocking various sets of pinholes in a controlled manner. Further details on these upgrades and a comparison in narrowband light of different SCC variations with this pinhole blocker can be found in the supplemental work in Section 5.6.

Both the VVC and SVC on IACT are charge 6 vortex coronagraphs with an inner working angle of 2.4 λ/D. For this reason, the dark hole digging algorithms tested in this study targeted a D-shaped correction region from 3 - 10 λ_0/D. Trials across all three WFSC algorithms were run for 50 iterations. In addition, an oversized D-shaped field stop was used just before the science camera to block the center of the PSF and prevent any ghost reflections from reaching the camera.

5.3 Dark hole results

Figure 5.2 shows the 2% narrowband dark holes dug by all three techniques and their average contrast within a scoring region from 3 - 10 λ/D (in a dashed white line). Since the VVC trials were taken at a shorter wavelength, the dark holes in Figure 5.2 appear smaller than the SVC dark holes, since axes are displayed in terms of λ/D, however they represent equivalent angular separation regimes. In narrowband light

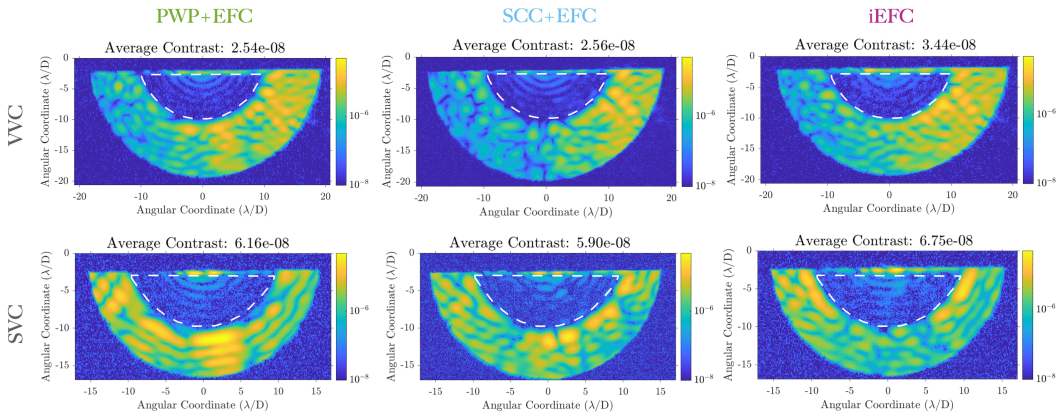

Figure 5.2: Narrowband 2% dark holes and the average contrast within the scoring region from 3-10 λ/D with the vector vortex coronagraph (top row) and scalar vortex coronagraph (bottom row) from the In-Air Coronagraph Testbed with three WFSC algorithms. The VVC measurements were centered at 635 nm and the SVC measurements were centered at 775 nm.

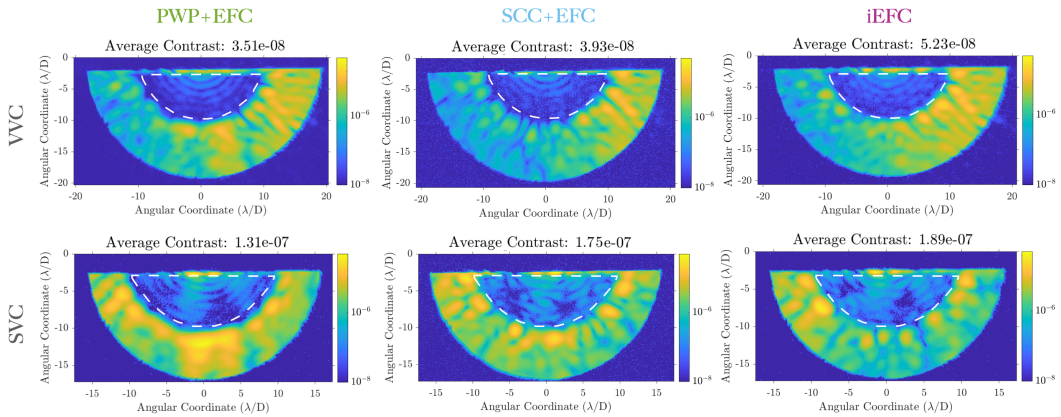

Figure 5.3: Broadband 10% dark holes and the average contrast within the scoring region from 3-10 λ/D with the vector vortex coronagraph (top row) and scalar vortex coronagraph (bottom row) from the In-Air Coronagraph Testbed with three WFSC algorithms. The VVC measurements were centered at 635 nm and the SVC measurements were centered at 760 nm.

with both the VVC and the SVC, the six dark holes presented here all show similar average contrasts roughly between 2-7 $\times 10^{-8}$ within the specified scoring region.

Meanwhile a clear distinction between the average contrasts for the VVC and SVC is visible in broadband light. Figure 5.3 shows the 10% broadband dark holes dug by all three techniques and their average contrast within the same scoring region from 3 - 10 λ/D (in a dashed white line). In broadband, the VVC average contrasts were

	Vector Vortex		Scalar Vortex	
	2%	10%	2%	10%
PWP + EFC	2.54×10^{-8}	3.51×10^{-8}	6.16×10^{-8}	1.31×10^{-7}
SCC + EFC	2.56×10^{-8}	3.93×10^{-8}	5.90×10^{-8}	1.75×10^{-7}
iEFC	3.44×10^{-8}	5.23×10^{-8}	6.75×10^{-8}	1.89×10^{-7}

Table 5.1: Summary table of best dark hole contrasts averaged from 3-10 λ/D for the scalar vortex coronagraph (SVC) and vector vortex coronagraph (VVC) in 2% narrowband and 10% broadband light with pairwise probing (PWP) and electric field conjugation (EFC), self-coherent camera (SCC) with electric field conjugation, and implicit electric field conjugation (iEFC).

all roughly 4×10^{-8} whereas the SVC average contrasts were all generally a factor of 3 worse than the VVC averages, roughly 1×10^{-7}. The consistent performance of the SVC across all three WFSC techniques, reaching approximately an order of magnitude worse contrasts than the VVC in 10% broadband light, indicates a model-mismatch is not the limitation of the SVC.

Additionally between the vector and scalar vortex coronagraphs, aside from the hardware defects mentioned in Section 5.2, a large difference in average contrasts is not present between the narrowband dark holes. A difference is apparent between the broadband results, and is evidence that the SVC contrasts are limited by chromaticity. The VVC dark holes exhibit a clearer ringing pattern compared to the SVC dark holes which show a much less prominent trend. Both the VVC polarization leakage and SVC chromatic leakage would be in the shape of an Airy pattern in the final dark hole and yield profiles like those observed.

Table 5.1 shows a summary of all the average contrasts achieved for both the VVC and SVC obtained with PWP + EFC, SCC + EFC, and iEFC. Overall both the 2% narrowband and the 10% broadband dark holes were consistent across WFSC techniques. Since the dark holes across all three techniques are in agreement, these results indicate the average contrast levels are not limited by the WFSC method. Instead the VVC is likely limited by polarization leakage due to the analyzer/polarizer and the SVC is likely limited by the FPM's chromatic zeroth

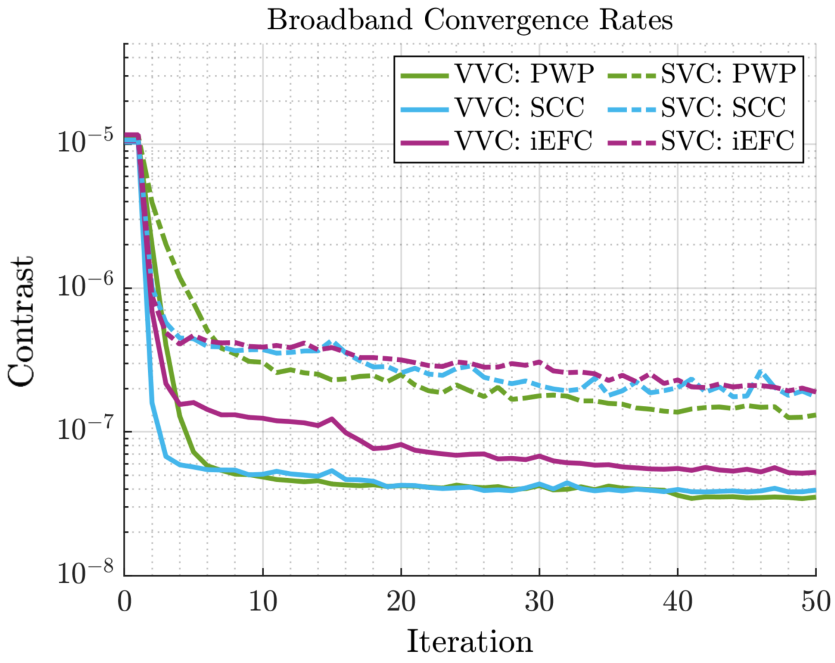

Figure 5.4: Convergence rates of three WFSC algorithms: pairwise probing (PWP) and electric field conjugation (EFC) (green), self-coherent camera (SCC) with electric field conjugation (blue), and implicit electric field conjugation (iEFC) (pink), for both the vector vortex coronagraph (VVC) (solid lines) and scalar vortex coronagraph (SVC) (dotted lines) in a 10% bandwidth plotted against iteration.

order leakage, which is in agreement with the simulated SVC performance (see Chapter 4).

5.4 Convergence rates

One of the primary objectives of this study was not only to use three different dark hole digging methods in one environment and compare the best contrasts achieved, but also to consider the implementations of each and present their advantages and disadvantages.

Figure 5.4 shows the convergence rate of each of the three techniques in 10% broadband light. The trials shown here yielded the best average broadband contrasts within the 3 - 10 λ/D dark hole. The dashed lines are SVC trials and the solid lines are VVC trials. The PWP + EFC trial is shown in green, the iEFC in pink, and the SCC in blue.

The model-free methods reach deeper contrasts in the first few iterations than the model-based method. The faster convergence rates for both SCC + EFC and iEFC

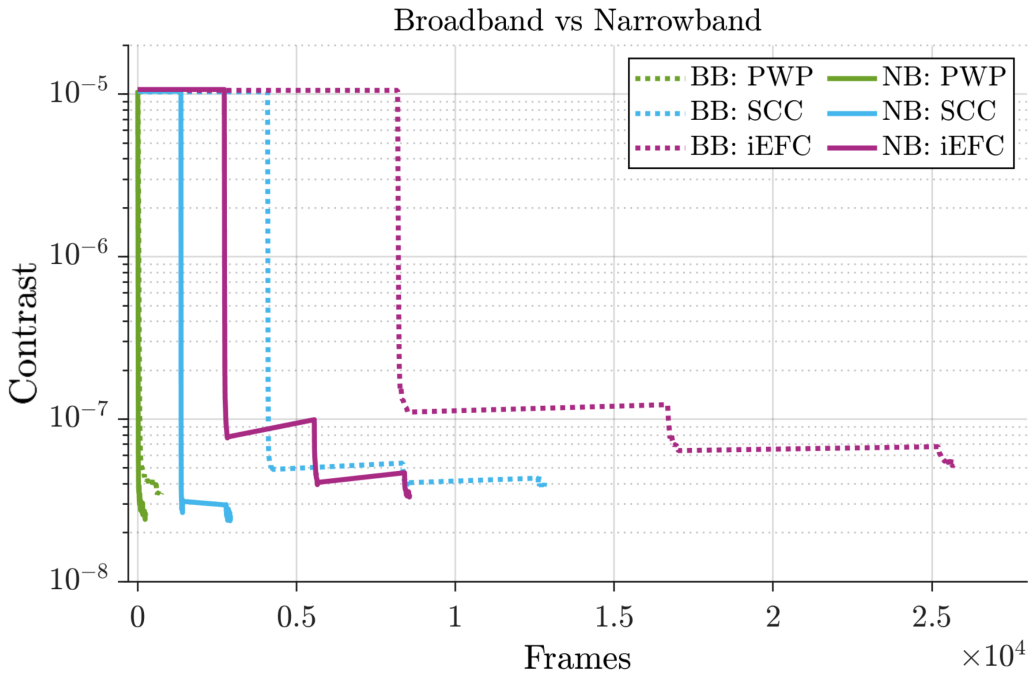

Figure 5.5: Convergence rates of three WFSC algorithms: pairwise probing (PWP) and electric field conjugation (EFC) (green), self-coherent camera (SCC) with electric field conjugation (blue), and implicit electric field conjugation (iEFC) (pink), for both 2% narrowband (NB) light (solid lines) and 10% broadband (BB) light (dotted lines) plotted against number of frames, or total exposures.

are clearly visible for both the SVC and VVC compared to the PWP + EFC. It was expected that the SCC sensitivity would outperform PWP + EFC and iEFC. This is because the PWP + EFC and iEFC algorithms assume a linear approximation that restricts the probe amplitude and therefore the amount of leaked photons used for an accurate E-field estimation (Groff et al., 2016). On the other hand, the SCC is only limited by the number of photons going through the pinholes, which can be increased with more cleverly designed coronagraphs or Lyot stops (Delorme et al., 2016; Martinez, 2019; Gerard and Marois, 2020; Haffert, 2022).

When the same trials are plotted against number of exposures, or frames, and the cost of building the Jacobian without any model is included, this trend is not apparent. Figure 5.5 shows the long period at the start of a trial used to build the Jacobian as well as, for both SCC and iEFC, the periods of relinearization during the trial. The time for deformable mirror (DM) registration, or model calibration for PWP + EFC which can be parallelized and depend on computational power, is not considered here. Additionally the characterization of the DM with a Zygo interferometer, a

time-consuming process that would be required regardless of which algorithm is used, is not included.

In general, the long runtimes for the model-free WFSC techniques are sensitive to testbed instability and PSF drift. It is possible that some of these issues might be avoided on a vacuum testbed, improving measurements during the long exposure times required in these experiments. However, the number of frames required for each of the steps in the model-free techniques would not change and this might be a limiting factor.

5.5 Conclusion

In conclusion, this study found iEFC and SCC + EFC are both high performing model-free dark hole digging methods and ultimately reach equally high broadband contrasts (around 3×10^{-8} for the VVC and around 1×10^{-7} for the SVC in 10% bandwidth) as model-based PWP + EFC. Through the course of implementing these three techniques on IACT, this study reports for the first time applying SCC + EFC for simultaneous multi-subband correction with a field stop.

There are still several improvements possible with the hardware installed for the SCC on IACT. In particular, the SCC Lyot stop pinhole geometry is optimized for the VVC instead of the SVC. The pinhole placement matches the theoretical 'ring of fire' where the VVC mask throws light outside of the Lyot stop radius in the pupil plane, and could be redesigned to better fit the SVC's theoretical 'ring of fire' for potentially improved performance. This would primarily require computing the optimal pinhole separation and size for the SVC mask and design wavelength. Although this study compares the performance of PWP + EFC, SCC, and iEFC directly, it is important to note these three dark hole digging algorithms have not all been fully studied and developed to equal extents. PWP + EFC is the most established of these methods while the code architectures used to implement SCC + EFC and iEFC were both derived from an architecture designed specifically for application to PWP + EFC.

The results show that compared to VVCs, SVC performance is still limited by its chromaticity and likely not by model-mismatch in PWP + EFC. This work therefore definitely motivates the need for better scalar vortex designs. Some ongoing efforts to achromatize scalar vortex coronagraphs include employing hybrid combinations of radial and azimuthal features or utilizing metasurface implementations (Desai et al., 2023a; Desai et al., 2024; König et al., 2023; Palatnick et al., 2023). Both

are strategies which yield complex FPMs that might benefit from model-free WFSC techniques. In general, this study found that model-free techniques are as effective as model-based techniques and might be a preferred choice to deal with more complex mask designs like phase-induced amplitude apodization (PIAA) masks, metasurface scalar vortex phase masks or other future increasingly complex mask designs where model mismatch limits performance (Fogarty et al., 2022; König et al., 2023; Palatnick et al., 2023).

Another main conclusion of this study is that model-free methods require significantly longer time for Jacobian building and are limited by testbed instabilities. In terms of iterations, the model-free methods sometimes converge faster and in the case of SCC + EFC, require less images per iteration. But in terms of number of exposures, the conventional model-based method saves a lot of calibration cost by using a model of the optical system instead of having to tediously poke each Fourier mode on the DM to build the Jacobian. To reduce the number of exposures required to the build the Jacobian, model-free techniques could be improved with a clever choice of mode basis. Or perhaps a hybrid method using the SCC for wavefront sensing and an optical model to compute the DM correction, might offer a balance of the advantages offered by model-free and model-based WFSC techniques.

Supplemental Work

5.6 Variations of the self coherent camera

Building off the classical SCC, two simple modifications further improved wavefront sensing capabilities and were implemented in this study. The first variation was a method of utilizing the SCC without the Fourier transform or side lobe cropping. This method is based on Thompson et al. (2022). Instead of using the Fourier transform of the cropped side lobe to extract the fringe intensity, the image with the closed pinhole is subtracted from the image with the opened pinhole to retain the fringe intensity. This implementation was especially effective on IACT since a field stop in the D-shape of the dark hole is used to block the stray starlight outside the correction region. The hard edges of the field stop pose a significant challenge in the classical SCC since the side lobes in the Fourier transform become substantially distorted. Although the wavefront sensing capability is improved, this variant is slower since two images are required where classical SCC needs only

one. This variant also offers the ability to use pinholes closer to the science channel which potentially extracts more light for wavefront sensing (Martinez, 2019). This capability has not been implemented in this study but will be tested in the future.

Figure 5.6: Hardware upgrades to IACT for implementation of the self-coherent camera. (left) Pinhole blocker placed directly in front of the Lyot stop. (right) Schematic showing the Lyot stop pinholes in purple and the overlayed pinhole blocker in green. The pinhole blocker can move in the vertical axis to either block or unblock pinholes in various configurations.

The second variation on SCC requires opening multiple pinholes instead of just one. As mentioned in Section 5.2, in order to implement the SCC, only two modifications in the pupil plane were required: a new Lyot stop and a pinhole blocker. Figure 5.6 shows the schematic of the Lyot stop pinholes and the pinhole blocker installed on IACT. This multi-reference SCC method is based on Delorme et al. (2016). With 3 pinholes in the Lyot stop, all at the same radius away from the center, overlapping fringes are created in different directions in the coronagraphic image. While Delorme et al. (2016) used such a design to enhance SCC broadband capabilities, here it was used to effectively increase the amount of light in the reference channel and allow for improved wavefront sensing.

Figure 5.7 shows how the convergence rate improved with each SCC variation that was implemented in narrowband light. The first variation, the SCC without the Fourier transform (blue dashed line), performed better than the classical SCC (green dashed line) by a factor of 2 after only 3 iterations.

In comparison to a single pinhole, increasing the number of pinholes to 3 improved the sensitivity, hence the convergence rate now required approximately half the number of iterations. However Figure 5.7 showed that with more pinholes (the dashed pink line with circle markers), the contrast was limited to approximately 3×10^{-8}.

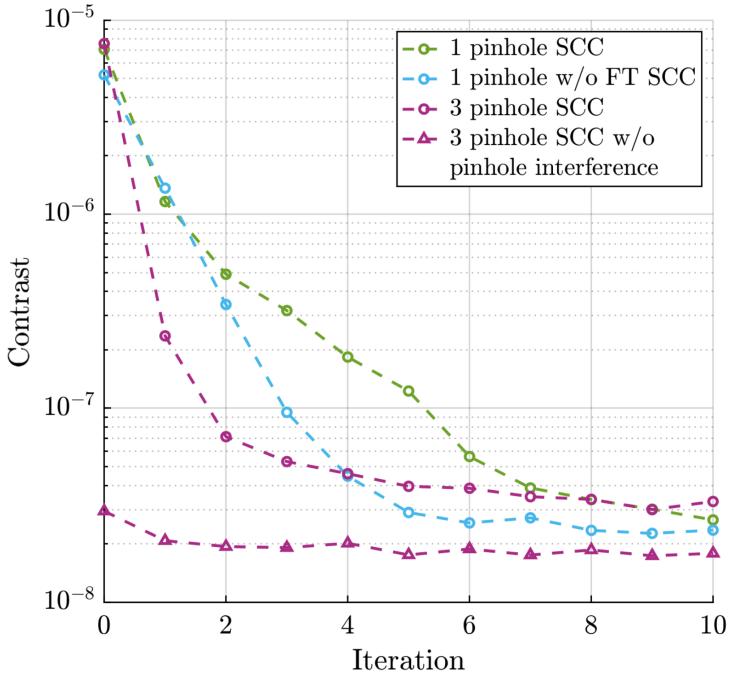

Figure 5.7: Convergence of dark hole digging by classical single pinhole SCC (green), single pinhole SCC without the Fourier Transform (FT) (blue) and triple pinhole SCC without the FT before removing the interference between the pinholes (pink with circle markers) and immediately after (pink with triangle markers).

This was determined to be due to the interference between the pinholes themselves. Figure 5.7 also shows the subsequent trial after removing this light from the estimate (the dashed pink line with triangle markers) by applying a numerical filter to crop out the pinhole interference. This resulted in the triple pinhole SCC reaching better contrast and faster convergence than either of the other SCC variations.

In addition to improving the convergence rate, multiple pinholes enable broadband WFSC with the SCC (Delorme et al., 2016). The classical SCC is indeed limited to narrowband light since broadband light through a single pinhole results in blurred fringes in one particular image direction and poor wavefront sensing (Galicher et al., 2009). With the multi-reference SCC, broadband light would still cause the fringes to blur, but the multi-directional fringes remove any ambiguity in E-field estimation. Although this capability was not used in this study (since broadband measurements were performed through multiple subbands), the increased number of pinholes provided brighter fringes, and hence resulted in better wavefront sensing.

Chapter 6

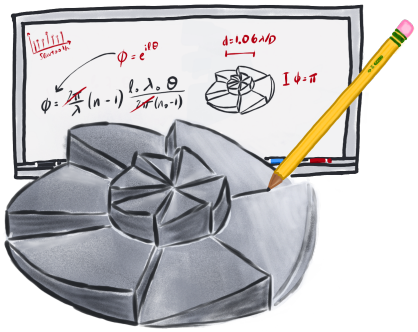

SECOND GENERATION SCALAR VORTEX CORONAGRAPHS

Article: Benefits of adding radial phase dimples on scalar coronagraph phase masks

Desai, N., D. Mawet, E. Serabyn, G. Ruane, A. Bertrou-Cantou, J. Llop-Sayson, and A. J. E. Riggs (Feb. 2024). "Benefits of adding radial phase dimples on scalar coronagraph phase masks". In: *Journal of Astronomical Telescopes, Instruments, and Systems* 10.1, p. 015001. DOI: 10.1117/1.JATIS.10.1.015001.

This chapter is also based on work published in the following proceedings:

Desai, N., A. Bertrou-Cantou, G. Ruane, J. Llop-Sayson, A. E. Riggs, E. Serabyn, and D. Mawet (Oct. 2023). "Achromatizing scalar vortex coronagraphs with radial phase mask dimples". In: *Techniques and Instrumentation for Detection of Exoplanets XI*. Vol. 12680. SPIE. DOI: 10.1117/12.2677224.

6.1 Motivation

In this chapter, phase mask concepts introduced by F. Roddier and C. Roddier (1997) and Soummer et al. (2003) are revisited and investigated in combination with current scalar phase mask coronagraph concepts to suppress chromatic stellar leakage. This study investigates potential new designs which combine radial features with current azimuthal-only topographies using simulations of 2D wavefront propagation for these proposed scalar phase masks. The proposed mask designs would work with an unobscured circular aperture, including segmented apertures (an off-axis segmented aperture is one of the designs currently considered for the Habitable Worlds Observatory (HWO)). More generally this work demonstrates the potential for hybrid radial and azimuthal focal plane mask (FPM) design techniques which could be applied to future phase mask designs to achromatize their performance.

New designs are needed to make scalar vortex coronagraphs (SVCs) more achromatic and comparable in performance to vector vortex coronagraphs. Recently, there have been several different attempts to achromatize SVC designs including varying the FPM surface topography (Galicher et al., 2020; Desai et al., 2022), combining two materials of different refractive indices into a dual-layer FPM, (Swartzlander, 2006; Ruane et al., 2019) or employing metasurfaces optimized for broadband phase control (König et al., 2023; Palatnick et al., 2023).

6.2 Radial phase mask dimples

This chapter considers two specific radial phase mask designs (originally introduced in Chapter 2): the Roddier & Roddier dimple (referred hereafter as the 'Roddier dimple'; F. Roddier and C. Roddier (1997)) and the Dual Zone Phase Mask (referred hereafter as the 'DZPM dimple'; Soummer et al. (2003)).

F. Roddier and C. Roddier (1997) originally proposed an improvement of Lyot's stellar coronagraph, by replacing the occulting mask with a transparent π phase shifting mask. The left schematic in Figure 6.1 shows the Roddier dimple dimensions. For the central wavelength λ_0, the phase shift of the mask should be π and the size of the dimple should have a radius of $0.53\lambda_0/D$. The optimal size for the Roddier dimple corresponds to 0.43 times the size of the first Airy ring since it encircles 50% of the energy of the Airy pattern (Born and Wolf, 1980). The working principle is to create a phase-shifted region of a specific size so the exactly balanced fluxes, inside the dimple region and outside the dimple region, cancel each other due to their opposite phases.

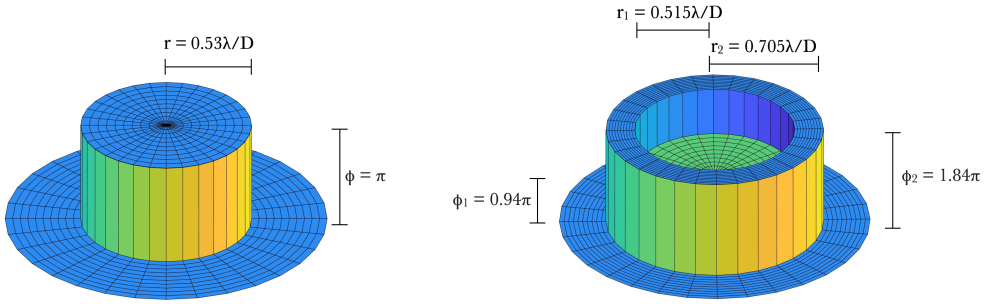

Figure 6.1: Schematics of existing phase dimple designs. (left) The Roddier phase dimple with lateral dimensions and phase shift (F. Roddier and C. Roddier, 1997). (right) The Dual Zone Phase Mask dimple (Soummer et al., 2003).

Soummer et al. (2003) identified that the Roddier & Roddier phase mask suffers from two chromatic effects: the first is in the effective phase shift of the dimple, and the second is in the amount of flux going through the dimple. When the wavelength decreases slightly, the Airy disk shrinks resulting in more energy being concentrated in the central dimple. They proposed a generalization of the Roddier dimple, an alternative dual zone phase mask with better broadband performance and conducted a more thorough optimization study of the parameter space for the size and phase shift of both zones. They also considered optimizing the DZPM for 20%, 30% and 40% broadband coverage. One of their findings was that with large phase steps, the phase shift is more chromatic, making it more difficult to compensate over large bandwidths. This study focuses on comparing FPMs and therefore only considers the parameters of the unapodized DZPM shown in the schematic on the right in Figure 6.2. The final parameters of the DZPM for an unapodized pupil are shown in the schematic on the right in Figure 6.1. For the central wavelength λ_0, the DZPM dimple consists of a central zone of radius $0.515\lambda_0/D$ with a phase shift of 0.94π next to an annulus region with an outer radius of $0.705\lambda_0/D$ with a phase shift of 1.84π radians. Note, the performance of both the Roddier and DZPM coronagraphs is limited in terms of contrast for simple circular unobstructed apertures. Although not considered in this study, solutions with apodized entrance pupils have been shown to increase the contrast performance of both of these coronagraph masks. Of the several DZPM solutions recommended by Soummer et al. (2003), the highest performance ones involved the use of an apodized pupil.

6.3 Hybrid scalar phase mask topographies

I simulated several different azimuthally modulated scalar phase mask topographies of charge 6 to perform a direct comparison of their broadband performance. The Fast Linearized Coronagraphic Optimizer (FALCO)[1] software package (introduced in Chapter 3) was used to assess the chromaticity of the designs proposed in this paper as coronagraphic FPMs (Riggs et al., 2018). The point spread function (PSF) of a star, and 2D wavefront propagation through all subsequent pupils and optics including the FPM was simulated to measure the contrast performance without any deformable mirror (DM)-assisted wavefront correction. To simulate the various FPMs proposed below, high resolution phase mappings were developed and resolution parameters were adjusted in the wavefront propagation pipeline to find an appropriate simulation environment for coronagraph mask development. In this study, four base scalar phase mask designs are considered:

Classic Vortex: The first scalar phase mask design considered is the classic vortex. A classic scalar vortex is a simple phase ramp wrapping around the optical axis, and its slope is proportional to the charge of the vortex. For example a charge 6 classic vortex is a linear ramp from 0 to 12π, which in practice would result in thick optics less suited for the focal plane.

Sawtooth Vortex: The second scalar phase mask design considered in this study is a phase-wrapped version of the classic vortex. It is referred to as the 'sawtooth' vortex SVC because the azimuthal profile of this mask looks like a sawtooth pattern. In the sawtooth vortex design, l phase ramps range from 0 to 2π. The charge of the vortex, l, dictates the number of phase ramps, and therefore the slope (which is piece-wise identical to the classic case).

Cosine: The third scalar phase mask design considered is the sinusoidal phase mask. This mask design is described by an azimuthal cosine-modulated phase function which spans six periods (Hénault, 2015; Hénault et al., 2016).

Wrapped Vortex: The fourth scalar phase mask design is the wrapped vortex which is inspired by the phase wrapping method proposed by Galicher et al. (2020). The design considered here is a charge 6 vortex version (see Chapter 4). This design was obtained with an azimuthal profile optimization using the position of the 2π jumps as parameters.

[1] `https://github.com/ajeldorado/falco-matlab`

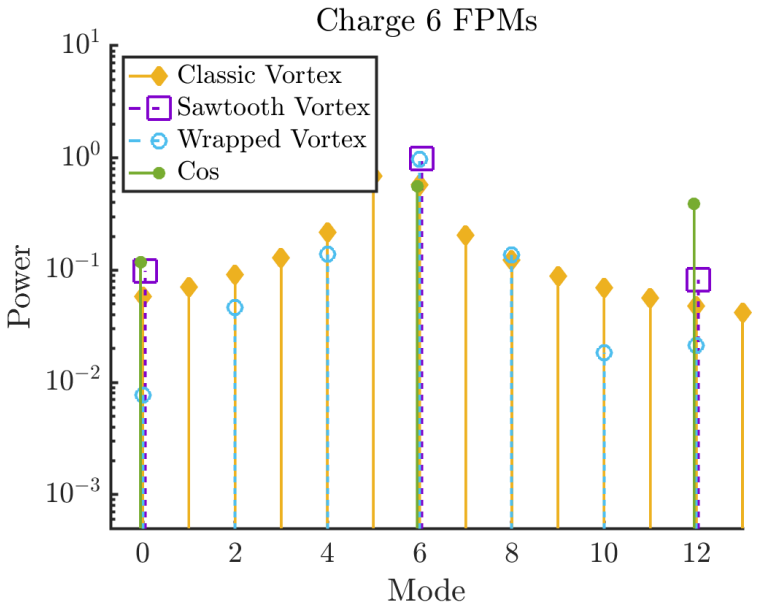

Figure 6.2: Modal decomposition at a 10% wavelength offset ($\lambda_0/\lambda = 1.1$) of the classic vortex (yellow), sawtooth vortex (purple), wrapped vortex (blue), and cosine phase mask (green).

To understand the chromaticity of these scalar phase masks, modal decompositions (as presented in Section 3.4) of the azimuthal phase profile for the four cases considered were performed at a 10% wavelength offset ($\lambda_0/\lambda = 1.1$) and are shown in Figure 6.2 (Ruane et al., 2018; Desai et al., 2022).

The modal decomposition of the sawtooth vortex reveals that no odd or low even modes emerge apart from the zeroth order mode. The modes that emerge are at a base frequency of the charge, in this case $l = 6$ so there are modes at 6, 12, 18, etc. as seen in Figure 6.2. This property of the sawtooth offers a significant advantage over the classic vortex (for which the base frequency is 1), not only for increased insensitivity to low order wavefront aberrations, but also for improved broadband performance.

A modal decomposition for the sawtooth vortex and cosine phase mask reveals that the zeroth order mode (central leakage) needs to be suppressed for better broadband performance. To suppress the zeroth mode leakage, we explore adding central phase dimples. This is because central phase dimples only have zeroth order leakage which can balance that of the vortex, without affecting higher azimuthal orders. This radial modulation is not expected to change the power distribution in the modal decomposition since it is only dependent on azimuthal features.

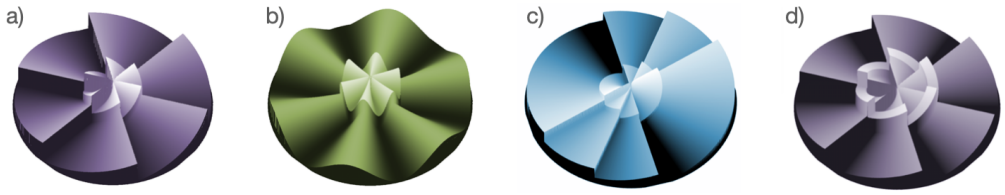

Figure 6.3: The 3D renderings of each of the focal plane phase masks considered in this study: (a) Sawtooth Vortex+Roddier, (b) Cosine+Roddier, (c) Wrapped Vortex+Roddier, (d) Sawtooth+Dual Zone Phase Dimple.

This study investigates the effects of employing radial phase dimples in current scalar phase mask designs. The masks considered here add a Roddier dimple to the sawtooth vortex, wrapped vortex and cosine designs. Additionally, a DZPM dimple was added to the sawtooth vortex to investigate whether a significant effect on broadband performance resulted. Figure 6.3 shows the 3D renderings of these four focal plane scalar phase masks.

6.4 Simulated contrast performance

Each of the designs discussed hereafter in this chapter was simulated and evaluated with 2D wavefront propagation. The average contrast in the 3 - $10\lambda_0/D$ region was calculated for 19 discrete wavelengths equally spaced across a 20% bandwidth. For 10% bandwidth contrast measurements, the same spectral sampling was used. The raw contrast here is defined as the ratio of the average intensity in the region of interest in the coronagraphic image to the highest intensity in the non-coronagraphic PSF. The resulting chromaticity V-curve in Figure 6.4 shows that although adding the Roddier dimple or DZPM to the sawtooth is still chromatic, it improves performance by at least an order of magnitude consistently across a 20% bandwidth. More specifically, compared to a classic vortex, the contrast is improved by over 100× across a 10% bandwidth ($\lambda_0/\lambda = 0.95$ or $\lambda_0/\lambda = 1.05$) and roughly 30× at the far edges of the 20% bandwidth ($\lambda_0/\lambda = 0.9$ or $\lambda_0/\lambda = 1.1$).

The same simulation pipeline was used to compute the throughput of a simulated planet at angular separations ranging from 0 - 20 λ_0/D for comparison between the sawtooth vortex mask and the hybrid vortex mask designs. The addition of the central phase dimples was not expected to affect the throughput or inner working angle of a standard charge 6 vortex coronagraph. The simulation found the throughput as a function of angular separation for the sawtooth SVC and the Roddier dimpled

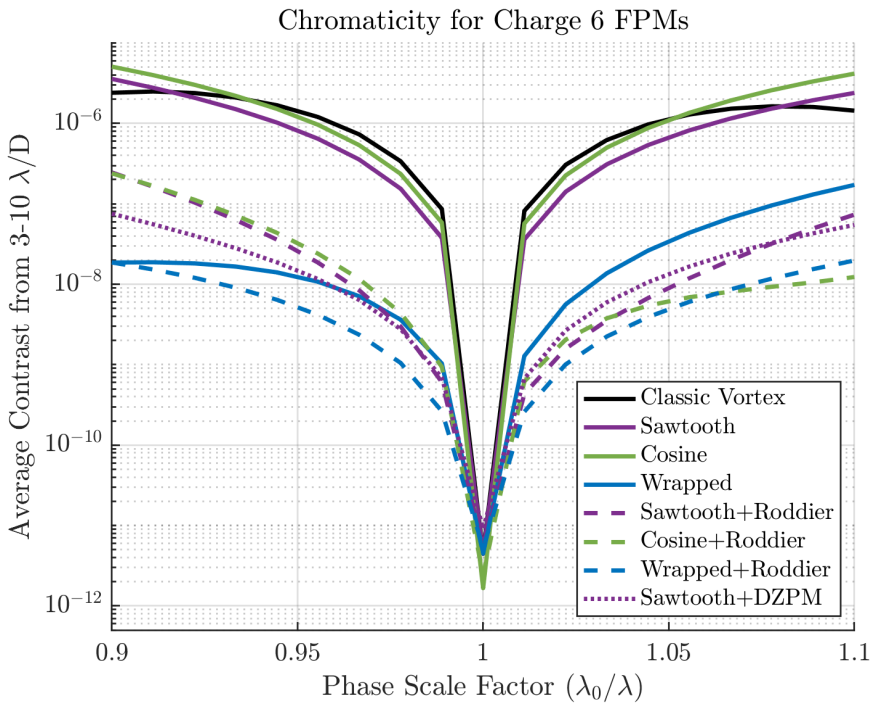

Figure 6.4: Chromaticity V-curve showing simulated average contrast from 3-10 λ_0/D across a 20% bandwidth. The solid lines correspond to the 4 base scalar phase mask designs considered in this study: classic vortex (black), sawtooth vortex (purple), cosine (green) and wrapped vortex (blue). The dashed lines correspond to the same 4 designs with a Roddier dimple added. The Dual Zone Phase Mask dimple with a sawtooth vortex (purple dashed) is also shown.

sawtooth SVC to be overlapping, both yielding 50% throughput at an inner working angle of 2.4 λ_0/D.

Figure 6.5 compares the radial profiles of the 20% broadband final coronagraphic image for each of the four proposed designs with the non-coronagraphic PSF (black). The figure illustrates the starlight attenuation effects of the Roddier dimple and the DZPM dimple and especially shows the contrast improvement compared to the non-coronagraphic profile.

Table 6.1 shows the average raw contrasts in 10% and 20% broadband light from 3 - 10 λ_0/D in the simulated coronagraphic image for the four base scalar phase mask designs, the three hybrid Roddier dimple designs as well as the hybrid dual zone phase dimple design considered in this study. Three main conclusions can be drawn from this table. Firstly, sawtooth design shows a significant improvement over the classic vortex: the 10% broadband results show a factor of 2× contrast gained.

	Bandwidth	
	10%	20%
Vortex	4.06×10^{-7}	1.17×10^{-6}
Sawtooth	2.03×10^{-7}	1.00×10^{-6}
Cosine	3.16×10^{-7}	1.56×10^{-6}
Wrapped	6.36×10^{-9}	3.16×10^{-8}
Sawtooth + Roddier	3.77×10^{-9}	3.79×10^{-8}
Cosine + Roddier	4.76×10^{-9}	3.3×10^{-8}
Wrapped + Roddier	1.40×10^{-9}	6.62×10^{-9}
Sawtooth + DZPM	3.78×10^{-9}	2.03×10^{-8}

Table 6.1: Simulated broadband average raw contrast in 3-10 λ_0/D.

Secondly, it can be clearly seen that adding a radial phase dimple in addition to using the sawtooth pattern: for 20% broadband, the Roddier dimple provides a factor of 26× contrast improvement and the DZPM dimple offers a 49× factor of improvement over the sawtooth vortex alone. Lastly, the DZPM dimple solution does not provide a significant advantage over the simpler Roddier dimple. Overall, using a hybrid sawtooth design clearly provides improved contrast performance compared to classic vortex: the Sawtooth+Roddier design and the Sawtooth+DZPM design yield a 108× factor improved average contrast.

In Figure 6.4 the Roddier dimple not only shows a significant improvement when added to the sawtooth vortex design, but also for the cosine design. Table 6.1 shows a contrast improvement by a factor of 66× in 10% and 46× in 20% bandwidth. However for the wrapped vortex, adding the Roddier dimple only provides a factor of 4× for 10% or 20%. These results agree with the modal decompositions shown in Section 6.3. Since the wrapped vortex already has a small zeroth order mode, there is only a minor improvement to the central leakage from the Roddier dimple.

6.5 Sensitivity to low-order aberrations

A high-performing FPM appropriate for a future space telescope mission would not only demonstrate good starlight suppression across a large bandwidth, but also be insensitive to low-order wavefront aberrations. Figures 6.6 and 6.7 show the sensitivity of these proposed coronagraph phase masks to tip/tilt, defocus, spherical,

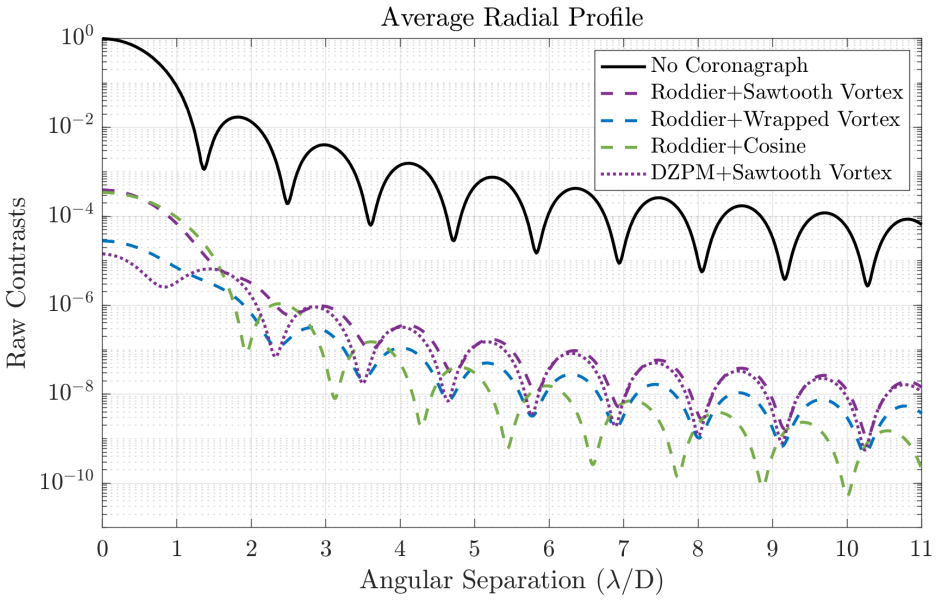

Figure 6.5: Average radial profiles for 20% broadband light simulated for four proposed hybrid focal plane phase masks compared to the non-coronagraphic point-spread function (black). The four hybrid mask profiles correspond to the coronagraphic focal plane image with the Roddier dimple added to the Sawtooth (purple dashed), Wrapped Vortex (blue dashed) and Cosine (green dashed) as well as the Dual Zone Phase Dimple added to the Sawtooth (purple dotted).

astigmatism, and coma Zernike aberrations for monochromatic and broadband light. Figure 6.6 simulates wavefront error at $\lambda_0 = 650$ nm, and Figure 6.7 shows the averaged 20% broadband result.

The stellar leakage is averaged over effective angular separations across $3 \pm 0.5\,\lambda_0/D$, and normalized to the peak leakage without the coronagraph masks, as a function of root-mean-square (RMS) wavefront error for each Zernike aberration. These can be directly compared to current capabilities and requirements on wavefront stability.

A vortex coronagraph's sensitivities follow a notional power law as described in Ruane et al. (2018). The sensitivity to each aberration depends on the vortex charge l and the corresponding Zernike polynomial $Z_n^m(r/a, \theta)$, where n is the radial degree and m is the azimuthal degree and a is the radius of the circular pupil over which the phase is described. The radial and azimuthal degrees of the Zernike polynomials are non-negative integers and with $n \geq |m| \geq 0$ ($m = 0$ for spherical Zernike polynomials).

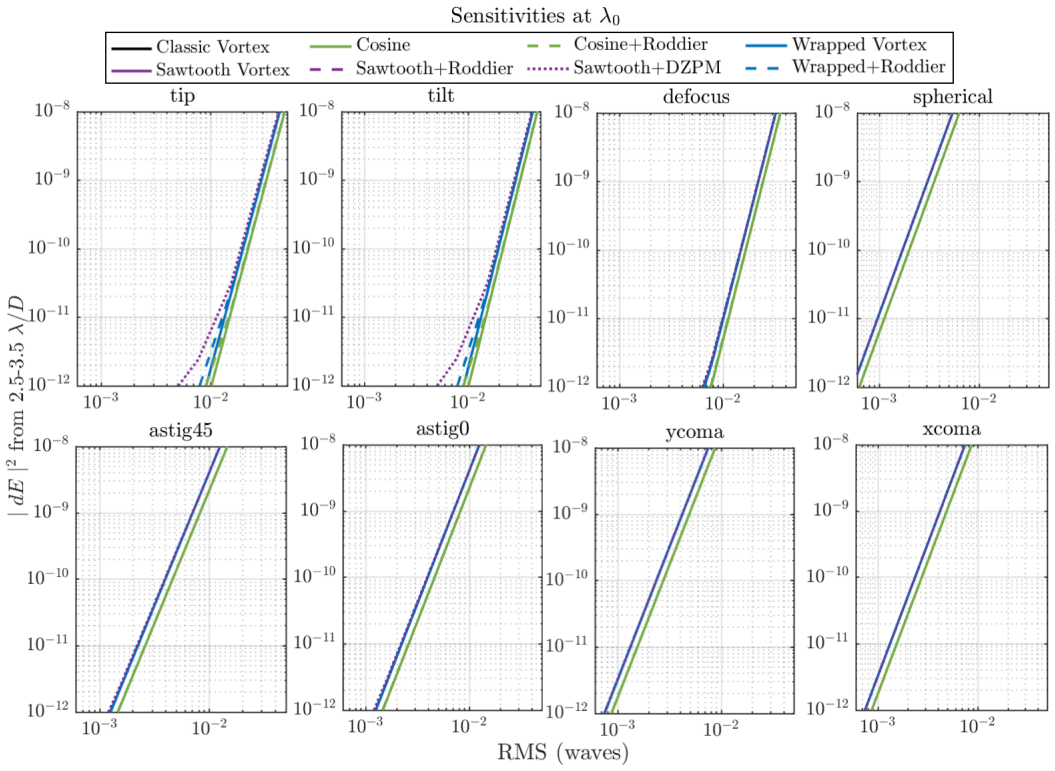

Figure 6.6: Monochromatic sensitivities to the lowest order Zernike aberrations (tip, tilt, defocus, spherical, astig, coma). The average change in stellar leakage across $3 \pm 0.5\ \lambda_0/D$ is shown as a function of root-mean-square (RMS) wavefront error. The solid lines shown here are the four base focal plane masks (classic vortex, sawtooth vortex, wrapped vortex, and cosine). The dashed and dotted lines correspond to hybrid designs incorporating a Roddier phase dimple and dual zone phase dimple, respectively.

The Zernike polynomials may be written as

$$Z_n^m(r/a,\theta) = R_n^{|m|}(r/a) \begin{cases} \cos(m\theta) & m \geq 0 \\ \sin(|m|\theta) & m < 0 \end{cases}, \quad r \leq a, \tag{6.1}$$

where $R_n^m(r/a)$ is the radial Zernike polynomial given by

$$R_n^m(r/a) = \sum_{k=0}^{\frac{n-m}{2}} \frac{(-1)^k (n-k)!}{k!\left(\frac{n+m}{2}-k\right)!\left(\frac{n-m}{2}-k\right)!} (r/a)^{n-2k}, \quad r/a \leq 1. \tag{6.2}$$

For a given charge l, the vortex coronagraph filters out aberrations corresponding to Zernike polynomials with $n + m < l$, or in other words, it is weakly sensitive to these aberrations. These are the Zernike aberrations in the "null space" for a vortex coronagraph. So for charge 6, this includes tip and tilt, defocus, astigmatism,

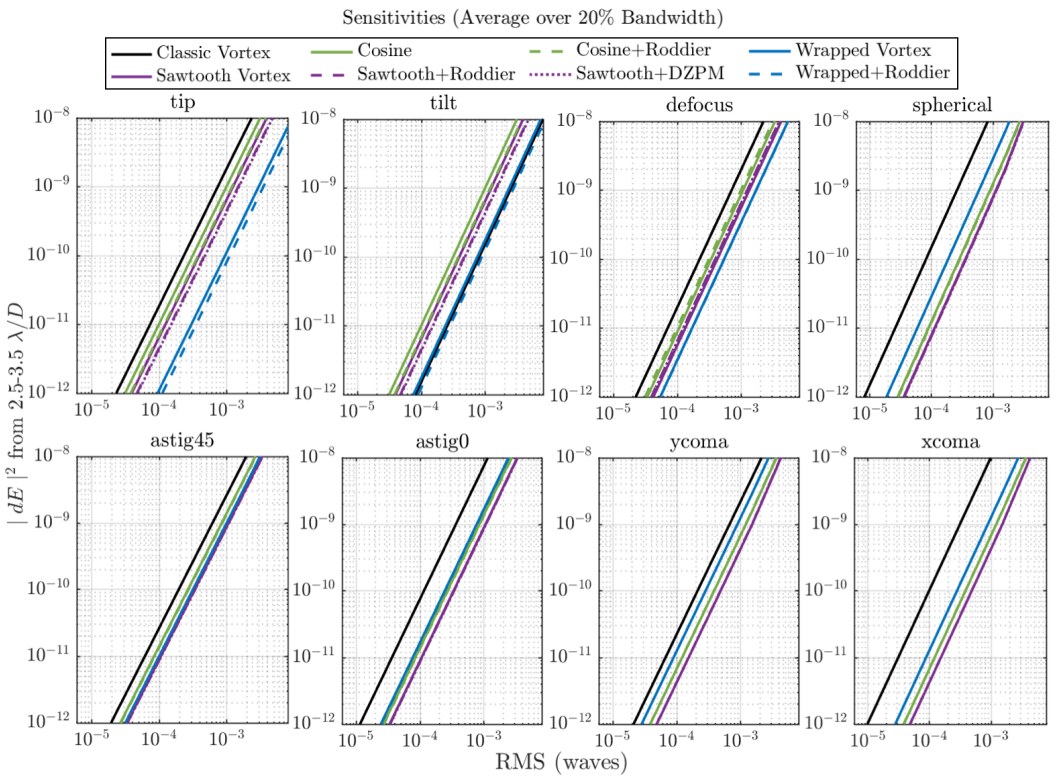

Figure 6.7: Broadband sensitivities to the lowest order Zernike aberrations (tip, tilt, defocus, spherical, astig, coma). The average change in stellar leakage across 3 $\pm$ 0.5 λ_0/D is shown as a function of root-mean-square (RMS) wavefront error. The solid lines shown here are the four base focal plane masks (classic vortex, sawtooth vortex, wrapped vortex, and cosine). The dashed and dotted lines correspond to hybrid designs incorporating a Roddier phase dimple and dual zone phase dimple, respectively.

coma and spherical aberrations. A theoretical vortex coronagraph's sensitivity to the Zernike aberrations in the null space of a charge 6 vortex were reported in Ruane et al. (2018) and can be seen in Table 6.2. In monochromatic light at the design wavelength, all of the scalar vortex designs follow this behavior. However power law fits of the sensitivity orders for the hybrid scalar vortex designs in Figure 6.7 reveal that the out-of-band sensitivity is degraded for all the Zernike aberrations in the null space to 2nd order power laws (Table 6.2). Adding a phase dimple does not restore the notional sensitivity power law properties in broadband light, which is postulated to be due to the still dominant chromatic leakage.

In monochromatic light, there is not a significant difference in sensitivity between the scalar phase mask topographies. Figures 6.6 and 6.7 show that overall no

Zernike	Z_n^m	Theoretical charge 6 vortex coronagraph	Monochromatic SVC (with and without dimple)	Broadband SVC (with and without dimple)
tip/tilt	$Z_1^{\pm 1}$	6	6	2
defocus	Z_2^0	6	6	2
astigmatism	$Z_2^{\pm 2}$	4	4	2
coma	$Z_3^{\pm 1}$	4	4	2
spherical	Z_4^0	4	4	2

Table 6.2: Zernike aberration sensitivities: power laws

significant impact to the sensitivities to low-order aberrations is noticed when a Roddier dimple or DZPM dimple is added. Table 6.2 reports the power laws measured from sensitivity plots in Figures 6.6 and 6.7 for each of the Zernike aberrations in the null space of a charge 6 vortex coronagraph. Table 6.2 shows that in 20% broadband light, the nominal sensitivity power law is not restored by attenuating the central leakage with a phase dimple. For the other aberrations: spherical, coma, and astigmatism aberrations, the phase masks with the Roddier dimple or DZPM dimple (dashed or dotted lines) are indistinguishable from the phase masks without them (solid lines). Comparing between the scalar phase mask designs for tip, tilt and defocus, the wrapped vortex has the least sensitivity followed by the sawtooth vortex and then the cosine design. The sawtooth vortex is the most robust to spherical, astigmatism and coma, followed by the cosine design, the wrapped vortex and the classic scalar vortex is the most sensitive. This indicates for the sawtooth design, larger errors may be tolerated on these low order aberrations, which typically dominate the dynamic wavefront error budget.

6.6 Optimizing the phase dimple

The next step is to investigate whether the parameters of the Roddier dimple require re-optimization when paired with a sawtooth vortex. Figure 6.8 shows how the average raw contrast from 3 - 10 λ_0/D varies with bandwidth and dimple size. This simulation found that for monochromatic light, the contrast is insensitive to a slightly larger or smaller phase dimple. However as the bandwidth increases, the optimal Roddier dimple radius grows slightly larger. The optimal dimple radius values for each of the bandwidths is shown in Table 6.3. The DZPM mask is not considered in this optimization since little contrast improvement was observed in the uncorrected 2D wavefront propagation results (see Table 6.1).

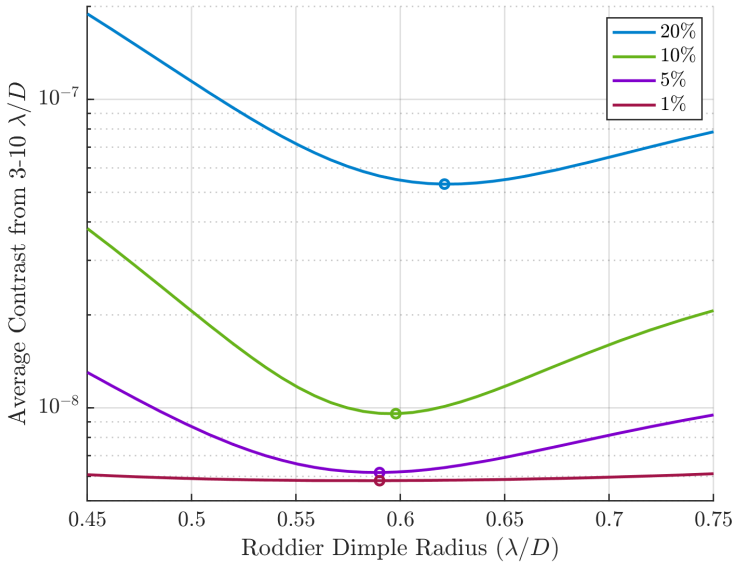

Figure 6.8: Sweep of Roddier phase dimple sizes in combination with the sawtooth vortex. Average contrast in final focal plane from 3 - 10 λ_0/D shown for 1%, 5%, 10%, and 20% bandwidths (note 5 wavelengths were sampled across the bandpass to reduce computation). The optimal radius for each bandwidth is marked with a circular marker and values are reported in Table 6.3.

Bandwidth	Radius (λ/D)
1%	0.590
5%	0.590
10%	0.600
20%	0.621

Table 6.3: Optimal radius of Roddier phase dimples for Sawtooth SVC.

6.7 Conclusion

The potential benefit of adding radial phase dimples to scalar vortex masks to improve broadband performance is investigated, with the goal of addressing zeroth order leakage in current scalar vortex designs. A Roddier dimple was superimposed on a sawtooth vortex design, wrapped vortex design, and a cosine design. Additionally a DZPM dimple was superimposed on a sawtooth vortex design. Simulations of 2D wavefront propagation found that adding a Roddier dimple improves

the sawtooth vortex average contrast by a factor of 53× and 26× in a 10% and 20% bandwidths, respectively. With the DZPM dimple, the sawtooth vortex average contrast is improved by the same factor of 53× in 10% bandwidth, and by a factor of 49× in 20% bandwidth. Furthermore, for the cosine phase mask, adding a Roddier dimple was found to improve the average contrast by 66× and 46×, in 10% and 20%, respectively. Lastly, for the wrapped vortex mask, which already offers improved broadband performance compared to the classic vortex, adding the Roddier dimple was only found to have a moderate impact of roughly a 4× factor of improvement to contrast for both 10% and 20%.

Sensitivity analysis demonstrated that adding the radial phase dimples does not restore the notional sensitivity to low-order wavefront aberrations power law, as expected. Scalar vortex masks, even with suppressed zeroth order leakage, are still significantly more sensitive to aberrations out-of-band and follow a quadratic power law. The sawtooth design has also been identified as more insensitive to most low-order aberrations than the cosine or wrapped vortex designs. The hybrid sawtooth with a phase dimple design offers a factor of almost 100× improvement in contrast over the classic vortex, and considering both the sensitivity robustness and contrast performance, is a likely choice for next steps of manufacturing and testing on a high contrast optical bench. This is discussed further in Section 7.2.

These results show that radial phase mask dimples are a promising technique to apply to new scalar vortex designs. A sweep of the Roddier phase dimple parameters indicates a shift in optimal size for different bandwidths. This suggests that it may be essential to consider re-optimizing the parameters when integrating radial features like the Roddier dimple with other scalar phase masks. Although the standalone Roddier and DZPM coronagraphs demonstrate better performance with apodized entrance pupils, these apodizers do not work well with the vortex coronagraph, which prefers circular uniform apertures. However, recent experiments with carbon nanotube microdot apodizers in combination with the vortex coronagraph have demonstrated successful elimination of starlight leakage due to segment gap diffraction to the 10^{-8} level (Bertrou-Cantou et al., 2023). Similar apodizers could easily be combined with the hybrid designs presented here for application in ground-based telescopes with obstructed apertures.

While adding a central dimple improves simulated performances by up to two orders of magnitude in some cases, the predicted dark regions are still one to two orders of magnitude away from the ultimate 10^{-10} level needed for terrestrial planet

observations from space. Nevertheless, the performance is certainly more than sufficient for use on the next generation of very large ground-based telescopes. To reach the HWO target contrast value of 10^{-10} across a 20% bandwidths, additional achromatization techniques will thus likely be necessary, such as using phase dimples together with achromat plate combinations (Swartzlander, 2006; Ruane et al., 2019) or metasurfaces (König et al., 2023; Palatnick et al., 2023) (see Chapter 7).

Supplemental Work

6.8 Wavefront correction with hybrid mask designs

After characterizing the impact of adding the Roddier dimple and DZPM dimple to the sawtooth vortex on broadband performance, wavefront sensing and control simulations were performed to determine whether closed loop correction reaches even deeper contrasts. FALCO was used to simulate pairwise probing with EFC, introduced in Chapter 2, was applied to dig a dark hole across a 20% bandwidth with 5 sub-bandpasses and one 34×34 actuator DM. EFC was run for 10 iterations with a specified 180° D-shaped correction region from 5-10 λ/D. Figure 6.9 shows the resulting dark holes after correction as well as the final DM surfaces. EFC applied to the sawtooth design alone reaches an average contrast of 3.87×10^{-7}, a factor of $> 2.5\times$ improvement. A similar gain was expected with the Roddier+Sawtooth design, but wavefront control only yields minor improvement (a factor of $< 1.2\times$). A larger gain was observed with the DZPM+Sawtooth design as wavefront control reaches an average contrast of 9.95×10^{-9}, a factor of roughly $2\times$ improvement.

Overall, closed loop wavefront control was found to only show minor improvement in contrast. Additionally, the final DM surface maps computed to minimize the electric field in the final dark hole show very little DM stroke. This either indicates that the wavefront control is limited by the amount of correction it can provide since the sawtooth pattern is already more achromatic than the classic vortex, or that the radial phase dimples inhibit the EFC algorithm from determining a DM solution optimized across a large bandwidth. A possible explanation could be that the optimal correction at one end of the band, at $\lambda_0/\lambda = 0.9$, is the opposite DM shape to the optimal correction at the other end of the band, at $\lambda_0/\lambda = 1.1$, thus resulting in a solution with little contrast improvement and low DM stroke.

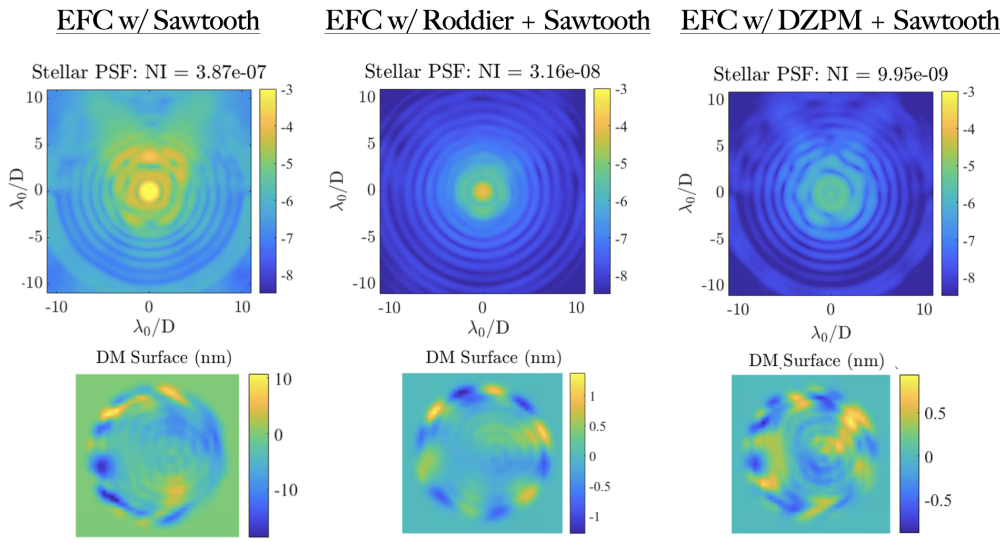

Figure 6.9: Simulated closed loop correction with the Sawtooth (left), Roddier+Sawtooth (middle) and DZPM+Sawtooth (right) topographies for 20% broadband. Top: 180° D-shaped dark holes from 5-10 λ/D. Bottom: resulting deformable mirror surface solutions after 10 iterations of pairwise-probing and electric field conjugation. The D-shaped dark hole in the bottom half is barely visible since electric field conjugation provides only very little improvement in contrast.

6.9 Optimizing radial features

One potential further avenue of investigation with hybrid phase mask designs involves varying all the parameters of the Dual Zone Phase mask (DZPM) and the Roddier dimple for promising additional hybrid designs. This includes the height of the Roddier dimple and possibly both radii and both heights for the DZPM. For now, this work only explored all the degrees of freedom for a hybrid design combining the sawtooth scalar vortex mask with a single Roddier phase dimple. Figure 6.10 shows the 2D parameter sweep performed and displays the resulting simulated average contrasts across 3 to 10 λ/D in 20% bandwidth light. A few different dimple radius values (0.5-0.7 λ/D) might yield similar performance, potentially allowing for an additional design freedom. However it is clear from this 2D sweep that the optimal height for a single phase dimple in a hybrid scalar vortex mask design is one that induces exactly a π phase shift.

Expanding this radial parameter optimization could lead to triple zone, quadruple zone, or even continuous radial features. These have potential to yield novel interesting and complex hybrid designs when combined with vortex coronagraph azimuthal

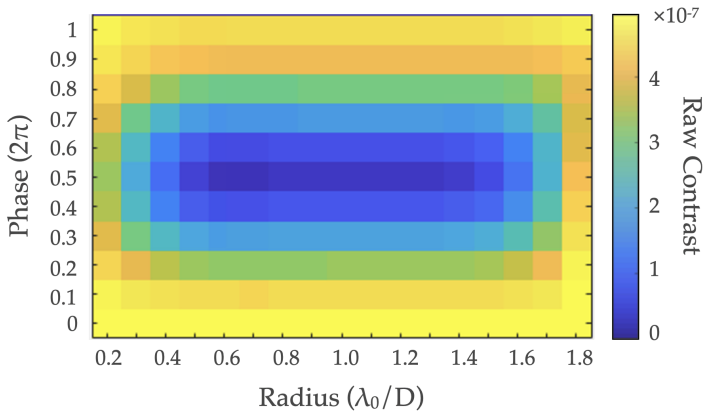

Figure 6.10: Averaged 2D wavefront propagation raw contrasts from 3 to 10 λ/D across 20% bandwidth for the charge 6 Sawtooth + Roddier dimple design with varying phase shifts and sizes of the dimple. The radius is given in units of the central wavelength λ_0.

profiles. However increased complexity in these patterns leads to more difficult fabrication requirements. Current manufacturing capabilities and constraints should be considered in future novel scalar vortex mask designs.

Chapter 7

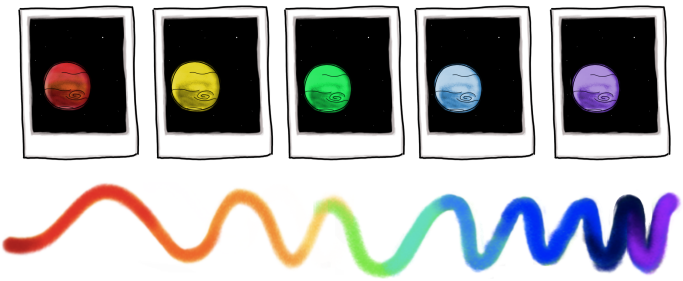

SUMMARY AND PERSPECTIVES

7.1 Summary

Direct imaging is crucial for the study of habitable exoplanets around Sun-like stars because it offers the potential to characterize their atmospheres and detect biosignatures. However, the extreme contrast between the bright starlight and faint planet light poses immense challenges that are addressed by coronagraphs. Current coronagraph instruments are capable of imaging young giant planets, however future space telescopes need better coronagraphs, super stable telescopes, and precision wavefront sensing and control that is effective and efficient in order to characterize habitable Earth-like planets. In this thesis the viability of scalar vortex coronagraphs for exoplanet direct imaging is explored. Through both simulation and laboratory demonstration, scalar vortex coronagraph focal plane masks are investigated and tested and novel designs are developed with promising potential for high contrast imaging.

The first two chapters present the scientific background and introduce the theory which form the foundation of this research. Chapter 1 covers a brief history of exoplanet discovery and explains the most successful detection methods. Very few planets have been directly imaged to date, as seen in Figure 1.1. The progress of direct imaging from both ground and space so far is briefly summarized and efforts to improve coronagraph technologies are motivated by the need to directly detect planets at contrasts of 10^{-10} across a sufficiently large bandwidth for spectroscopy

and characterization. Chapter 2 first briefly introduces Fourier optics and how light propagation is modeled between the pupil and focal planes of a telescope. Utilizing these principles, the theory of coronagraphs and how they suppress starlight to enable capturing the light from nearby sources like exoplanets is presented. Chapter 2 then motivates the need for focal plane wavefront sensing and control by the required contrasts and explains the concepts behind techniques for conjugating the electric field in closed loop with a deformable mirror.

Chapter 3 explains the scope of this thesis, the tools and the methods specifically developed for this research. The work conducted in this thesis falls into three categories: simulation work, design work, and laboratory experiments. In simulation, several coronagraph mask topographies are considered and the modeling efforts used to describe them are presented. A coronagraph pipeline based on Fourier optics principles was developed to predict contrast performance for scalar vortex mask designs. For the new design work in this thesis, a new modal decomposition analytical tool was developed to better understand the chromatic limitations of current scalar vortex mask topographies. This tool is later used to assess the new designs presented in this thesis. Finally, the laboratory setups of two high contrast imaging benches at Caltech (HCST) and JPL (IACT) for characterization and testing of scalar vortex coronagraphs are introduced.

Chapters 4, 5, and 6 are each based off peer-reviewed publications from this thesis and are supplemented by relevant work which was published as conference proceedings. Chapter 4 presents an analysis of current scalar vortex topographies and found phase wrapping to be advantageous over a classic vortex topography using the modal decomposition tool. This chapter also reports the first laboratory results of the wrapped staircase scalar vortex coronagraph, as a 'first generation scalar vortex coronagraph' which could be a promising alternative to current vector vortex coronagraphs. The chromatic behavior of this first-generation design was assessed on HCST and wavefront sensing and control was performed on IACT at JPL, achieving an average raw contrasts of 3.2×10^{-8} in monochromatic light and 2.2×10^{-7} across a 10% bandwidth.

Chapter 5 investigates how various wavefront sensing and control methods interact with both vector and scalar vortex masks. Three distinct model-based and model-free methods are implemented on IACT to obtain a direct comparison in identical laboratory conditions. The model-free techniques were found to be high-performing dark hole digging methods which ultimately reach equally high broadband contrasts

(around 3×10^{-8} for the vector vortex coronagraph and around 1×10^{-7} for the scalar vortex coronagraph in 10% bandwidth) as the current standard model-based technique. In general, as increasingly complex mask designs become more common, model-free techniques might be a preferred choice where model mismatch limits performance. This chapter also compares the advantages and disadvantages of each of these wavefront sensing and control algorithms with respect to their potential for future space telescopes and highlights the increased calibration costs of model-free methods compared to model-based approaches by studying convergence trends.

Chapter 6 explores the effects of adding central phase dimples to scalar masks to improve broadband performance by suppressing the chromatic stellar leakage. New hybrid designs are presented with radial phase dimples integrated with the sawtooth vortex, wrapped vortex, and cosine phase mask. This work showed that, using these dimples, it is possible to substantially improve the broadband contrast performance with these 'second generation scalar vortex coronagraphs.' One such hybrid design reaches simulated average contrasts of 3.77×10^{-9} in 10% bandwidth and 3.79×10^{-8} in 20% bandwidth. A prototype was fabricated and will be tested during the writing of this manuscript, as is discussed in the following section.

7.2 Future work

This thesis developed the necessary concepts for future fabrication and testing of new scalar vortex coronagraph masks targeting high performance across a broad band.

There are at least three main avenues of research directly building off the findings of this thesis. The first involves testing the new coronagraph designs proposed. The second explores the potential to achromatize a vortex phase mask by combining two materials. The third investigates an alternate scalar vortex coronagraph implementation using metasurface materials which impart a scalar vortex phase using a thin layer of subwavelength-scale structures. These three future scalar vortex concepts are shown in Figure 7.1.

The immediate next step following the work of this thesis is to manufacture and test the new hybrid vortex designs combining radial and azimuthal features proposed in Chapter 6. The simulations conducted in this thesis show promising potential from adding a central phase dimple to a sawtooth vortex coronagraph. In particular, the hybrid sawtooth design with the Roddier dimple will be tested experimentally. This design has just been fabricated by Zeiss, the same manufacturer as the successful

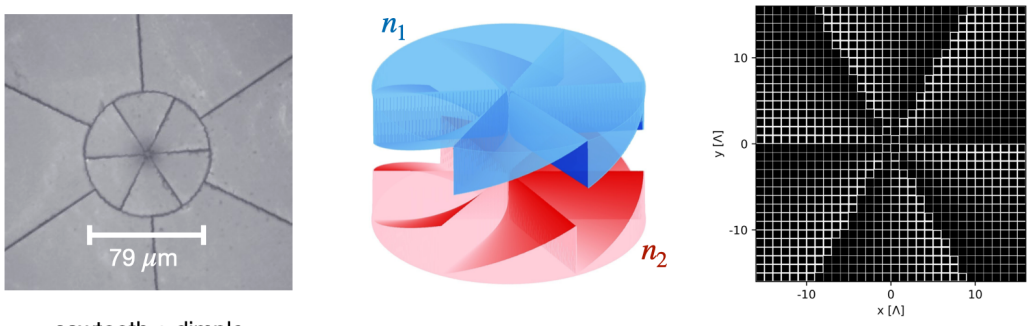

Figure 7.1: Three future avenues of SVC development: (left) Microscope image of newly received hybrid sawtooth designs with central phase dimple. (center) Schematic of a dual layer scalar vortex mask with two materials of different refractive indices. (right) Metasurface nanopost design of a scalar vortex mask (phasemap courtesy of König et al. (2023)).

wrapped staircase scalar vortex masks presented in Chapter 4. Its performance on the high contrast testbeds at Caltech and JPL will be measured with the same techniques utilized in this work and compared to the performances reported in this thesis. A microscope image of the central phase dimple of one of the new prototype masks taken during the characterization and metrology steps is shown in the left image in Figure 7.1.

The second avenue of future work builds off the design concepts investigated in this thesis to find even higher performing coronagraph phase mask designs using two layers. A dual-layer scalar vortex mask involves stacking two layers of different materials with different scalar vortex topographies, shown in the central schematic in Figure 7.1. The modal decomposition tool introduced in Chapter 3 is particularly helpful in calculating and assessing a potential alternative dual-layer scalar vortex coronagraph implementation because it helps identify the origin of zeroth order chromatic leakage. By leveraging the wavelength dependence of the refractive index for certain materials, clever material combinations can be chosen that suppress the original wavelength dependent term. These favorable choices can be identified through analyzing the zeroth order leakage apparent in the modal decompositions. Stacking several layers of dielectrics has been previously considered to increase broadband performance but was found to usually result in thick optics components which are not suitable for use in the focal plane (Swartzlander, 2006; Ruane et al., 2019). A next generation dual-layer design might consider higher vortex charges

which employ phase wrapping to remain within reasonable thickness and limit the material choices to those with high refractive indices. A new design might also involve adding a central phase dimple on one of the two vortex phase ramps. Finding suitable materials and respective fabrication methods for dual-layer scalar masks remains a challenge but will be explored in the coming years with collaborators specializing in manufacturing.

The third avenue will explore the application of metasurfaces to scalar vortex coronagraphs. Metasurfaces are thin structures consisting of millions of sub-wavelength building blocks arranged to create a specific phase and amplitude response to an incoming beam. Recent studies have shown that metasurfaces can be engineered to provide precise 2π phase coverage and high throughput across large bandwidths, making them a prime candidate for achromatic high-performance coronagraphs (Yu and Capasso, 2014; Khorasaninejad et al., 2016). Two new collaborations were started during this thesis to investigate the potential for metasurface implementations of scalar vortex coronagraphs. The wavefront propagation pipeline developed to simulate the performance of scalar vortex phase masks in this thesis has already been used to test the broadband performance of several new metasurface designs. Simulations of preliminary metasurface sawtooth vortex designs, like the one shown on the right of Figure 7.1, have shown promise in improving broadband performance (König et al., 2023; Palatnick et al., 2023) and manufacturing of these masks is currently underway. Once prototypes are successfully fabricated, they will be characterized and tested on the high contrast optical benches at Caltech and JPL as was done in this work. Their light suppression ability and chromatic behavior will be compared to the existing scalar and vector vortex masks and their designs will be iterated upon using the design and simulation tools developed in this thesis.

7.3 Perspectives

Direct imaging will be crucial in detecting and characterizing a habitable exoplanet. Advancements in coronagraph designs will be critical to enhancing direct imaging capabilities. Specifically achieving high contrast imaging across a broad band is essential for characterizing exoplanet atmospheres and detecting biosignatures, which was the focus of much of this work. All facets of direct imaging including the coronagraph system design itself, wavefront sensing and control techniques, and post-processing methods will need to be improved to reach the 10^{-10} contrast goal to detect an Earth twin. In addition, high contrast coronagraphy at this level must be done from space due to the absence of atmospheric turbulence. The Habitable

Worlds Observatory (HWO) holds hope for accomplishing this and in the process, discovering much more.

For the scientific goals of HWO, a coronagraph capable of achieving 10^{-10} contrasts will require not only extremely precise and well developed wavefront sensing and control methods, but also high performing focal plane masks. This thesis is especially relevant to proving the scalar vortex coronagraph is a viable candidate for HWO and has potential to reach the required performance with further development. Overall the scalar vortex coronagraph provides a significant advantage over the vector vortex alternative for its polarization independence. It should be seriously considered for HWO if comparable broadband performance is achieved in high contrast testbed experiments, especially since only minimal modification is needed (swapping the focal plane mask).

The achromatization strategies investigated in this thesis successfully improved the broadband contrast in simulation by several orders of magnitude but require further laboratory exploration. The future research avenues outlined, such as the fabrication and testing of the new hybrid vortex designs and exploration of dual-layer or metasurface implementations, set clear pathways for advancing focal plane mask development beyond the scope of this thesis. It is likely that the best performing broadband scalar vortex phase mask design will be a combination of the new topographies proposed here and new implementations discussed in the previous section.

This work not only presents theoretical coronagraph concepts but also provides practical demonstrations through simulation and laboratory experiments. The transition from new coronagraph instrument designs to practical implementations is crucial. Testing new coronagraph designs on high contrast optical benches with the methods investigated in this work will provide valuable insights into their real-world performance and suitability for deployment on future space missions. Moreover, the experimental comparison of electric field conjugation techniques performed in this work should prove useful in the selection of focal plane wavefront sensing and control strategy for HWO and other ground-based telescopes with extreme adaptive optic systems regardless of coronagraph choice.

Overall, in the coming years direct exoplanet detections from both ground and space telescopes will continue to complement each other as new approaches expand the parameter space of confirmed exoplanets which are reachable by current coronagraphs. The new generation of large ground based telescopes, the Extremely Large

Telescope, Giant Magellan Telescope, and Thirty Meter Telescope, will undoubtedly reveal new insights to planetary formation and systems very different than our own. New data from Gaia and JWST will be of unprecedented quality, exceeding that of any ground-based telescope. With the launch of the Roman Space Telescope, active wavefront control for high contrast imaging will be tested from space for the first time and pave the way for future larger space observatories like HWO. HWO will have the angular resolution and sensitivity to detect and characterize dozens of exo-Earths. It will bring us one step closer to answering fundamental questions about the formation and existence of our own Solar system and potentially life elsewhere in the Universe.

BIBLIOGRAPHY

Baudoz, P., A. Boccaletti, J. Baudrand, and D. Rouan (2006). "The Self-Coherent Camera: a new tool for planet detection". In: *IAU Colloq. 200: Direct Imaging of Exoplanets: Science & Techniques*. Ed. by C. Aime and F. Vakili, pp. 553–558. DOI: 10.1017/S174392130600994X.

Baudoz, P., R. Galicher, A. Potier, O. Dupuis, S. Thijs, and F. Patru (2018). "Optimization and performance of multi-deformable mirror correction on the THD2 bench". In: *Advances in Optical and Mechanical Technologies for Telescopes and Instrumentation III*. Ed. by R. Navarro and R. Geyl. Vol. 10706. Society of Photo-Optical Instrumentation Engineers (SPIE) Conference Series, 107062O, 107062O. DOI: 10.1117/12.2314089.

Baxter, W., A. Potier, G. Ruane, and C. M. Prada (2021). "Design and commissioning of an in-air coronagraph testbed in the HCIT facility at NASA's Jet Propulsion Laboratory". In: *Techniques and Instrumentation for Detection of Exoplanets X*. Ed. by S. B. Shaklan and G. J. Ruane. Vol. 11823. International Society for Optics and Photonics. SPIE, 118231S. DOI: 10.1117/12.2601432.

Bertrou-Cantou, A., J. Llop-Sayson, J. Liberman, D. Mawet, J. G. Hagopian, G. Ruane, et al. (2023). "High contrast spectroscopy testbed (HCST): experimental results with an apodized vortex coronagraph". In: *Society of Photo-Optical Instrumentation Engineers (SPIE) Conference Series*. Vol. 12680. Society of Photo-Optical Instrumentation Engineers (SPIE) Conference Series, 126801B, 126801B. DOI: 10.1117/12.2677902.

BMC (2024). *MEMS Deformable Mirrors: Architecture Description*. URL: https://bostonmicromachines.com/products/deformable-mirrors/standard-deformable-mirrors/.

Boccaletti, A., C. Cossou, P. Baudoz, P. O. Lagage, D. Dicken, A. Glasse, et al. (2022). "JWST/MIRI coronagraphic performances as measured on-sky". In: *Astronomy & Astrophysics* 667, A165. ISSN: 1432-0746. DOI: 10.1051/0004-6361/202244578.

Bordé, P. J. and W. A. Traub (2006). "High-Contrast Imaging from Space: Speckle Nulling in a Low-Aberration Regime". In: *The Astrophysical Journal* 638.1, pp. 488–498. ISSN: 1538-4357. DOI: 10.1086/498669.

Born, M. and E. Wolf (1980). "Chapter VIII - Elements of the theory of diffraction". In: *Principles of Optics (Sixth Edition)*. Ed. by M. Born and E. Wolf. Sixth Edition. Pergamon, pp. 370–458. ISBN: 978-0-08-026482-0. DOI: https://doi.org/10.1016/B978-0-08-026482-0.50015-3.

Carlotti, A. (2013). "Apodized phase mask coronagraphs for arbitrary apertures". In: *Astronomy & Astrophysics* 551, A10. ISSN: 1432-0746. DOI: 10.1051/0004-6361/201220661.

Cash, W. (2006). "Detection of Earth-like planets around nearby stars using a petal-shaped occulter". In: *Nature (London)* 442.7098, pp. 51–53. DOI: 10.1038/nature04930.

Charbonneau, D., T. M. Brown, D. W. Latham, and M. Mayor (2000). "Detection of Planetary Transits Across a Sun-like Star". In: *Astrophys. J. Lett.* 529.1, pp. L45–L48. DOI: 10.1086/312457.

Chauvin, G., A. Vigan, M. Bonnefoy, S. Desidera, M. Bonavita, D. Mesa, et al. (2015). "The VLT/NaCo large program to probe the occurrence of exoplanets and brown dwarfs at wide orbits: II. Survey description, results, and performances". In: *Astronomy & Astrophysics* 573, A127. ISSN: 1432-0746. DOI: 10.1051/0004-6361/201423564.

Currie, T., B. Biller, A.-M. Lagrange, C. Marois, O. Guyon, E. Nielsen, et al. (2023). *Direct Imaging and Spectroscopy of Extrasolar Planets*. arXiv: 2205.05696 [astro-ph.EP].

Delorme, J. R., R. Galicher, P. Baudoz, G. Rousset, J. Mazoyer, and O. Dupuis (2016). "Focal plane wavefront sensor achromatization: The multireference self-coherent camera". In: *Astronomy & Astrophysics* 588, A136. DOI: 10.1051/0004-6361/201527657.

Desai, N., A. Bertrou-Cantou, G. Ruane, J. Llop-Sayson, A. E. Riggs, E. Serabyn, and D. Mawet (Oct. 2023a). "Achromatizing scalar vortex coronagraphs with radial phase mask dimples". In: *Techniques and Instrumentation for Detection of Exoplanets XI*. Vol. 12680. SPIE. DOI: 10.1117/12.2677224.

Desai, N., J. Llop-Sayson, A. Bertrou-Cantou, G. Ruane, A. E. Riggs, E. Serabyn, and D. Mawet (Aug. 2022). "Topological designs for scalar vortex coronagraphs". In: *Space Telescopes and Instrumentation 2022: Optical, Infrared, and Millimeter Wave*. Ed. by L. E. Coyle, S. Matsuura, and M. D. Perrin. Vol. 12180. International Society for Optics and Photonics. SPIE, 121805H. DOI: 10.1117/12.2630950.

Desai, N., J. Llop-Sayson, N. Jovanovic, G. Ruane, E. Serabyn, S. Martin, and D. Mawet (Sept. 2021). "High contrast demonstrations of novel scalar vortex coronagraph designs at the high contrast spectroscopy testbed". In: *Techniques and Instrumentation for Detection of Exoplanets X*. Ed. by S. B. Shaklan and G. J. Ruane. SPIE. DOI: 10.1117/12.2603953.

Desai, N., D. Mawet, E. Serabyn, G. Ruane, A. Bertrou-Cantou, J. Llop-Sayson, and A. J. E. Riggs (Feb. 2024). "Benefits of adding radial phase dimples on scalar coronagraph phase masks". In: *Journal of Astronomical Telescopes, Instruments, and Systems* 10.1, p. 015001. DOI: 10.1117/1.JATIS.10.1.015001.

Desai, N., G. Ruane, J. D. Llop-Sayson, A. Bertrou-Cantou, A. Potier, A. E. Riggs, et al. (Apr. 2023b). "Laboratory demonstration of the wrapped staircase scalar vortex coronagraph". In: *Journal of Astronomical Telescopes, Instruments, and Systems* 9.2, p. 025001. DOI: 10.1117/1.JATIS.9.2.025001.

Devlin, R. C., A. Ambrosio, D. Wintz, S. L. Oscurato, A. Y. Zhu, M. Khorasaninejad, et al. (2017). "Spin-to-orbital angular momentum conversion in dielectric metasurfaces". In: *Opt. Express* 25.1, pp. 377–393.

Fanson, J. L., R. Bernstein, D. Ashby, B. C. Bigelow, G. Brossus, W. S. Burgett, et al. (2022). "Overview and status of the Giant Magellan Telescope project". In: *Ground-based and Airborne Telescopes IX*. Ed. by H. K. Marshall, J. Spyromilio, and T. Usuda. SPIE. DOI: 10.1117/12.2631694.

Fienup, J. R. (1982). "Phase retrieval algorithms: a comparison". In: *Appl. Opt.* 21.15, pp. 2758–2769. DOI: 10.1364/AO.21.002758.

Fitzgerald, M. P., S. Sallum, M. A. Millar-Blanchaer, R. Jensen-Clem, P. M. Hinz, O. Guyon, et al. (2022). "The Planetary Systems Imager for TMT: overview and status". In: *Ground-based and Airborne Instrumentation for Astronomy IX*. Ed. by C. J. Evans, J. J. Bryant, and K. Motohara. Vol. 12184. Society of Photo-Optical Instrumentation Engineers (SPIE) Conference Series, 1218426, p. 1218426. DOI: 10.1117/12.2630410.

Fogarty, K., R. Belikov, D. Sirbu, and E. Pluzhnik (2022). "The PIAA-vortex coronagraph: a new coronagraph technology to maximize exo-Earth yields in the Astro2020 era". In: *Space Telescopes and Instrumentation 2022: Optical, Infrared, and Millimeter Wave*. Ed. by L. E. Coyle, S. Matsuura, and M. D. Perrin. Vol. 12180. Society of Photo-Optical Instrumentation Engineers (SPIE) Conference Series, 1218028, p. 1218028. DOI: 10.1117/12.2630638.

Foo, G., D. M. Palacios, and J. Swartzlander Grover A. (2005). "Optical vortex coronagraph". In: *Optics Letters* 30.24, pp. 3308–3310. DOI: 10.1364/OL.30.003308.

Forgan, D., R. J. Parker, and K. Rice (2014). "The dynamical fate of self-gravitating disc fragments after tidal downsizing". In: *Monthly Notices of the Royal Astronomical Society* 447.1, pp. 836–845. ISSN: 0035-8711. DOI: 10.1093/mnras/stu2504.

Fulton, B. J., L. J. Rosenthal, L. A. Hirsch, H. Isaacson, A. W. Howard, C. M. Dedrick, et al. (2021). "California Legacy Survey. II. Occurrence of Giant Planets beyond the Ice Line". In: *The Astrophysical Journal Supplement Series* 255.1, p. 14. ISSN: 1538-4365. DOI: 10.3847/1538-4365/abfcc1.

Gaia Collaboration, T. Prusti, J. H. J. de Bruijne, A. G. A. Brown, A. Vallenari, C. Babusiaux, et al. (2016). "The Gaia mission". In: *aap* 595, A1, A1. DOI: 10.1051/0004-6361/201629272.

Galicher, R., P. Baudoz, G. Rousset, J. Totems, and M. Mas (2009). "Self-coherent camera as a focal plane wavefront sensor: simulations". In: *Astronomy and Astrophysics* 509, A31. ISSN: 1432-0746. DOI: 10.1051/0004-6361/200912902.

Galicher, R., E. Huby, P. Baudoz, and O. Dupuis (2020). "A family of phase masks for broadband coronagraphy example of the wrapped vortex phase mask theory and laboratory demonstration". In: *Astronomy & Astrophysics* 635, A11. DOI: 10.1051/0004-6361/201936971.

Galicher, R. and J. Mazoyer (2023). "Imaging exoplanets with coronagraphic instruments". In: *Comptes Rendus. Physique* 24.S2, pp. 1–45. ISSN: 1878-1535. DOI: 10.5802/crphys.133.

Ganic, D., X. Gan, M. Gu, M. Hain, S. Somalingam, S. Stankovic, and T. Tschudi (2002). "Generation of doughnut laser beams by use of a liquid-crystal cell with a conversion efficiency near 100%". In: *Opt. Lett.* 27.15, pp. 1351–1353. DOI: 10.1364/OL.27.001351.

Gerard, B. L. and C. Marois (2020). "Focal Plane Wavefront Sensing with the FAST TGV Coronagraph". In: *Publications of the Astronomical Society of the Pacific* 132.1012, p. 064401. ISSN: 1538-3873. DOI: 10.1088/1538-3873/ab84c9.

Gerchberg, R. W. (1972). "A practical algorithm for the determination of phase from image and diffraction plane pictures". In: *Optik* 35, pp. 237–246.

Gilmozzi, R. and J. Spyromilio (2007). "The European Extremely Large Telescope (E-ELT)". In: *The Messenger* 127, p. 11.

Give'On, A. (2009). "A unified formailism for high contrast imaging correction algorithms". In: *Techniques and Instrumentation for Detection of Exoplanets IV*. Ed. by S. B. Shaklan. Vol. 7440. Society of Photo-Optical Instrumentation Engineers (SPIE) Conference Series, 74400D, p. 74400D. DOI: 10.1117/12.825049.

Give'on, A., B. Kern, S. Shaklan, D. C. Moody, and L. Pueyo (2007). "Broadband wavefront correction algorithm for high-contrast imaging systems". In: *Astronomical Adaptive Optics Systems and Applications III*. Ed. by R. K. Tyson and M. Lloyd-Hart. Vol. 6691. Society of Photo-Optical Instrumentation Engineers (SPIE) Conference Series, 66910A, 66910A. DOI: 10.1117/12.733122.

Goodman, J. (2005). *Introduction to Fourier Optics*. McGraw-Hill physical and quantum electronics series. W. H. Freeman. ISBN: 9780974707723.

Groff, T. D., A. J. E. Riggs, B. Kern, and N. J. Kasdin (2016). "Methods and limitations of focal plane sensing, estimation, and control in high-contrast imaging". In: *Journal of Astronomical Telescopes, Instruments, and Systems* 2, 011009, p. 011009. DOI: 10.1117/1.JATIS.2.1.011009.

Haffert, S. Y. (2022). "The spectrally modulated self-coherent camera (SM-SCC): Increasing throughput for focal-plane wavefront sensing". In: *Astronomy & Astrophysics* 659, A51. ISSN: 1432-0746. DOI: 10.1051/0004-6361/202141309.

Haffert, S. Y., J. R. Males, K. Ahn, K. V. Gorkom, O. Guyon, L. M. Close, et al. (2023). "Implicit electric field conjugation: Data-driven focal plane control". In: *Astronomy & Astrophysics* 673, A28. DOI: 10.1051/0004-6361/202244960.

Hénault, F. (2015). "Strehl ratio: a tool for optimizing optical nulls and singularities". In: *Journal of the Optical Society of America A* 32.7, p. 1276. DOI: 10.1364/JOSAA.32.001276.

Hénault, F., A. Carlotti, and C. Vérinaud (2016). "Analysis of nulling phase functions suitable to image plane coronagraphy". In: *Advances in Optical and Mechanical Technologies for Telescopes and Instrumentation II*. Ed. by R. Navarro and J. H. Burge. SPIE. DOI: 10.1117/12.2231188.

Henry, G. W., G. W. Marcy, R. P. Butler, and S. S. Vogt (1999). "A Transiting "51 Peg-like" Planet*". In: *The Astrophysical Journal* 529.1, p. L41. DOI: 10.1086/312458.

Ida, S., D. N. C. Lin, and M. Nagasawa (2013). "Toward a Deterministic Model of Planetary Formation. VII. Eccentricity Distribution of Gas Giants". In: *The Astrophysical Journal* 775.1, p. 42. DOI: 10.1088/0004-637X/775/1/42.

Kasper, M., N. Cerpa Urra, P. Pathak, M. Bonse, J. Nousiainen, B. Engler, et al. (2021). "PCS — A Roadmap for Exoearth Imaging with the ELT". In: *Published in The Messenger vol. 182* pp. 38-43, March 2021. DOI: 10.18727/0722-6691/5221.

Kenworthy, M. A., J. L. Codona, P. M. Hinz, J. R. P. Angel, A. Heinze, and S. Sivanandam (2007). "First On-Sky High-Contrast Imaging with an Apodizing Phase Plate". In: *The Astrophysical Journal* 660.1, pp. 762–769. ISSN: 1538-4357. DOI: 10.1086/513596.

Khorasaninejad, M., W. T. Chen, R. C. Devlin, J. Oh, A. Y. Zhu, and F. Capasso (2016). "Metalenses at visible wavelengths: Diffraction-limited focusing and subwavelength resolution imaging". In: *Science* 352.6290, pp. 1190–1194. ISSN: 1095-9203. DOI: 10.1126/science.aaf6644.

König, L., S. Palatnick, N. Desai, M. Absil O. an Millar-Blanchaer, and D. Mawet (2023). "Metasurface-based scalar vortex phase mask design in pursuit of 1e-10 contrast". In: *Techniques and Instrumentation for Detection of Exoplanets XI*. Vol. 12680.

König, L., O. Absil, M. Lobet, C. Delacroix, M. Karlsson, G. Orban de Xivry, and J. Loicq (2022). "Optimal design of the annular groove phase mask central region". In: *Optics Express* 30.15, p. 27048. DOI: 10.1364/OE.461047.

Konopacky, Q. M., T. S. Barman, B. A. Macintosh, and C. Marois (2013). "Detection of Carbon Monoxide and Water Absorption Lines in an Exoplanet Atmosphere". In: *Science* 339.6126, pp. 1398–1401. ISSN: 1095-9203. DOI: 10.1126/science.1232003.

Kühn, J., E. Serabyn, J. Lozi, N. Jovanovic, T. Currie, O. Guyon, et al. (2018). "An H-band Vector Vortex Coronagraph for the Subaru Coronagraphic Extreme Adaptive Optics System". In: *Publications of the Astronomical Society of the Pacific* 130.985, p. 035001. DOI: 10.1088/1538-3873/aa9fe5.

Lafreniere, D., C. Marois, R. Doyon, D. Nadeau, and E. Artigau (2007). "A New Algorithm for Point-Spread Function Subtraction in High-Contrast Imaging: A Demonstration with Angular Differential Imaging". In: *The Astrophysical Journal* 660.1, pp. 770–780. ISSN: 1538-4357. DOI: 10.1086/513180.

Lafrenière, D., C. Marois, R. Doyon, and T. Barman (2009). "HST/NICMOS DETECTION OF HR 8799 b IN 1998". In: *The Astrophysical Journal* 694.2, pp. L148–L152. ISSN: 1538-4357. DOI: 10.1088/0004-637x/694/2/l148.

Lazorenko, P. F. and J. Sahlmann (2017). "Gaiaand VLT astrometry of faint stars: Precision ofGaiaDR1 positions and updated VLT parallaxes of ultracool dwarfs". In: *Astronomy & Astrophysics* 606, A90. ISSN: 1432-0746. DOI: 10.1051/0004-6361/201731544. URL: http://dx.doi.org/10.1051/0004-6361/201731544.

Lee, J. H., G. Foo, E. G. Johnson, and G. A. Swartzlander (2006). "Experimental Verification of an Optical Vortex Coronagraph". In: *Physical Review Letters* 97 (5), p. 053901. DOI: 10.1103/PhysRevLett.97.053901.

Liu, H., Z. Lu, and F. Li (2005). "Using diffractive optical element and Zygo interferometer to test large-aperture convex surface". In: *Optics & Laser Technology* 37.8, pp. 642–646. ISSN: 0030-3992. DOI: https://doi.org/10.1016/j.optlastec.2004.09.001.

Llop-Sayson, J., N. Jovanovic, G. Morrissey, D. Echeverri, and D. Mawet (2020a). "Wavefront control experiments with a single mode fiber at the High-Contrast Spectroscopy Testbed for Segmented Telescopes (HCST)". In: *Society of Photo-Optical Instrumentation Engineers (SPIE) Conference Series*. Vol. 11443. Society of Photo-Optical Instrumentation Engineers (SPIE) Conference Series, 114432Q, 114432Q. DOI: 10.1117/12.2562973.

Llop-Sayson, J., G. Ruane, D. Mawet, N. Jovanovic, C. T. Coker, J.-R. Delorme, et al. (2020b). "High-contrast Demonstration of an Apodized Vortex Coronagraph". In: *The Astronomical Journal* 159.3, p. 79. ISSN: 1538-3881. DOI: 10.3847/1538-3881/ab6329.

Lyot, B. (1939). "The study of the solar corona and prominences without eclipses (George Darwin Lecture, 1939)". In: *Monthly Notices of the Royal Astronomical Society* 99, p. 580. DOI: 10.1093/mnras/99.8.580.

Malbet, F., J. W. Yu, and M. Shao (1995). "High-Dynamic-Range Imaging Using a Deformable Mirror for Space Coronography". In: *Publications of the Astronomical Society of the Pacific* 107, p. 386. ISSN: 1538-3873. DOI: 10.1086/133563.

Males, J. R., L. Close, S. Y. Haffert, O. Guyon, V. Gasho, F. Coronado, et al. (2022). "The conceptual design of GMagAO-X: visible wavelength high contrast imaging with GMT". In: *Adaptive Optics Systems VIII*. Ed. by D. Schmidt, L. Schreiber, and E. Vernet. SPIE. DOI: 10.1117/12.2630619.

Marois, C., D. Lafreniere, R. Doyon, B. Macintosh, and D. Nadeau (2006). "Angular Differential Imaging: A Powerful High-Contrast Imaging Technique". In: *The Astrophysical Journal* 641.1, pp. 556–564. ISSN: 1538-4357. DOI: 10.1086/500401.

Martinez, P. (2019). "Fast-modulation imaging with the self-coherent camera". In: *Astronomy & Astrophysics* 629, L10, p. L10. DOI: 10.1051/0004-6361/201936496.

Mawet, D., P. Riaud, O. Absil, and J. Surdej (2005a). "Annular Groove Phase Mask Coronagraph". In: *The Astrophysical Journal* 633.2, pp. 1191–1200. DOI: 10.1086/462409.

Mawet, D., E. Serabyn, K. Liewer, C. Hanot, S. McEldowney, D. Shemo, and N. O'Brien (2009a). "Optical Vectorial Vortex Coronagraphs using Liquid Crystal Polymers: theory, manufacturing and laboratory demonstration". In: *Optics Express* 17.3, p. 1902. DOI: 10.1364/oe.17.001902.

Mawet, D., E. Serabyn, K. M. Liewer, R. S. Burruss, J. P. Hickey, and D. M. Shemo (2009b). "The Vector vortex coronagraph: Laboratory results and first light at Palomar Observatory". In: *The Astrophysical Journal* 709, pp. 53–57.

Mawet, D., O. Absil, J. Milli, C. Delacroix, J. Girard, J. O'Neal, et al. (2013). "Small-angle, high-contrast exoplanet imaging with the L-band AGPM vector vortex coronagraph now offered at the VLT". In: vol. 8864, p. 88640I. DOI: 10.1117/12.2025501.

Mawet, D., N. Murakami, C. Delacroix, E. Serabyn, O. Absil, N. Baba, et al. (2011). "Taking the vector vortex coronagraph to the next level for ground- and space-based exoplanet imaging instruments: review of technology developments in the USA, Japan, and Europe". In: *Techniques and Instrumentation for Detection of Exoplanets V*. Ed. by S. Shaklan. Vol. 8151. Society of Photo-Optical Instrumentation Engineers (SPIE) Conference Series, 815108, p. 815108. DOI: 10.1117/12.896059.

Mawet, D., P. Riaud, J. Surdej, and J. Baudrand (2005b). "Subwavelength surface-relief gratings for stellar coronagraphy." In: *Applied Optics* 44 34, pp. 7313–21.

Mayor, M. and D. Queloz (1995). "A Jupiter-mass companion to a solar-type star". In: *Nature (London)* 378.6555, pp. 355–359. DOI: 10.1038/378355a0.

Mazoyer, J., P. Baudoz, R. Galicher, M. Mas, and G. Rousset (2013). "Estimation and correction of wavefront aberrations using the self-coherent camera: laboratory results". In: *Astronomy & Astrophysics* 557, A9. ISSN: 1432-0746. DOI: 10.1051/0004-6361/201321706.

Murakami, N., S. Hamaguchi, M. Sakamoto, R. Fukumoto, A. Ise, K. Oka, et al. (2013). "Design and laboratory demonstration of an achromatic vector vortex coronagraph". In: *Optics express* 21, pp. 7400–10. DOI: 10.1364/OE.21.007400.

Murakami, N., R. Uemura, N. Baba, J. Nishikawa, M. Tamura, N. Hashimoto, and L. Abe (2008). "An Eight-Octant Phase-Mask Coronagraph". In: *Publications of the Astronomical Society of the Pacific* 120.872, pp. 1112–1118. DOI: 10.1086/592285.

N'Diaye, M., R. Soummer, A. Carlotti, K. Dohlen, K. Fogarty, J. Mazoyer, et al. (2018). "Apodized Pupil Lyot coronagraphs with arbitrary aperture telescopes: novel designs using hybrid focal plane masks". In: *Space Telescopes and Instrumentation 2018: Optical, Infrared, and Millimeter Wave*. Ed. by H. A. MacEwen, M. Lystrup, G. G. Fazio, N. Batalha, E. C. Tong, and N. Siegler. SPIE. DOI: 10.1117/12.2313225.

NASA Exoplanet Science Institute (2020). *Planetary Systems Table*. DOI: 10.26133/NEA12. URL: https://catcopy.ipac.caltech.edu/dois/doi.php?id=10.26133/NEA12.

National Academies of Sciences, Engineering and Medicine (2021). *Pathways to Discovery in Astronomy and Astrophysics for the 2020s*. DOI: 10.17226/26141.

Nielsen, E. L., R. J. De Rosa, B. Macintosh, J. J. Wang, J.-B. Ruffio, E. Chiang, et al. (2019). "The Gemini Planet Imager Exoplanet Survey: Giant Planet and Brown Dwarf Demographics from 10 to 100 au". In: *The Astronomical Journal* 158.1, p. 13. ISSN: 1538-3881. DOI: 10.3847/1538-3881/ab16e9.

Packham, C., M. Honda, M. Chun, I. Sakon, M. Richter, Y. Okamoto, et al. (2018). "MICHI: a thermal-infrared instrument for the TMT". In: *Ground-based and Airborne Instrumentation for Astronomy VII*. Ed. by H. Takami, C. J. Evans, and L. Simard. SPIE. DOI: 10.1117/12.2313967.

Palatnick, S., L. König, M. Millar-Blanchaer, J. K. Wallace, O. Absil, D. Mawet, et al. (2023). "Prospects for Metasurfaces in Exoplanet Direct Imaging Systems: from principles to design". In: *Techniques and Instrumentation for Detection of Exoplanets XI*. Vol. 12680.

Potier, A., P. Baudoz, R. Galicher, G. Singh, and A. Boccaletti (2020). "Comparing focal plane wavefront control techniques: Numerical simulations and laboratory experiments". In: *Astronomy & Astrophysics* 635, A192. DOI: 10.1051/0004-6361/201937015.

Pueyo, L., N. J. Kasdin, and S. Shaklan (2011). "Propagation of aberrations through phase-induced amplitude apodization coronagraph". In: *Journal of the Optical Society of America A* 28.2, p. 189. ISSN: 1520-8532. DOI: 10.1364/josaa.28.000189.

Quesnel, M., G. Orban de Xivry, G. Louppe, and O. Absil (2022). "A deep learning approach for focal-plane wavefront sensing using vortex phase diversity". In: *Astronomy & Astrophysics* 668, A36. ISSN: 1432-0746. DOI: 10.1051/0004-6361/202143001.

Racine, R., G. A. H. Walker, D. Nadeau, R. Doyon, and C. Marois (1999). "Speckle Noise and the Detection of Faint Companions". In: *Pub. Astron. Soc. Pacific* 111.759, pp. 587–594. DOI: 10.1086/316367.

Riggs, A. J. E., G. Ruane, E. Serabyn, W. Baxter, J. Llop-Sayson, C. Mejia Prada, et al. (2022). "High-contrast demonstration of a vector vortex coronagraph with a segmented, off-axis aperture". In: *Space Telescopes and Instrumentation 2022: Optical, Infrared, and Millimeter Wave*. Ed. by L. E. Coyle, S. Matsuura, and M. D. Perrin. Vol. 12180. Society of Photo-Optical Instrumentation Engineers (SPIE) Conference Series, 121805I, p. 121805I. DOI: 10.1117/12.2630130.

Riggs, A. J. E., G. Ruane, E. Sidick, C. Coker, B. D. Kern, and S. B. Shaklan (2018). "Fast linearized coronagraph optimizer (FALCO) I: a software toolbox for rapid coronagraphic design and wavefront correction". In: *Space Telescopes and Instrumentation 2018: Optical, Infrared, and Millimeter Wave*. Ed. by M. Lystrup, H. A. MacEwen, G. G. Fazio, N. Batalha, N. Siegler, and E. C. Tong. Vol. 10698. Society of Photo-Optical Instrumentation Engineers (SPIE) Conference Series, 106982V, p. 106982V. DOI: 10.1117/12.2313812.

Roddier, F. and C. Roddier (1997). "Stellar Coronagraph with Phase Mask". In: *Publications of the Astronomical Society of the Pacific* 109.737, p. 815. DOI: 10.1086/133949.

Rouan, D., P. Riaud, A. Boccaletti, Y. Clénet, and A. Labeyrie (2000). "The Four-Quadrant Phase-Mask Coronagraph. I. Principle". In: *Publications of the Astronomical Society of the Pacific* 112.777, p. 1479. DOI: 10.1086/317707.

Ruane, G., D. Mawet, B. Mennesson, J. Jewell, and S. Shaklan (2018). "Vortex coronagraphs for the Habitable Exoplanet Imaging Mission concept: theoretical performance and telescope requirements". In: *Journal of Astronomical Telescopes, Instruments, and Systems* 4.01, p. 1. DOI: 10.1117/1.jatis.4.1.015004.

Ruane, G., D. Mawet, A. E. Riggs, and E. Serabyn (2019). "Scalar vortex coronagraph mask design and predicted performance". In: *Techniques and Instrumentation for Detection of Exoplanets IX*. Ed. by S. B. Shaklan. SPIE. DOI: 10.1117/12.2528625.

Ruane, G., A. J. E. Riggs, E. Serabyn, W. Baxter, C. Mejia Prada, D. Mawet, et al. (2022). "Broadband Vector Vortex Coronagraph Testing at NASA's High Contrast Imaging Testbed Facility". In: *Society of Photo-Optical Instrumentation Engineers (SPIE) Conference Series*. Society of Photo-Optical Instrumentation Engineers (SPIE) Conference Series.

Ruane, G., E. Serabyn, C. Mejia Prada, W. Baxter, E. A. Bendek, D. Mawet, and A. J. E. Riggs (2020). "Experimental analysis of the achromatic performance of a vector vortex coronagraph". In: *Space Telescopes and Instrumentation 2020: Optical, Infrared, and Millimeter Wave*. Ed. by M. Lystrup, N. Batalha, E. C. Tong, N. Siegler, and M. D. Perrin. SPIE. DOI: 10.1117/12.2561593.

Ruffio, J.-B. and M. Kasper (2022). *Non Common Path Aberrations Correction*. arXiv: 2211.00775 [astro-ph.IM].

Seo, B.-J., K. Patterson, K. Balasubramanian, B. Crill, T. Chui, D. Echeverri, et al. (2019). "Testbed demonstration of high-contrast coronagraph imaging in search for Earth-like exoplanets". In: *Techniques and Instrumentation for Detection of Exoplanets IX*. Ed. by S. B. Shaklan. Vol. 11117. International Society for Optics and Photonics. SPIE, p. 111171V. DOI: 10.1117/12.2530033.

Serabyn, E., E. Huby, K. Matthews, D. Mawet, O. Absil, B. Femenia, et al. (2017). "The W. M. Keck Observatory Infrared Vortex Coronagraph and a First Image of HIP 79124 B". In: *The Astrophysical Journal* 153.1, 43, p. 43. DOI: 10.3847/1538-3881/153/1/43.

Serabyn, E., C. M. Prada, P. Chen, and D. Mawet (2019). "Vector vortex coronagraphy for exoplanet detection with spatially variant diffractive waveplates". In: *Journal of the Optical Society of America B Optical Physics* 36.5, p. D13. DOI: 10.1364/JOSAB.36.000D13.

Serabyn, E., G. Ruane, and D. Echeverri (2022). "Observing inside the coronagraphic regime with optimized single-mode nulling interferometry". In: *Space Telescopes and Instrumentation 2022: Optical, Infrared, and Millimeter Wave*. Ed. by L. E. Coyle, M. D. Perrin, and S. Matsuura. SPIE. DOI: 10.1117/12.2630589.

Smith, W. H. (1987). "Spectral differential imaging detection of planets about nearby stars." In: *Pub. Astron. Soc. Pacific* 99, pp. 1344–1353. DOI: 10.1086/132124.

Soummer, R., K. Dohlen, and C. Aime (2003). "Achromatic dual-zone phase mask stellar coronagraph". In: *Astronomy & Astrophysics* 403, pp. 369–381. DOI: 10.1051/0004-6361:20030278.

Sparks, W. B. and H. C. Ford (2002). "Imaging Spectroscopy for Extrasolar Planet Detection". In: *The Astrophysical Journal* 578.1, pp. 543–564. ISSN: 1538-4357. DOI: 10.1086/342401.

Spergel, D., N. Gehrels, J. Breckinridge, M. Donahue, A. Dressler, B. S. Gaudi, et al. (2013). "Wide-Field InfraRed Survey Telescope-Astrophysics Focused Telescope Assets WFIRST-AFTA Final Report". In: *arXiv e-prints*, arXiv:1305.5422, arXiv:1305.5422. DOI: 10.48550/arXiv.1305.5422.

Swartzlander, G. (2005). "Broadband nulling of a vortex phase mask". In: *Optics Letters* 30.21, p. 2876. ISSN: 1539-4794. DOI: 10.1364/ol.30.002876.

Swartzlander, G., E. L. Ford, R. S. Abdul-Malik, L. M. Close, M. A. Peters, D. M. Palacios, and D. W. Wilson (2008). "Astronomical demonstration of an optical vortex coronagraph". In: *Optics Express* 16.14, p. 10200. DOI: 10.1364/OE.16.010200.

Swartzlander, G. (2006). "Achromatic optical vortex lens". In: *Optics Letters* 31.13, pp. 2042–2044. DOI: 10.1364/OL.31.002042.

Thompson, W., C. Marois, G. Singh, O. Lardière, B. Gerard, Q. Fu, and W. Heidrich (2022). "Performance of the Fast Atmospheric Self Coherent camera at the NEW-EARTH lab and a simplified measurement algorithm". In: *Adaptive Optics Systems VIII*. Ed. by L. Schreiber, D. Schmidt, and E. Vernet. Vol. 12185. Society of Photo-Optical Instrumentation Engineers (SPIE) Conference Series, 121852C, p. 121852C. DOI: 10.1117/12.2630415.

Vigan, A., C. Fontanive, M. Meyer, B. Biller, M. Bonavita, M. Feldt, et al. (2021). "The SPHERE infrared survey for exoplanets (SHINE): III. The demographics of young giant exoplanets below 300 au with SPHERE". In: *Astronomy & Astrophysics* 651, A72. ISSN: 1432-0746. DOI: 10.1051/0004-6361/202038107.

Wang, J. J., S. Ginzburg, B. Ren, N. Wallack, P. Gao, D. Mawet, et al. (2020). "Keck/NIRC2 L'-band Imaging of Jovian-mass Accreting Protoplanets around PDS 70". In: *The Astronomical Journal* 159.6, p. 263. ISSN: 1538-3881. DOI: 10.3847/1538-3881/ab8aef.

Wolszczan, A. and D. A. Frail (1992). "A planetary system around the millisecond pulsar PSR1257 + 12". In: *Nature (London)* 355.6356, pp. 145–147. DOI: 10.1038/355145a0.

Yu, N. and F. Capasso (2014). "Flat optics with designer metasurfaces". In: *Nature Materials* 13.2, pp. 139–150. ISSN: 1476-4660. DOI: 10.1038/nmat3839.

A CARTOON THESIS

Meet the Goldiloxs!

A cartoon thesis by: Niyati Desai

The Goldiloxs are an alien family looking for a new home!

They're all packed and ready to go.

Now the only question is where to? They don't want somewhere...

too hot or too cold

They want somewhere 'just right'!

Each night on their home world, the Goldiloxs set their telescope up in their backyard...

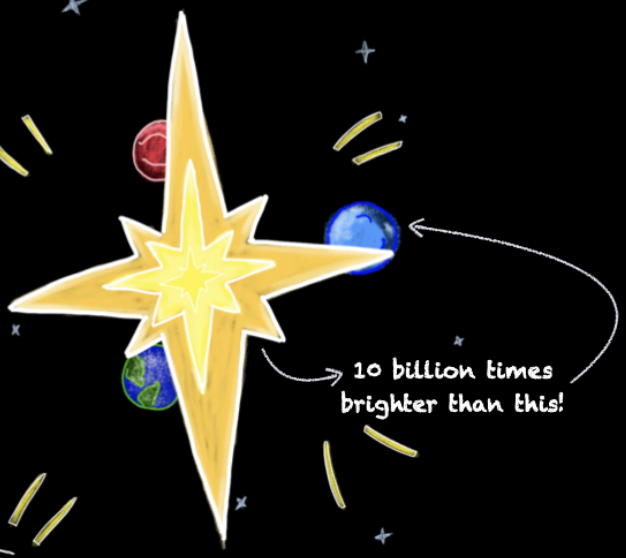

But whenever they try to look for planets, they're blinded by bright starlight.

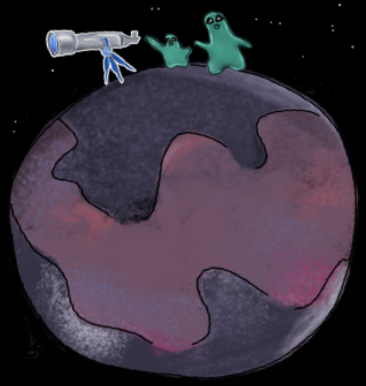

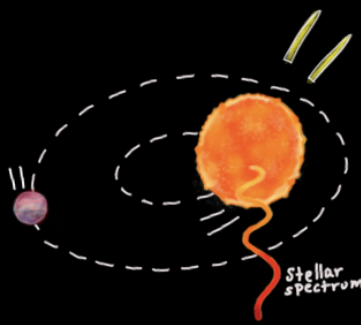

Because of this, 98% of the exoplanets known today have been detected indirectly:

by noticing a star wobble or get dimmer, then brighter again

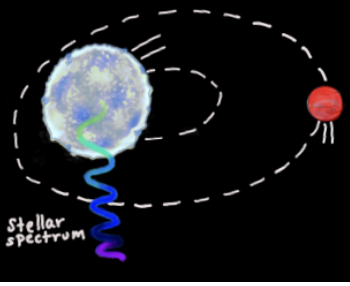

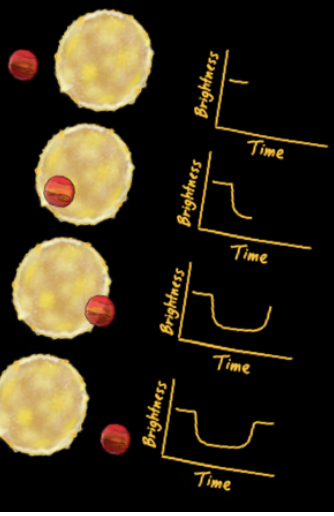

But that's not enough to learn about a planet's atmosphere.

Light directly from a planet in multiple wavelengths is needed to reveal if the planet's atmosphere is 'just right'!.

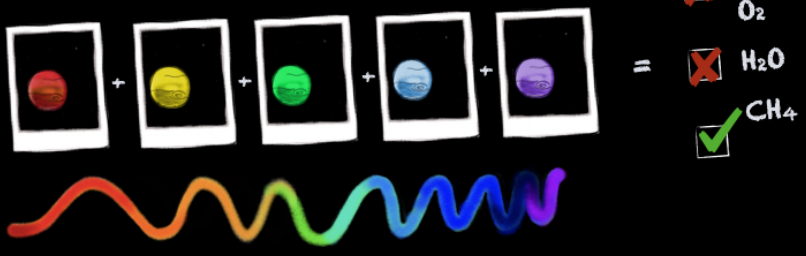

To block the starlight the Goldiloxs need a...

CORONAGRAPH!

But current coronagraph designs are chromatic, meaning they work well in only one wavelength.

This research aims to design better coronagraphs which can reach contrasts of 10^{-10} across many wavelengths.

$$\text{Contrast} = \frac{\text{brightness}\left(\bigcirc\right)}{\text{brightness}\left(\text{✦}\right)}$$

There are 2 main parts of a coronagraph that allow stars to be blocked and planets to be imaged:

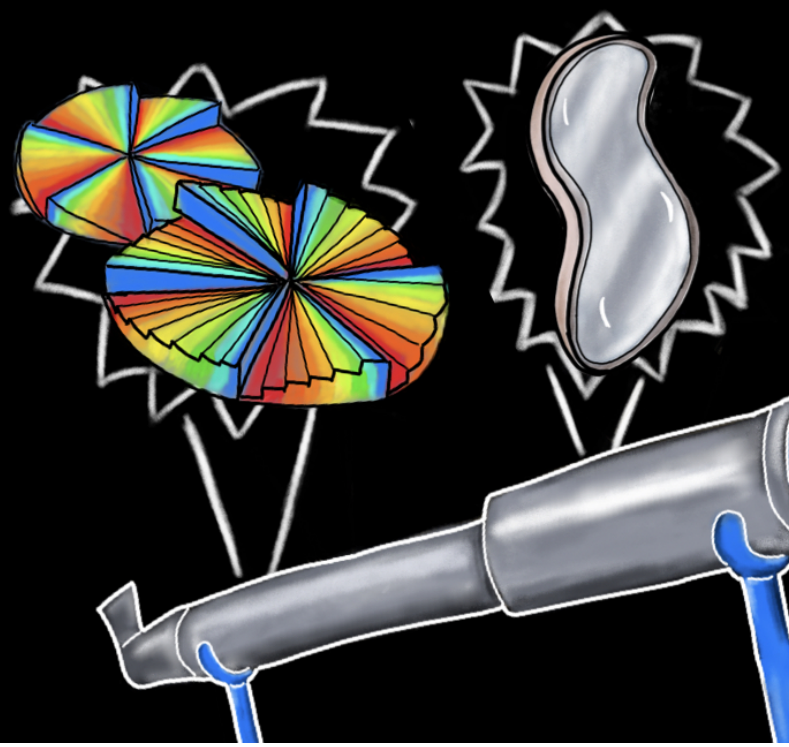

1) a geometric vortex mask shaped to filter out a star's light

2) a bendy mirror that helps direct the light so it lands perfectly on the mask

This thesis explores both!

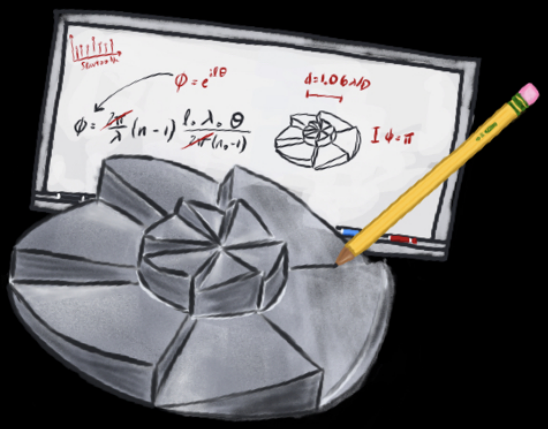

This thesis designs new vortex patterned optics that block starlight in broadband light.

It also explores ways to shape a coronagraph's bendy mirror to improve performance.

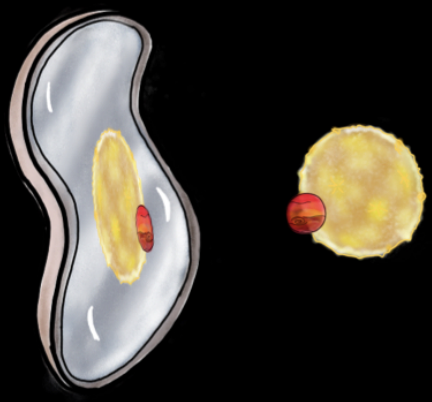

These ideas are investigated first in simulation by modeling the path of a star's light through the telescope.

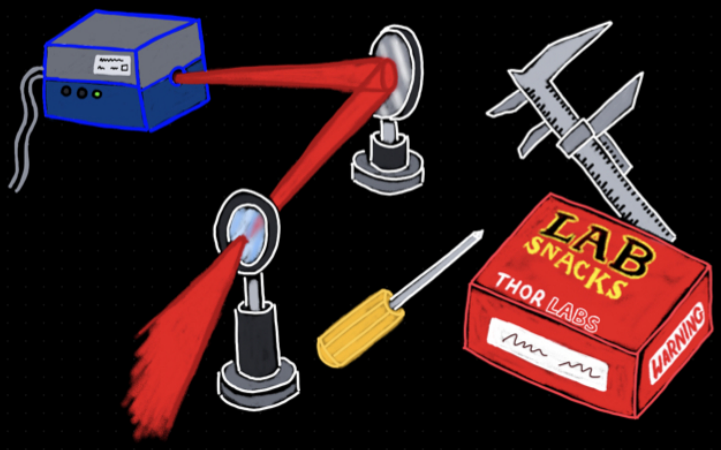

Then they are tested in laboratory experiments to see which coronagraph designs work best!

Much like the Goldiloxs, I've been searching for the 'just right' combination of vortex design and bendy mirror shape!

Thanks to this research, the Goldiloxs will be able to find their new home!